Beam Dynamics

for a Racetrack-Shape Fixed Field Induction Accelerator for

Giant Cluster Ions and Its Key Devices

by

Taufik

A Dissertation Submitted to the Doctoral Program

Department of Accelerator Science

School of High Energy Accelerator Science

The Graduate University for Advanced Studies

Acknowledgments

Baba. Their support in the past years has allowed my research to proceed smoothly and enjoyably.

Finally, I would like to express my heartfelt gratitude to my beloved wife, Istikomah, for her sacrifice in accompanying me and dealing with a different cultural environment. Her efforts in taking on many roles in the household and caring for my sons, Syahdan Hafidz Rabbani and Azka Musyafa Rabbani, became my inspiration to finish my studies. I also thank my father, Djatnika, and my mother, Alis Nuraeni, who always pray for me and support me in my success.

Abstract

For more than two decades, cluster ions have attracted broad interest in the field of material science and technology. Their interactions with materials have unique features compared with single heavy ions. A typical unique feature is the cluster effect, which results from localized, high-intensity energy deposition in materials. Cluster ions have been used for surface modification of materials and improving secondary ion mass spectrometry analysis. The cluster effect is also useful in high-energy applications. High-energy cluster ions are expected to be used in mutating plants and microorganisms, novel material modification in deep, and inertial fusion. However, the energy of cluster ion acceleration, which has been performed by electrostatic accelerators, has a limitation. To overcome this limitation, a racetrack-shape fixed field induction acceleration (RAFFIA) was proposed at KEK, Japan, in 2015.

The RAFFIA ring with two straight sections consists of four bending magnets, ramping quadrupole doublets, steering magnets, an electrostatic injection kicker, and induction cells. The bending magnet is a key component, which has the gradient field in the main pole region and the reverse field in the front. To investigate the orbit stability, a particle tracking code has been developed to simulate particle orbits through the acceleration cycle. A linear orbit theory has been established to determine the essential features of the RAFFIA, such as the lattice function, momentum dispersion function, closed-orbit distortion , and compaction factor. These features have some similarities to those in a synchrotron, although they vary with acceleration because the orbit gradually changes like that in a cyclotron. The non-uniformity of the magnetic field along the longitudinal direction of the bending magnet generates the intrinsic closed-orbit distortion. Ramped steering magnets are required for orbit stability as well as ramped quadrupole doublets. The beam stability is confirmed throughout an entire acceleration cycle by macroparticle tracking simulations. Longitudinal motion with a time-varying

transition energy, which is one of the characteristic features in the RAFFIA, has been studied using computer simulations.

In this work, a nonlinear beam-core evolution equation approach is proposed to estimate the acceptable beam current, which is the space charge limit. The approach is justified by a macroparticle simulation over a wide beam current parameter region. The instability seen in the beam-core evolution is rigorously analyzed as an eigenvalue problem in the coupled linear system derived from the linearized beam-core evolution equations. Assuming a C_{60}^{10+} beam with an injection energy of 10 MeV and rms emittance of 1×10^{-5} m·rad, the beam current threshold in the RAFFIA is around 225 μA.

A prototype of the RAFFIA bending magnet is manually assembled to demonstrate the properties of the real bending magnet. The idea that the change of the magnetic resistance in the magnetic flux circuits associated with excitation induces the reverse fields is confirmed.

Table of Contents

List of Figures

Chapter 1 Introduction

1.1. Cluster ion

Clusters are ensembles of several atoms or molecules that may be bound together by various type of chemical bonds. The constituents of the clusters may be the same or different atoms or molecules, and the clusters may consist of up to several million constituents. Clusters are considered an intermediate type of matter between molecules and bulk solids because their size is in the range of that of molecules and bulk solids, and their properties are different from those of their constituents or the bulk solid. The properties of the bulk remain the same when some of its atoms are added or subtracted from the bulk. In contrast, the properties of the cluster may be gradually or abruptly modified by adding or subtracting its constituents [1]. Compared with molecules, which have definite composition and geometry, clusters may have many compositions and geometries; for example, argon clusters can have four geometries. Like atoms and molecules, clusters can be ionized to form cluster ions. Thus, cluster energy can be increased by acceleration.

Ionizing cluster ions may produce high-charge cluster ions, like a single atom ion. However, Coulomb explosions are major concern for cluster ions. A highly charged C_{60} ion has achieved a charge state of up to +12 with a lifetime of over 0.5 μs [2]. The decay of highly charged cluster ions may be caused by recombination due to residual gas interactions in beam collisions between cluster ions [3] and Coulomb interaction in the cluster ion itself. The Coulomb force will increase as the charge state increases. If the Coulomb force exceeds the binding force, the cluster ion will face Coulomb explosion and decays into smaller fragment. For the case C_{60}^{Q+} ion, the Coulomb stability is

predicted to have a limit up to $Q = 14$ [4].

For acceleration, the purity of the cluster ion is important for analyzing the mass and charge state of the cluster using a magnet separator. Stable clusters formed by covalent bonding, such as C_{60} and Si_{100}, are well known.

1.2. Cluster ion sources

There are several methods that have been used to produce cluster ions. Some methods start with cluster formation, in which the cluster source is evaporated by methods such as heating, bombardment with fast particles, and exposure to high-intensity laser beams. The evaporating cluster sources form clusters via adiabatic expansion in the supersonic jet and cluster aggregation methods, and then the clusters are passed to the ionization chamber [1]. Another cluster ion method uses clusters directly. The clusters are evaporated and passed to the ionization chamber [3] where they are ionized by irradiation with fast highly charged particles, fast electrons, or high-intensity short pulse lasers.

1.2.1. Electron impact ionization

The ionization of clusters by energetic electron impact has been demonstrated with fullerene cluster ions. The energetic electron beam hits effusing neutral fullerenes at 90° (Fig. 1.1) [6]. The maximum cross section is obtained in the electron energy range of 100–300 eV and depends on the charge state. The charge states (Q) from 1 to 6, and even up to $Q = 7$ have been observed experimentally [7].
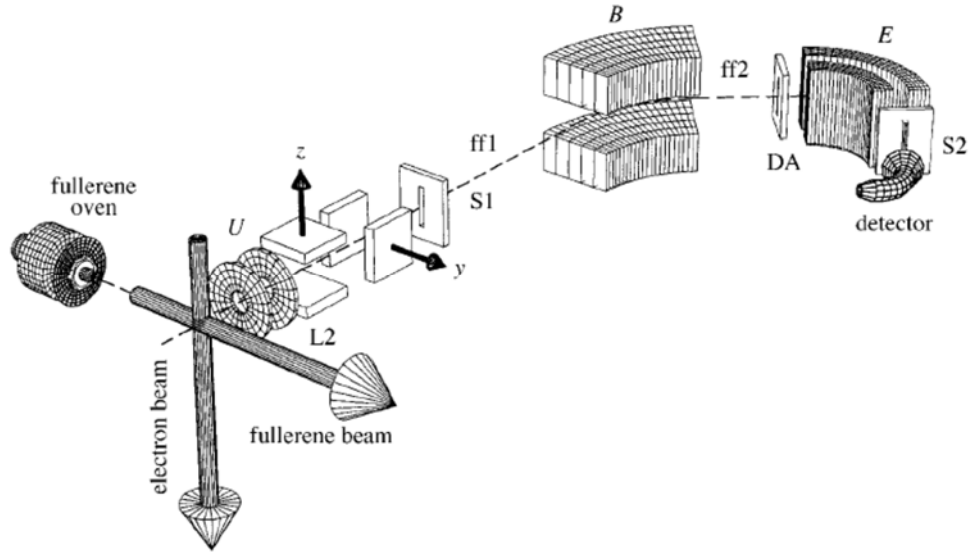
Figure 1.1: Schematic of fullerene ionization experiment using electron impact [6].

1.2.2. Ionization using highly charged heavy ion beam and laser pulse

C_{60}^{10+} cluster ions have been ionized by 280 keV Xe^{25+} bombardment [8] and by laser-induced dipole force [2]. In laser ionization, the cluster ion is produced by irradiating C_{60} with intense (10^{15} W cm^{-2}), short (70 fs), infrared (1800 nm) laser pulses [2]. Similar to electron impact ionization, the production of the C_{60} charge state by laser pulses and a Xe^{25+} beam spreads from the lower to higher charge state. So far, the 280 keV Xe^{25+} beam and laser ionization produce maximum charge states of $Q = 10$ and 12, respectively.

1.3.   Existing accelerator for cluster ions

There are several cluster ion accelerators that have produced energetic cluster ions. One is a gas cluster ion beam accelerator that is widely used for new surface modification processes. This kind of application does not need high-energy acceleration and the acceleration is usually achieved by using low DC voltages around 45 kV. Figure 1.2 shows a schematic of this machine for 1 mA argon gas cluster ion production [9]. This type of acceleration system consists of a cluster source, ionization chamber, low-

voltage acceleration electrode, optics lens, and target. For example, argon clusters are generated by adiabatic expansion of high-pressure gas through a nozzle, and then injected into the ionization chamber in a vacuum through the skimmer. The cluster ions are ionized by bombarding the clusters with electrons. Next, the cluster ions are extracted, accelerated by an electrostatic voltage, and transported to the target.
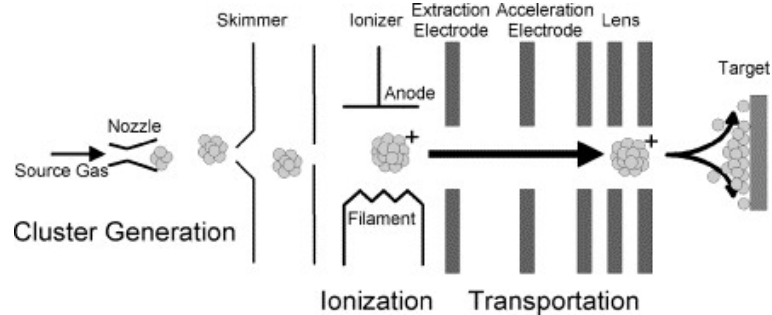
Figure 1.2: Schematic of the argon gas cluster ion acceleration system [9].

Another type of cluster ion acceleration system can provide a much higher final energy and uses an electrostatic tandem accelerator. This acceleration system was first demonstrated at the Institut de Physique Nucléaire (IPN) Orsay, France [5]. Heavy cluster ions, such as C_{60} and Au_5 ions, have been accelerated by this tandem accelerator.

In principle, a tandem accelerator has a two-stage acceleration system. The positive high voltage is generated in the terminal located in the middle of accelerator tank and the edges of the tank are grounded (Fig. 1.3). The two-stage acceleration is performed by injecting negative ions into one edge of the tank, so that the negative ions are accelerated toward the high-voltage terminal. When the negative ions reach the high-voltage terminal, they are converted to positive ions by the stripper and accelerated again to the next grounded tank edge.

Cluster ion acceleration using the IPN Orsay tandem accelerator is performed in two operation modes. The first mode is a standard operation mode, in which two-stage acceleration is used. The maximum acceleration voltage of this tandem accelerator is 15 MV. C_{60} ions with $Q = -1$ are externally injected into the tandem accelerator and a

maximum of four electrons are stripped in the charge exchange region at the center. C_{60} ions with $Q = +3$ are generated, eventually producing C_{60} ions with an energy of 60 MeV. The beam current is limited to a lower intensity due to the lower stripping cross section.

The second mode is single-end acceleration, where the positive ion beam is generated in the high-voltage terminal region and accelerated in a single-stage acceleration. The Faraday cup measurement result shows that a beam current of 300 pA for Au_2^{1+}, 110 pA for Au_3^{1+}, and 30 pA for Au_4^{1+} can be obtained in the high-voltage terminal [10].

(a)   (b)
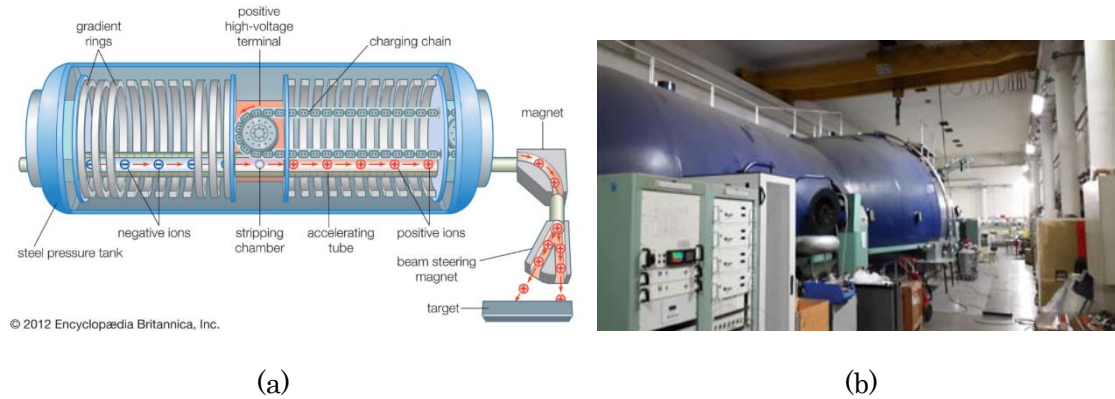
Figure 1.3: Layout (a) and photograph (b) of the tandem accelerator at IPN Orsay.

Since a successfully cluster ion acceleration using tandem accelerator and high potential for discovering a new phenomenon from cluster ion collision, cluster ion acceleration with a tandem accelerator has also been developed in Japan. The TIARA electrostatic accelerator facility at the QST-Takasaki Institute, Japan has demonstrated the acceleration of various cluster and molecular ions (B, C, O, Al, Si, Cu, Au, LiF, and AlO) using a 3 MV tandem accelerator [11].

Cluster ion acceleration using a tandem accelerator has several limitations, including high-voltage breakdown and the maximum beam current. In the two-stage acceleration mode, Q is limited and the cluster ion current is relatively small due to the stripping process. In the single-stage acceleration mode, the cluster ion source must be

embedded in the high-voltage terminal. Accommodating a cluster ion source capable of producing a high-intensity beam on a high-voltage platform of more than 10 MV is practically difficult owing to power flow.

1.4. Possible accelerator for high-energy cluster ions

1.4.1. Limitations of RF accelerators and how to overcome

To obtain giant cluster ions with higher energy, circular acceleration is necessary. RF acceleration based on an RF system consisting of an RF cavity and RF source, such as a tetrode, is not suitable because of the bandwidth limitation of the RF devices. The revolution frequency of giant cluster ions, which have large mass-to-charge ratios (A/Q > 720), is too small (order of kilohertz) at injection and increases dynamically with acceleration. This dynamic change in revolution frequency can be followed by induction acceleration. After a slow-cycling induction synchrotron was demonstrated using the KEK proton synchrotron in 2007 [12], a fast-cycling induction synchrotron showed acceleration from 50 kHz to 1 MHz in 2013 [13]. Based on these results, a racetrack-shape fixed field induction accelerator (RAFFIA) was proposed in 2015 as a unique solution to achieve repeated acceleration of giant cluster ions [14].

1.4.2. Induction accelerators

The concept of an accelerator based on induction acceleration was first proposed as the betatron by Widerøe in 1928 and realized by Kerst in the 1940s. The acceleration principle of the betatron is similar to the operational principle of a pulse transformer, where the flux change generated by the current in the primary coil induces the voltage through the secondary coil. The first betatron accelerated electrons up to 2.2 MeV [15]. Twenty years later, Christofilos and Veksler independently proposed a linear induction accelerator to generate an intense relativistic electron beam pulse. Its acceleration principle is the same as that of the betatron. However, the function of the magnetic core

in the linear accelerator is only as an acceleration voltage generator; therefore, the magnetic core is a toroid. The secondary winding is the outer metal case (Fig. 1.4). The induction cell can be arranged in series to obtain multiple accelerations. The first linear induction accelerator was the Astron injector, which began operating in 1963 and produced a 4 MeV electron beam with a current of 150 A and 250-ns-long pulse [16]. Subsequently, linear induction accelerators have been widely developed. In 1983, the Lawrence Livermore National Laboratory demonstrated the biggest induction accelerator, which had a 45 MeV beam with a current of 10 kA, called the Advance Test Accelerator [17].
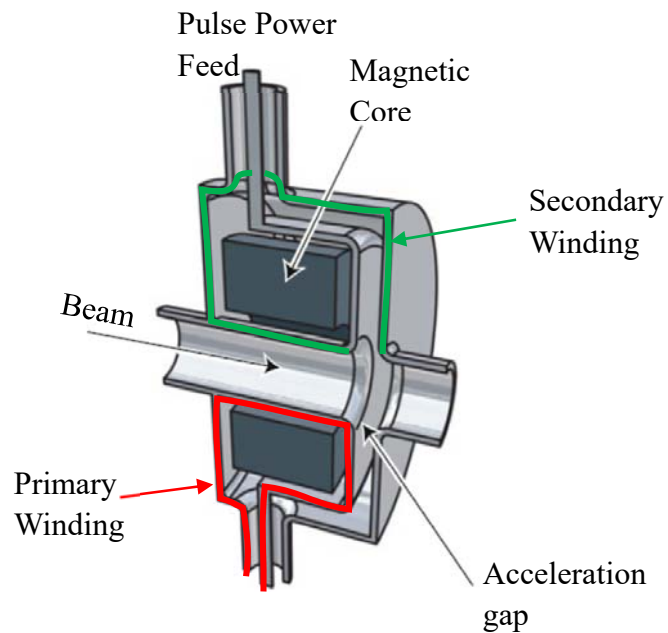
Figure 1.4: Cross section of the induction cell [17].

To reduce the length, weight, and cost of high-energy induction accelerators, accelerator scientists designed a multiple pass or recirculation acceleration scheme [18]. Concepts have been proposed for electron accelerators, including a recirculating induction accelerator [19] and a spiral line induction accelerator [20]. An induction synchrotron for replacing an RF synchrotron was proposed by Takayama and Kishiro for proton acceleration [21]. In this induction synchrotron, the functional separation of

acceleration and longitudinal confinement was introduced; thus, the beam handling in the longitudinal direction is flexible. The first demonstration of this induction synchrotron concept was performed with the KEK 12 GeV-PS [12]. Acceleration occurs in the acceleration gap of the induction cell (Fig. 1.4). When the beam passes through the induction cell, the return current, I_B, flows in the opposite direction to the beam current from the chamber wall to the transmission line (Fig. 1.5). The return current becomes a load on the pulse power supply. The important part for generating the acceleration voltage of the induction cell is the magnetic core. The magnetic core must provide a relatively high impedance to the transmission line to minimize the magnetizing current, I_C. This requirement can be satisfied by the choice of the magnetic material. The magnetic material should have high permeability, low coercive force, high flux density, and low loss at high-rate magnetization. The magnetic core material is usually ferrite or a ferromagnetic material.
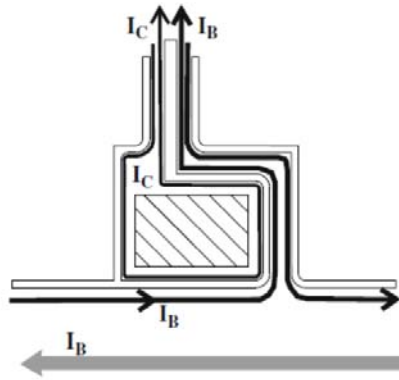
Figure 1.5: Beam loading in the induction cell.

The acceleration voltage (V_C) generation in the induction cell follows Faraday's law,

$$V_c = \frac{d\phi}{dt} \tag{1.1}$$

where $d\phi$ is magnetic flux difference during time difference (dt). The magnetic flux difference is created by magnetized the core material. The magnetization depends on the hysteresis curve of the magnetic material. As shown in the illustration, the hysteresis

shown in Fig. 1.6 is used to explain how induction voltage generate. Assuming a positive pulse V_C is generated by driving the core from $-B_r$ toward $+B_r$, the next positive V_C can be generated after the magnetic field is reset from $+B_r$ to $-B_r$.
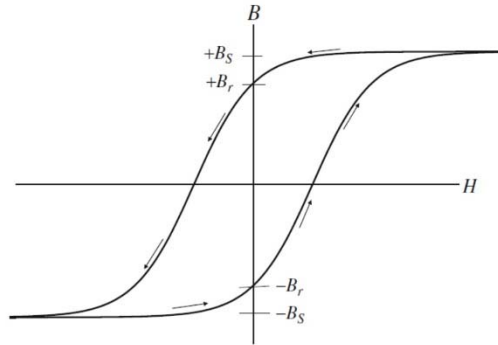
Figure 1.6: Example of a hysteresis curve of the magnetic material.

The positive and negative pulse must be supplied to the primary winding. This pulse power is provided by a modulator. The modulator consists of switching devices and a transmission line, which is usually a coaxial cable. The characteristics of the modulator are determined by the capability of the switching device. A switching device with high voltage resistance and high carrying current, short turn on/off time, high repetition rate, and long lifetime is desirable. Many switching devices, such as thyristors, magnetic switches, Si-MOSFETs, insulated-gate bipolar transistors, and silicon carbide devices, are now available. However, they have advantages and disadvantages. Therefore, the choice of switching device depends on the requirements of the application.

1.5.   Applications of cluster ions

1.5.1. General features of cluster ions interactions with materials

The interaction of energetic cluster ions with a target material typically shows non-linear effects during energy deposition in the target material, called cluster effects [22]. Because energy deposition by a cluster ion in the material is extremely localized, the stopping power is larger and the range is shorter than that of single atom or molecular

ions (Fig. 1.7). The density of the deposited energy is predicted to be huge. Material scientists expect that unknown non-equilibrium states may be generated in various materials and some states may survive beyond a transient time period as a result of quenching.
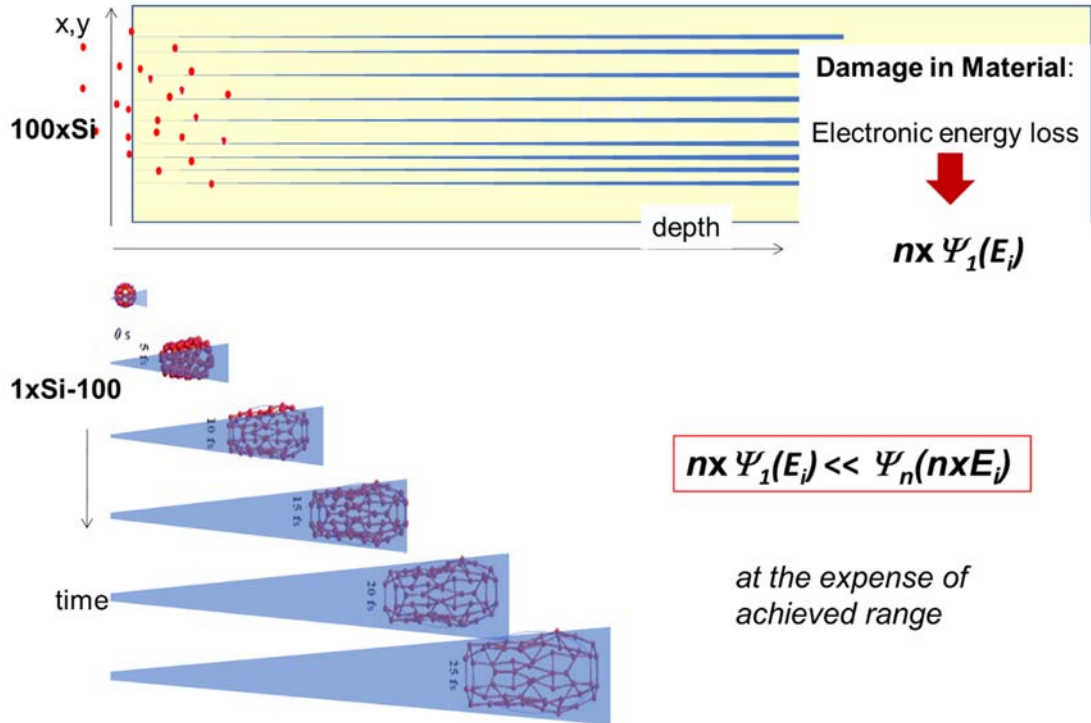
Figure 1.7: Schematic of energy deposition of single Si atom and cluster ions in a material.

1.5.2. Low energy cluster ions

Low-energy (~25 keV) cluster ions can be used for low-energy processing, extremely smooth surface processing, and precise nanometer depth etch processing. Thus, they have been widely used in new surface modification processes and have played an important role in the development of nanotechnology, including semiconductor devices, data storage devices, sensors, and transducers. In biomaterial applications, cluster ion irradiation has been studied for surface modification of

implantable medical devices in the human body and for improving biocompatibility, bio-integration, cell attachment, and cell proliferation for implanted devices [22].

1.5.3. Medium energy cluster ions

Cluster effects, such as the locally deposited energy density of fullerene ion of 5 MeV to dozens of megaelectronvolts, have been revealed by the track formation and are comparable to the deposition energy of heavy ions of hundreds of megaelectronvolts [23–25]. These effects are useful for synthesizing nanostructures or structure modification. As an example of material modification, cluster ions were used to deposit energy in a ferromagnetic film to modify the film's magnetic properties [26]. Energetic cluster ions can also can be used to increase secondary ion production in secondary ion mass spectrometry [27]. The cluster effects in the target material associated with the impact of a giant cluster ion bunch are expected to create new material phases that have never been observed under natural conditions on Earth.

Cluster ions with energies higher than 1 MeV/u could be used for plant or microorganism mutation, such as for mutation breeding of oil production algae. Giant cluster ions have major advantages compared with other irradiation sources. The ultra large size of the projectiles efficiently dissociates DNA and triggers mutations (Fig. 1.8) [28].
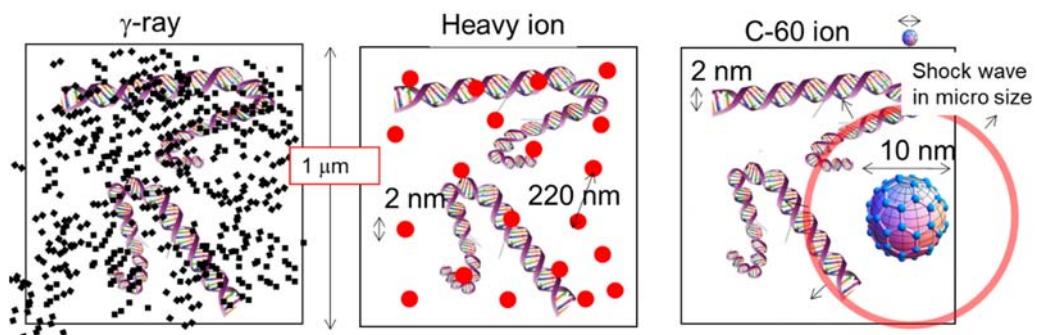
Figure 1.8: Comparison of DNA dissociation using different irradiation source.

1.5.4. High energy cluster ions

High-energy cluster ions (~40 MeV/u) are being considered as a driver beam for inertial fusion. High-energy density deposition on the deuterium–tritium target appears attractive compared with single-ion deposition in the existing heavy ion inertial fusion scenario [29]. A scheme using a two-way multiplex induction synchrotron as the main driver of inertial fusion and integrated with the RAFFIA as an injector has been proposed by a collaboration between KEK and some Japanese universities. This induction synchrotron accelerates giant cluster ions, such as Si_{-100} or C_{-60}, up to 100 GeV.

1.6. Purpose of this study and thesis structure

In this thesis, the feasibility of the RAFFIA is examined, the beam dynamics of the RAFFIA are determined, and the bending magnet with gradient and reverse field poles excited by a single set of coils is demonstrated.

The thesis structure is as follows.

Chapter 2 gives an overview of the RAFFIA, and the outline of the accelerator complex and its key devices are discussed.

In Chapter 3, the particle tracking code, which plays a crucial role in developing the linear theory discussed in Chapter 4, is described. The basic theory of the Runge-Kutta method for solving the equation of motion is reviewed. The algorithms for particle tracking code are explained.

In Chapter 4, the beam dynamics of the RAFFIA in the transverse and longitudinal direction are discussed. The linear optics approach is used to demonstrate the essential features of the RAFFIA lattice. Concepts, such as the betatron function, momentum dispersion function, closed-orbit distortion, and momentum compaction factor, are given, which can be defined for every turn. The multiparticle tracking simulation result through full induction acceleration is also described in this chapter.

In Chapter 5, a new approach based on the beam-core evolution equation to estimate the space charge effects in the RAFFIA is described. The approach is justified by a macroparticle tracking simulation and rigorous analytical theory. The approach is used to determine the beam current threshold in the RAFFIA.

In Chapter 6, the specific features of the RAFFIA magnets, which are a key device, are described. In particular, the important properties of the fixed bending magnet are explained. The excitation of the quadrupole doublets and steering magnet by acceleration is described in detail.

In Chapter 7, the prototype bending magnet is described. Its overall design, pole shape optimization, assembly process, and measurement results, such as the gap size, magnetic field excitation curve, and magnetic field profile, are discussed.

In Chapter 8, the highlights of Chapters 3, 4, 5, and 7 are summarized.

Chapter 2 Overview of RAFFIA

2.1. Outline of RAFFIA

The RAFFIA for C_{60} ($A = 720$, $Q = 10$) cluster ions is used as an example [30], where the injection energy and extraction energy are 10 and 144 MeV, respectively, and the circumference gradually changes from 49.1 to 54.3 m. An induction acceleration voltage of 10 kV per turn requires a total turn number of 1339. The size of the RAFFIA has been chosen to fit the existing space for the KEK digital accelerator.

The RAFFIA lattice consists of four 90° bending magnets (BM_i, i = 1–4) and four doublet Q magnets (QF_i/QD_i, i = 1–4) occupying the upper and lower straight sections (Fig. 2.1). The injection system and induction acceleration system are also placed on the lower straight section. A giant cluster ion beam delivered from the ion source embedded in the high-voltage platform is accelerated using the 0.8 MV induction linac and injected into the RAFFIA ring. The injection/extraction (edge) angle of the bending magnet is 45°. The orbit along the straight sections does not depend on the particle energy. Steering magnets are used for orbit correction and are placed on the straight sections, as described below. In addition, a kicker system for extraction is placed between bending magnets BM_1 and BM_2. The inward kick by the kicker gives a suitable extraction orbit from the RAFFIA ring at the downstream edge of BM_2 [31], although its details are not described in this thesis.
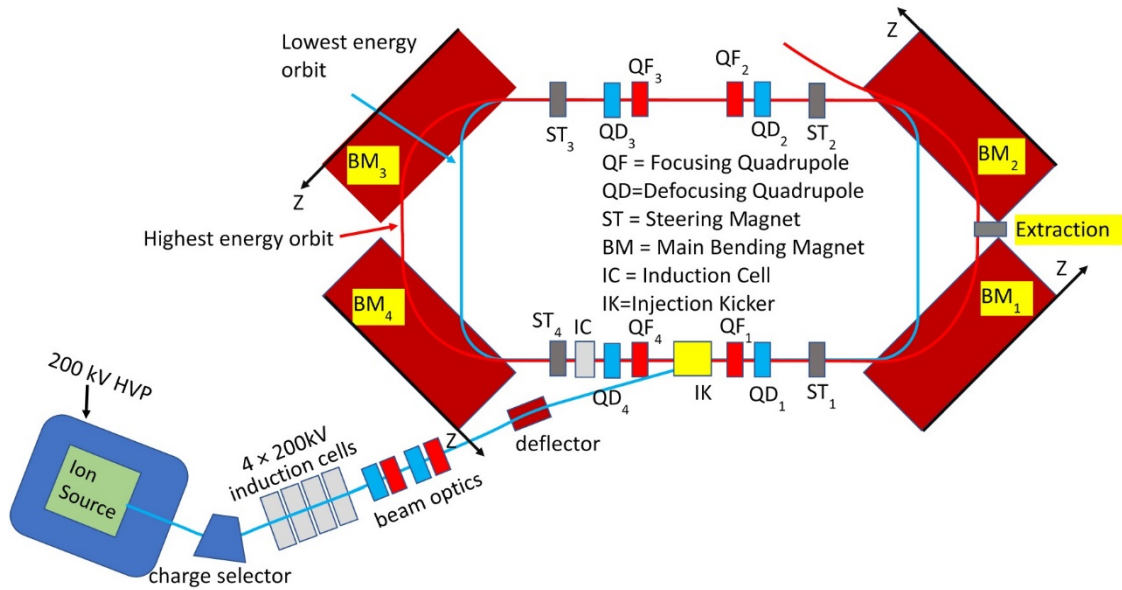
Figure 2.1: Schematic of the RAFFIA.

2.2. RAFFIA main components

2.2.1. Ion source and 200 kV high-voltage platform

The component that is most upstream of the accelerator complex is the ion source. The cluster ions are produced by electron impact ionization, which is currently being developed at Tokyo Institute of Technology [32]. A schematic and photograph of the ion source are shown in Fig. 2.2. Fullerene powders in the crucible are evaporated by the heater, and then passed to the ionization chamber. Simultaneously, electrons emitted from the filament are guided to the bias drift tube by an electric potential of up to 1 kV. The fullerenes are ionized along the electron path in the chamber. The solenoid is used to generate the focusing force for the electron and cluster ion beam. The cluster ion source is embedded in the 200 kV high-voltage platform to gain pre-acceleration.
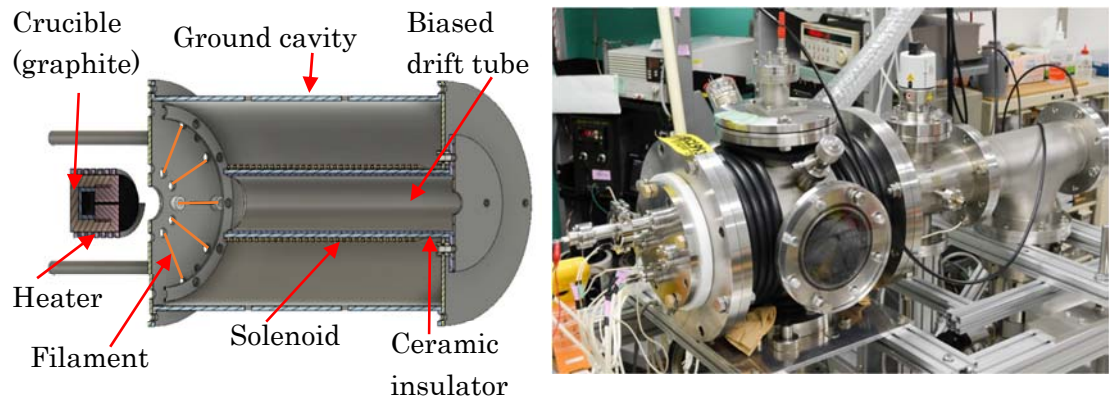
Figure 2.2: Schematic (left) and photograph (right) of the electron fullerene cluster ion source [32].

2.2.2. 0.8 MeV induction linac injector

The induction linac consists of four induction cells capable of generating a 200 kV acceleration voltage/cell. An induction cell with these specifications is currently operating in the Dual Axis Radiographic Hydrodynamic Test (DARHT) 2nd axis facility of Los Alamos National Laboratory as a radiographic facility (Fig. 2.3) [33]. The cell was assembled at the Lawrence Berkely National Laboratory in the early 2000s and can accelerate a 1.6-µs-long electron beam pulse. In the RAFFIA injector, this size of induction cell will be operated at 15 Hz.
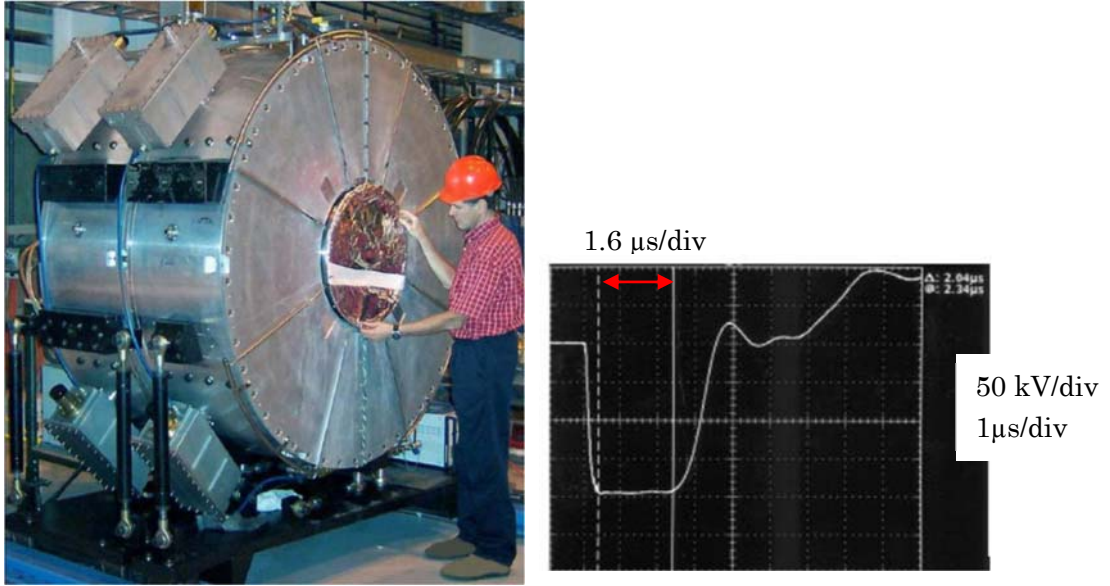
Figure 2.3: Photograph (left) and pulse profile (right) of the DARHT induction

cell [33].

2.2.3. Electrostatic injection kicker

The cluster ion beam is injected horizontally to the RAFFIA by the electrostatic injection kicker (ES-Kicker) (Fig. 2.4). The bending angle (θ_{inj}) given by the ES-Kicker is expressed as

$$\theta_{inj} = \frac{QEl}{p\beta},\tag{2.1}$$

where Q is the charge state, E is the electric field (V/m), l is the length of the ES-Kicker (m), p is the momentum (eV/c), and β is the relativistic beta. θ_{inj} is determined, considering a realistic electric field and available space. The gap size across the two electrodes (w) must satisfy

$$w > \frac{l\theta_{inj}}{2}.\tag{2.2}$$
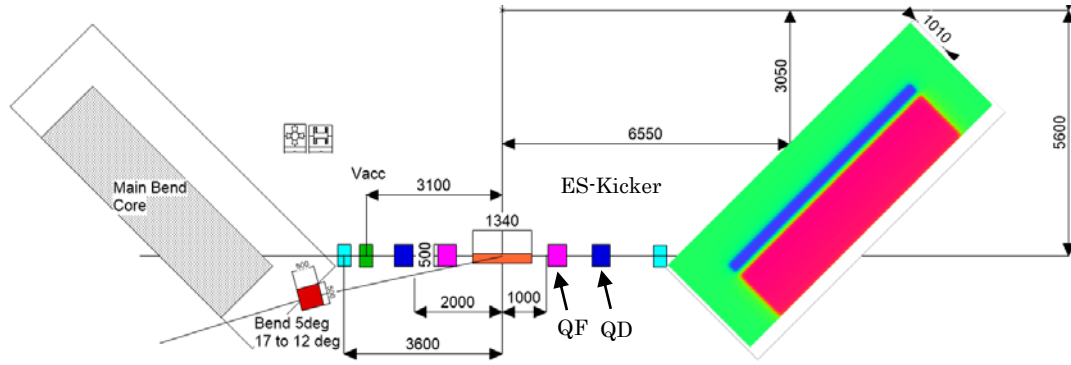
Figure 2.4: Layout of the injection region.

The ES-Kicker of the RAFFIA is similar to the existing one for the KEK-DA [34], where the field homogeneity in the kicker gap is secured by placing several intermediate electrodes between the ground and anode plates with the same distance and voltage difference (Fig. 2.5). The ES-Kicker is fully charged by a resonant charging power supply before the beam arrives and discharged before the head of the circulating beam completes the first turn. The specifications of the ES-Kicker being designed are listed in Table 2.1.

Table 2.1: Specifications of the ES-Kicker.

Parameters	
Beam kinetic energy	10 MeV (Z=10)
Beam injection angle	12 deg
Gap size between electrodes	200 mm
Vertical aperture	100 mm
Kicker length	1340 mm
Kicker Voltage	60.7 kV (+/- 30 kV)

<div align="center">(a)   (b)</div>
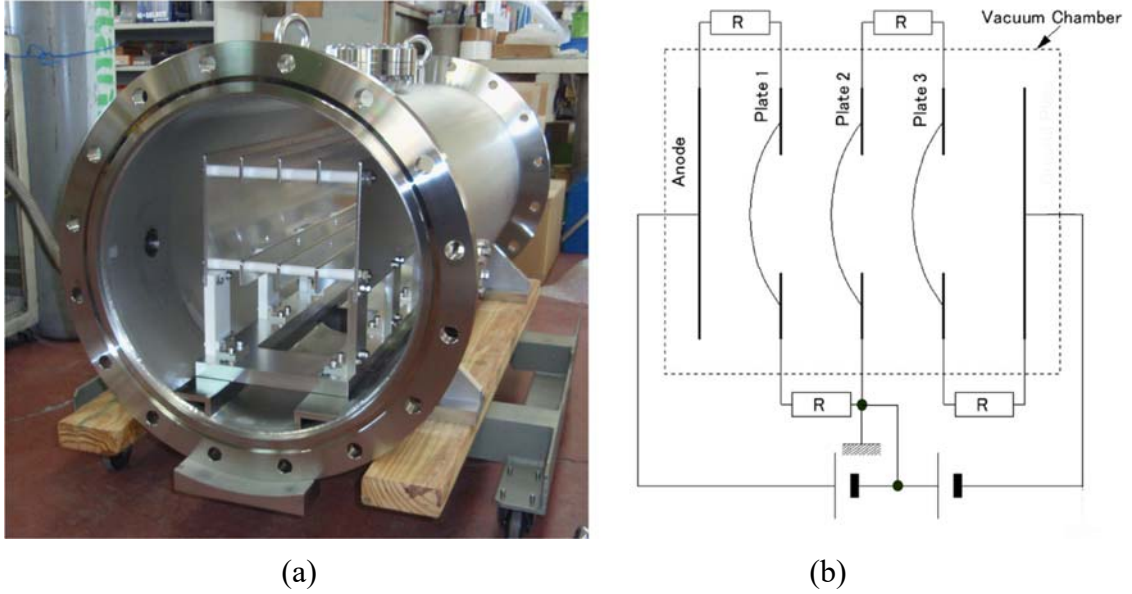
Figure 2.5: (a) Photograph of the KEK-DA ES-Kicker. (b) Equivalent circuit of the RAFFIA ES-Kicker.

2.2.4. RAFFIA ring guiding system

The racetrack-shape beam orbit of the RAFFIA is formed by four bending magnets. The bending magnets bend in the horizontal direction and focus in the vertical direction. The injection/extraction (edge) angle of 45° induces large edge defocusing in the vertical direction, which substantially affects beam motion, as discussed in Ref. [14]. The reverse field strip at the front edge and field gradient on the main pole are essential for compensating for this defocusing in the vertical direction and achieving orbit stability [14]. A schematic of the characteristics of focusing and defocusing in the vertical direction through the bending magnet region is shown in Fig. 2.6.

The main bending field and reverse field are excited with the expected flux densities in the different gaps by a single pair of excitation coils. A fraction of the magnetic flux in the main gap returns to the core front rather than to the return yoke through two magnetic flux loops due to the difference in magnetic resistance. This idea has been confirmed experimentally using a prototype bending magnet, which is described in

Chapter 7. The bending magnet is designed by using ANSYS 3D. The magnetic flux density in the y direction B_y, $\frac{dB_y}{dX}$, and $\frac{dB_y}{dZ}$ data on the median plane of the magnet gap are imported from the ANSYS 3D calculation result with a mesh size of 2 cm in the X-Z plane for the beam tracking simulation and beam dynamics calculation.
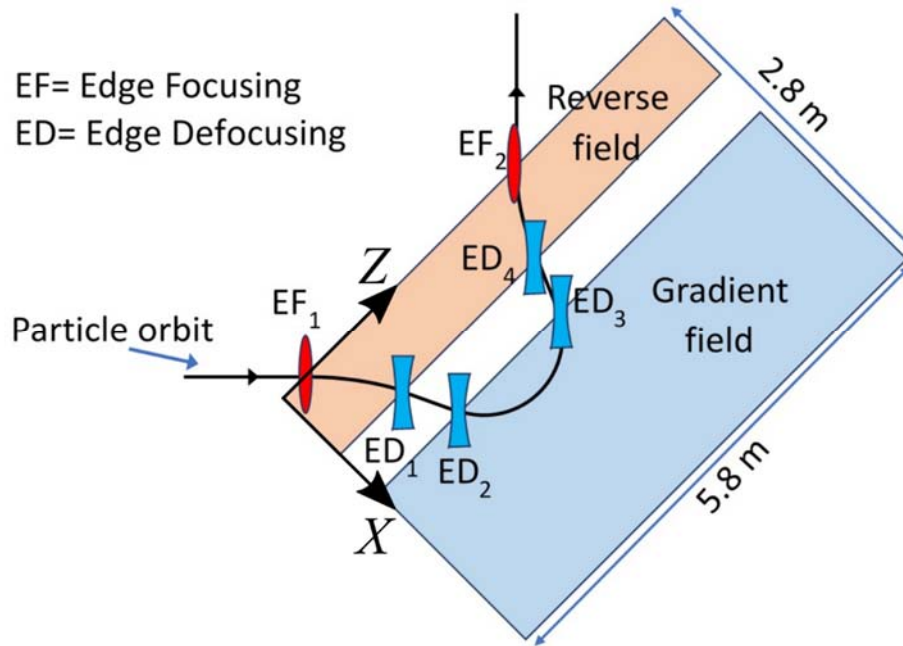
Figure 2.6: Vertical edge focusing in the bending magnet.

The orbit stability is ensured by using four quadrupole doublets. Due to the energy dependence of the particle orbit in the fixed bending field with the gradient, the optical strength of the guiding field varies with the turn or time. Thus, the gradient fields of the quadrupole doublets must follow this variation. The orbit stability of the RAFFIA can be achieved by optimized ramping of the gradient fields of the quadrupole magnets. The other component related to the orbit stability is a steering magnet. The intrinsic magnetic field non-uniformity along the longitudinal direction of the bending magnet becomes the main source of closed-orbit distortion. Four steering magnets are required to minimize closed-orbit deformation.

2.2.5. Induction acceleration system

The induction acceleration system of the RAFFIA is similar to that used in the KEK induction synchrotron. Two sets of induction cells are used for different purposes. The first set of induction cells provides a 10 kV acceleration voltage per turn and another set of induction cells generates a barrier voltage for beam confinement. These induction cells are energized by the switching power supply, where high-power solid-state switching elements are mounted.

The core material of the induction cell is thin Finemet tape and the cell generates an output voltage of 3 kV. To obtain the acceleration voltage of 10 kV, four induction cells are required for the RAFFIA. One further cell is used for beam confinement. The compact switching power supply driving the induction cell, in which SiC-MOSFETs that can operate at 1 MHz are used as switching elements, is under development [35].

2.2.6. Extraction kicker

To extract the cluster ion beam from the RAFFIA, a kicker located between BM_1 and BM_2 is proposed. The orbit position at the beam extraction region shown in Fig. 2.7 (a) shifts gradually outward as the energy increases. The x position of the beam centroid is shown as a function of the turn number in Fig. 2.7 (b). The extraction kicker is fired at the last turn.

(a)   (b)
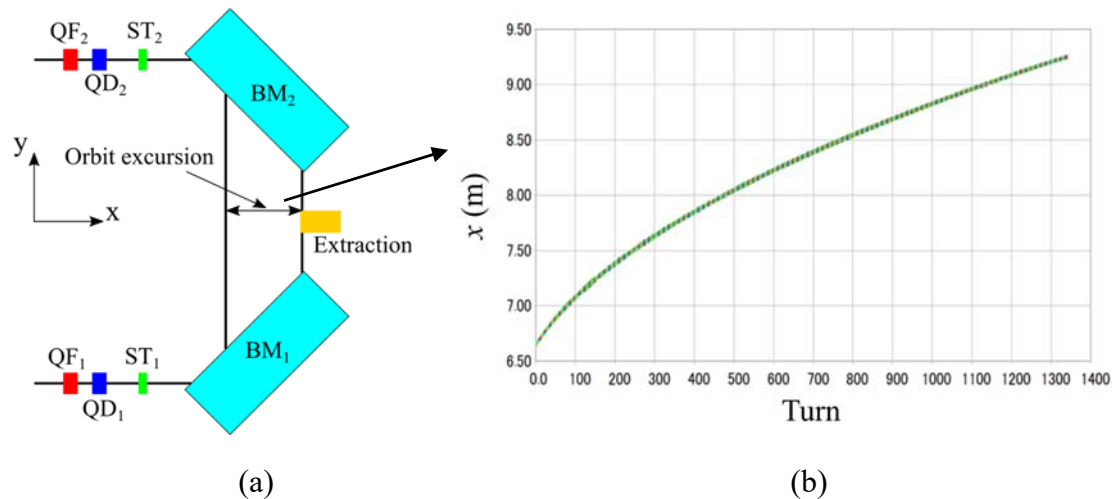
Figure 2.7: (a) Extraction kicker location and (b) orbits excursion in the region between BM$_1$ and BM$_2$.

The orbit at the extraction energy that is inwardly kicked by the kicker with 0.32 T·m is shown in Fig. 2.8. The simulation result implies that the inward kick before entering BM$_2$ is suitable to extract the beam at the exit of the BM$_2$.
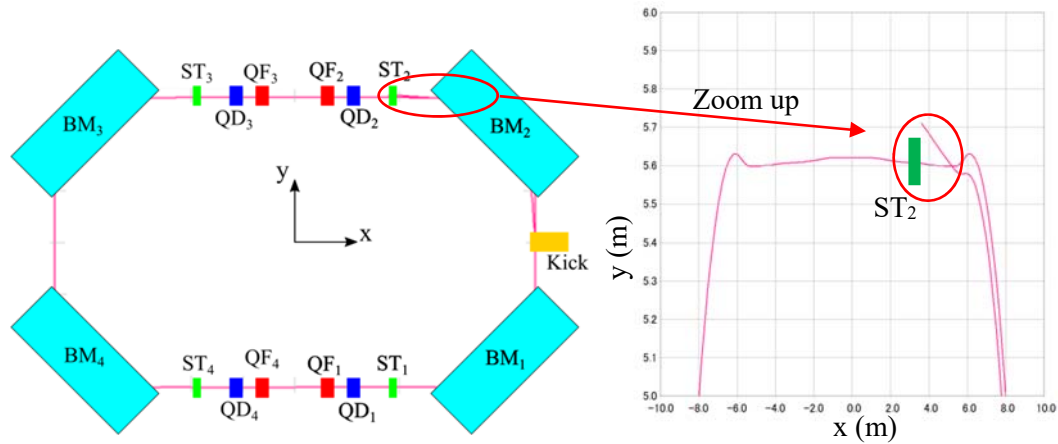
Figure 2.8: The orbit at extraction energy with kicker.

2.3. Induction acceleration system

The main components of the induction acceleration system are an induction cell and modulator. The induction cell is excited by a pulse current supplied by the modulator and the pulse timing is synchronized with the particle revolution. The switching power supply has an H-bridge configuration like that of the modulator used in the KEK induction synchrotron. The positive pulse is generated by simultaneously turning on S1 and S4 (Fig. 2.9), and the negative pulse is generated by simultaneously turning on S2 and S3.
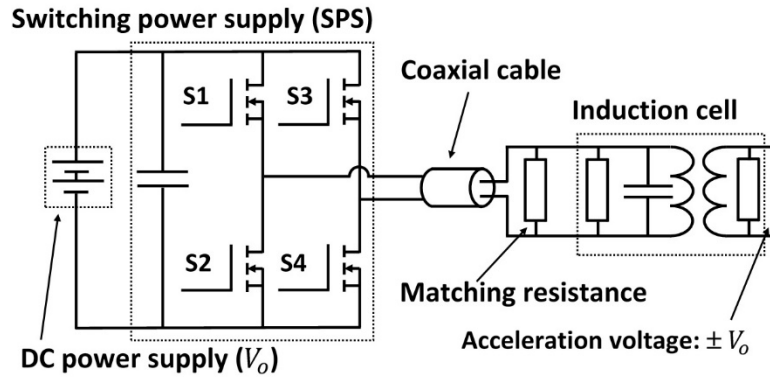
Figure 2.9: Equivalent circuit of the induction acceleration system.

The acceleration voltage (V_{ac}) and barrier voltage (V_{bb}) are generated across the acceleration gaps at every turn (Fig. 2.10). For confinement, two V_{bb} pulses of pulse length ϕ_{pulse} are generated with a phase duration ($\Delta\phi$) between the negative pulse and positive pulse. The beam bunch must be confined between two barrier pulses, and then accelerated with V_{ac}. The length of a beam bunch is varied by controlling the trigger signal of the barrier voltage pulses. This method should be effective for extracting bunches with the desired length by the kicker system at the end of acceleration, as described in the literature related to induction acceleration [17].
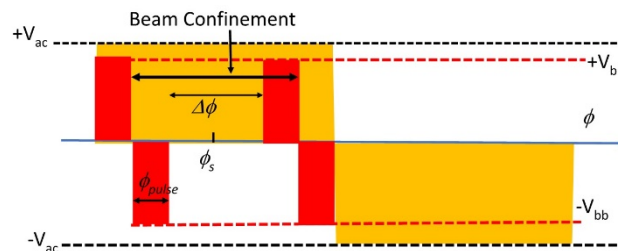
Figure 2.10: Pulse profiles of V_{ac} and V_{bb}.

Chapter 3 Particle tracking code

3.1. Equation of motion and Runge-Kutta method

Particle motion under the influence of electromagnetic field follows the equation of motion,

$$\frac{d\boldsymbol{p}}{dt} = m\gamma\frac{d^2\boldsymbol{r}}{dt^2} = q\left(\boldsymbol{E}(\boldsymbol{r}) + \frac{\boldsymbol{p}\times\boldsymbol{B}(\boldsymbol{r})}{m\gamma}\right) \tag{3.1}$$

where $\boldsymbol{p}$ is momentum, t is time, m is the particle mass, γ is the Lorentz factor, $\boldsymbol{r}$ is the position vector, q is the particle charge, $\boldsymbol{E}$ is the electric field, and $\boldsymbol{B}$ is the magnetic field. The Lorentz equation is a second-order ordinary differential equation but we can write it in two stage first-order differential equation by introducing

$$\frac{d\boldsymbol{r}}{dt} = \frac{\boldsymbol{p}}{m\gamma}. \tag{3.2}$$

Analytical solving of the equation of motion in three dimensions is complicated. Thus, a numerical method is used by solving Eq. (3.1) and Eq. (3.2).

In general form, the first order differential equation can be written in this form

$$\frac{dy}{dt} = f(t, y), \tag{3.3}$$

where $f(t, y)$ is an arbitrary derivative function. The ordinary differential equation with a known initial condition can be solved numerically through an approximate value from its derivative function at small step size (h). The simple method to solve Eq. (3.3) is by Euler's rule approximation as written in the following form,

$$y(t_{n+1}) = y(t_n) + hf(t, y), \tag{3.4}$$

where n is the step id and $h = t_{n+1} - t_n$. However, the Euler's method still has a big error from the truncation of the Taylor series. As we know, the Taylor series is written in this form,

$$y(t_{n+1}) = y(t_n) + hf\big(t_n, y(t_n)\big) + \frac{1}{2!}h^2 f'\big(t_n, y(t_n)\big) + \frac{1}{3!}h^3 f''\big(t_n, y(t_n)\big) + \cdots,$$

$$(3.5)$$

Here, the Euler's method is truncated at the second term of right hand side (RHS). Thus, the error is function of h^2 ($O(h^2)$).

Runge-Kutta (RK) method offers better truncation error correction than the Euler's method. This truncation error depends on the order of RK method. The differential equation solution solved by RK method is based on the integral form of Eq. (3.3) which can be written in this

$$y_{n+1} = y_n + \int_{t_n}^{t_{n+1}} f(t, y)dt. \qquad (3.6)$$

To make easier for understanding RK method, we derive RK2 (2nd order RK method) algorithms by expand $f(t, y)$ in Taylor series up to two terms at the midpoint of the integration limit,

$$f(t, y) = f\big(t_{n+1/2}, y_{n+1/2}\big) + \big(t - t_{n+1/2}\big)\frac{df}{dt}\big(t_{n+1/2}\big) + O(h^2), \qquad (3.7)$$

The term $\big(t - t_{n+1/2}\big)$ in the interval $t_n \leq t \leq t_{n+1}$ equals to positive or negative. Thus, this term will eliminate each other in the integration of $f(t, y)$ at that interval

$$\int_{t_n}^{t_{n+1}} f(t, y)dt \simeq f\big(t_{n+1/2}, y_{n+1/2}\big)h + O(h^3), \qquad (3.8)$$

and

$$y_{n+1} \simeq y_n + hf\big(t_{n+1/2}, y_{n+1/2}\big) + O(h^3). \qquad (3.9)$$

As we can see the, the Euler's rule and RK2 have the same number of terms but the RK2 give better precision. In order to solve by RK2, the $y_{n+1/2}$ must be obtained. The following Euler's rule

$$y_{n+1/2} \simeq y_n + \frac{1}{2}h\frac{dy}{dt} = y_n + \frac{1}{2}hf(t_n, y_n). \qquad (3.10)$$

By using this definition, the RK2 can be written in this form

$$y_{n+1} \simeq y_n + k_2 \tag{3.11}$$

where $k_2 = hf\left(t_n + \frac{h}{2}, y_n + \frac{k_1}{2}\right)$ and $k_1 = hf(t_n, y_n)$ [36].

The fourth-order RK method (RK4) can be obtain by approximating y with Taylor series up to third terms or second order term. The RK4 equation can be written in the following form

$$y_{n+1} = y_n + \frac{1}{6}(k_1 + 2k_2 + 2k_3 + k_4) \tag{3.12}$$

where $k_1 = hf(t_n, y_n)$, $k_2 = hf\left(t_n + \frac{h}{2}, y_n + \frac{k_1}{2}\right)$, $k_3 = hf\left(t_n + \frac{h}{2}, y_n + \frac{k_2}{2}\right)$, and $k_4 = hf(t_n + h, y_n + k_3)$. The RK4 will have smaller truncation error than RK2 in the order of $O(h^5)$.

The RK derivation and its family are also can be obtained by using Butcher tableau. In this method, the RK is written in general form.

$$y_{n+1} = y_n + h\sum_i^s b_i k_i \tag{3.12}$$

where

$$k_1 = f(t_n, y_n)$$
$$k_2 = f(t_n + c_2 h, y_n + h(a_{21}k_1))$$
$$k_3 = f(t_n + c_3 h, y_n + h(a_{31}k_1 + a_{32}k_2))$$
$$\vdots$$
$$k_s = f\left(t_n + c_s h, y_n + h(a_{s1}k_1 + a_{s2}k_2 + \cdots + a_{s,s-1}k_{s-1})\right),$$

s is the number of stage, a_{ij} is the Runge-Kutta matrix, b_i and c_i are known as the weights and the nodes. These data are written in the following Butcher tableau

$$
\begin{array}{c|ccccc}
0 & & & & & \\
c_2 & a_{21} & & & & \\
c_3 & a_{31} & a_{32} & & & \\
\vdots & \vdots & & \ddots & & \\
c_s & a_{s1} & a_{s2} & \cdots & a_{s,s-1} & \\
\hline
 & b_1 & b_2 & \cdots & b_{s-1} & b_s.
\end{array}
$$

The RK method is consistent when $\sum_{j=1}^{i-1} a_{ij} = c_i$ for $i = 2,\dots, s$. The number of stage (s) is usually equal to the RK order (p) but for $p \geq 5$, s may be larger than p [37]. The Butcher tableau of RK2 in Eq. (3.11) and RK4 are shown in Fig. 3.1.

$$
\begin{array}{c|cc}
0 & & \\
1/2 & 1/2 & \\
\hline
 & 0 & 1
\end{array}
\qquad\qquad
\begin{array}{c|cccc}
0 & & & & \\
1/2 & 1/2 & & & \\
1/2 & 0 & 1/2 & & \\
1 & 0 & 0 & 1 & \\
\hline
 & 1/6 & 1/3 & 1/3 & 1/6
\end{array}
$$

Figure 3.1: Butcher tableau for RK2 (left) and RK4(right)

For particle tracking simulations, the equation of motion is evaluated by the RK4. The RK4 solution for Eq. (3.1) and (3.2) is shown in Appendix A.

3.2. Algorithms of particle tracking code

The flowchart of the particle tracking code is shown in Fig. 3.2. The RK method is only used in the bending magnets and quadrupole magnets section, whereas a kick approximation is used in the steering magnet and acceleration section. The magnetic field data in the quadrupole is assumed to be an ideal field that is determined by its field gradient. Meanwhile, the magnetic fields in the bending magnet are obtained from the expansion of a discrete magnetic field data on the median plane. Expansion of the magnetic fields beyond the grid points on the median plane are obtained in a way of linear interpolation between adjacent points. B_y in the upper and lower regions of the

median plane is assumed to be equal to B_y on the median plane. Meanwhile B_X and B_Z in the upper and lower regions of the median plane are expressed in the forms expanded to the first order of y. The reference orbit is calculated, assuming that the bending magnet fields are uniform along the Z-direction and the fields itself at the center of magnet (origin of Z direction) obtained from the ANSYS 3D calculation. The field is called an ideal field in the paper. The initial position of the particle is defined at the center of the lower straight section (Fig. 2.1).
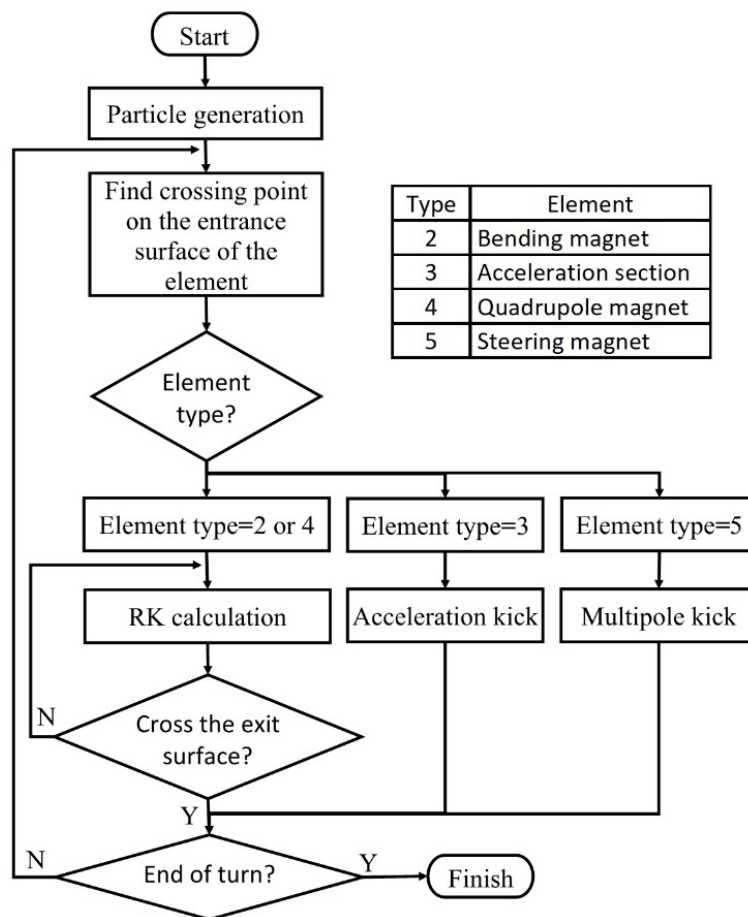
Figure 3.2: Flowchart of the particle tracking code.

Chapter 4 Beam dynamics of RAFFIA [38]

4.1. Transverse motion

4.1.1. Linear optics approach

The transverse motion of the particles around the reference orbit, known as betatron motion, is defined by Hill's equation

$$Y'' + K(s)Y = 0, \tag{4.1}$$

where Y is the transverse coordinate, s is the longitudinal coordinate, and $K(s)$ is the restoring force coefficient. Hill's equation can be solved by a linear optics approach using a transfer matrix. In the transfer matrix form, the transverse motion calculation is defined by

$$\bar{Y}_{s_1} = M_{s_0 \to s_1} \cdot \bar{Y}_{s_0}, \tag{4.2}$$

where $\bar{Y}$ is the vector for the transverse position in phase space and M is a 2×2 transfer matrix. For the orbit stability of the circular accelerator, a one-turn transfer matrix (M_T), which is obtained by multiplying the sequence of M, must satisfy the stable condition where

$$\left| \frac{Trace \ (M_T)}{2} \right| \leq 1. \tag{4.3}$$

A stable orbit indicates that the particles motion in one turn is always confined around a closed orbit.

The transfer matrix represents the optical properties of the devices around the reference orbit. Therefore, the reference orbits for the stable motion must be known to determine the transfer matrix. As the particle orbits in the RAFFIA gradually change with acceleration, the closed orbit must be found for every turn.

The reference orbit is calculated by applying ideal bending magnet data in the particle tracking code. The ideal bending magnet data is assumed to be uniform along the Z-direction and the fields itself at the center of magnet (origin of Z direction) obtained from the ANSYS 3D calculation as shown in Fig. 4.1. A stable orbit is obtained if the transfer matrix satisfies Eq. (4.3). The quadrupole doublets are the only parameter that can be adjusted to obtain stable closed orbits.

(a)

(b)
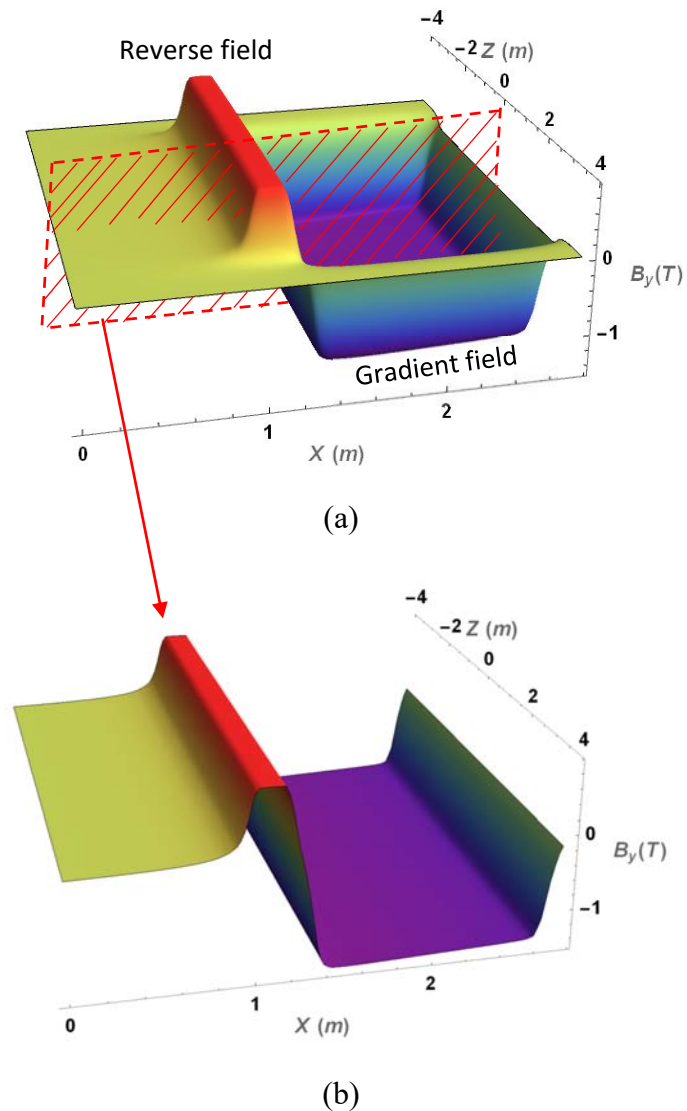
Figure 4.1: (a) two-dimension bending magnet field data obtained from ANSYS 3D calculation and (b) ideal bending magnet field data which is extended from the data at the origin of Z direction.

Typical tracking results in the global coordinate system are shown in Fig. 4.2. One-turn transfer matrices can be defined every turn by running N-particle tracking. By generating N-particles in the phase space, the elements of the transfer matrix are given in terms of the least squares fit by

$$\begin{pmatrix} Y_k \\ Y'_k \end{pmatrix}_{n+1} = M_T \begin{pmatrix} Y_k \\ Y'_k \end{pmatrix}_n = \begin{pmatrix} m_{11} & m_{12} \\ m_{21} & m_{22} \end{pmatrix} \begin{pmatrix} Y_k \\ Y'_k \end{pmatrix}_n, \tag{4.4.a}$$

$$\chi^2 = \sum_{k=1}^N \left\{ \left(Y_k^{(n+1)} - m_{11} Y_k^{(n)} - m_{12} Y'_k^{(n)} \right)^2 + \left(Y'_k^{(n+1)} - m_{21} Y_k^{(n)} - \right. \right.$$

$$\left. m_{22} Y'_k^{(n)} \right)^2 \right\} = \min , \tag{4.4.b}$$

where k is the particle number and n is the turn number.
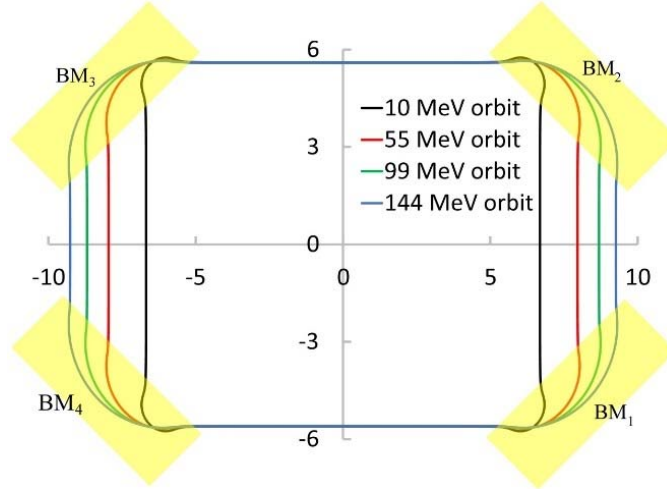
Figure 4.2: Typical tracking results.

4.1.2. Beta function

The beam size is important in designing an accelerator and one of the contributions to the beam size is defined by $(\varepsilon\beta)^{1/2}$, where ε is the emittance and β is the beta function. The beta function determines the beam envelope, which describes the outermost betatron motion of the beam. To be derived from Hill's equation, β depends on the lattice of the machine. β and the other Twiss parameters (α and γ) are calculated from the transfer matrix by

$$\begin{pmatrix} \beta \\ \alpha \\ \gamma \end{pmatrix}_{s_2} = \begin{pmatrix} m_{11}^2 & -2m_{11}m_{12} & m_{11}^2 \\ -m_{21}m_{11} & 1+2m_{12}m_{21} & -m_{12}m_{22} \\ m_{21}^2 & -2m_{22}m_{21} & m_{22}^2 \end{pmatrix} \begin{pmatrix} \beta \\ \alpha \\ \gamma \end{pmatrix}_{s_1}, \quad (4.5)$$

where m is the component of the 2×2 transfer matrix, M.

The beta function of the RAFFIA at the injection and extraction energy are shown in Fig. 4.3. The vertical beam envelope (β_V) is much bigger than that for the horizontal beam envelope (β_H). The horizontal and vertical beam envelopes are maximum in the QF and QD, respectively. At the injection energy, the value of β_H maximum, β_H minimum, β_V maximum, and β_V minimum are 47.097 m, 0.038 m, 327.62 m, and 1.550 m, respectively. Meanwhile, at the extraction energy, the value of β_H maximum, β_H minimum, β_V maximum, and β_V minimum are 15.515 m, 1.99 m, 305.481 m, and 1.752 m. Fig. 4.3 also shows that the beam envelope at the extraction energy is smaller than the beam envelope at the injection energy.
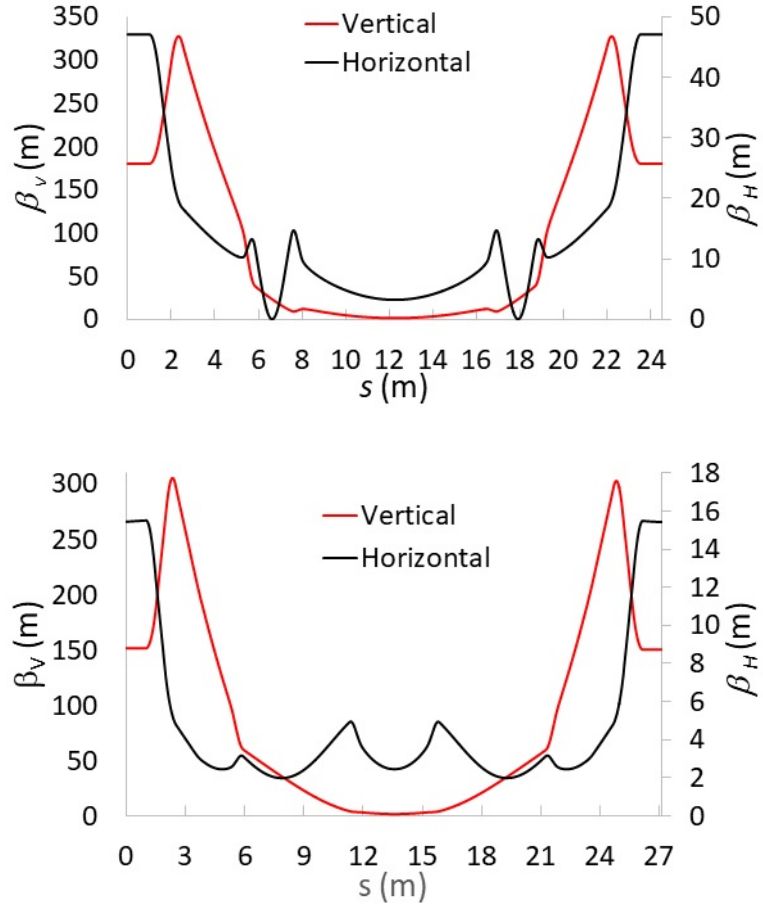
Figure 4.3: Beta-function in the half lattice of the RAFFIA at injection (upper) and extraction energy (lower).

4.1.3. Dispersion function

The particles with $\Delta p/p$ perform their horizontal betatron oscillations around a different orbit from the reference particle. This motion is described by Eq. (4.1) with additional $(\Delta p/p)/\rho$ in the right-hand side of the equation. With this additional term, Eq. (4.1) becomes an inhomogeneous differential equation. The general solution of the equation is

$$x(s) = x_\beta(s) + x_{eq}(s), \tag{4.6}$$

where x_β is the homogeneous solution that represents the betatron motion and x_{eq} is the particular solution that represents the displacement of the betatron oscillation center.

The particular solution of the inhomogeneous equation is given by

$$D(s) = \frac{\sqrt{\beta(s)}}{2\sin(^\mu/_2)} \int_s^{s+C} \left(\frac{1}{\rho(s')}\right) \sqrt{\beta(s')} \cos[^\mu/_2 - |\Psi(s) - \Psi(s')|] \, ds', \quad (4.7)$$

where dispersion function $D = x_{eq}/(\Delta p/p)$, μ is the phase advance, and Ψ is the betatron phase. The dispersion function can also be calculated with a 3×3 transfer matrix by

$$\begin{pmatrix} D \\ D' \\ 1 \end{pmatrix}_{s_2} = \begin{pmatrix} m_{11} & m_{12} & m_{13} \\ m_{21} & m_{22} & m_{23} \\ 0 & 0 & 1 \end{pmatrix} \begin{pmatrix} D \\ D' \\ 1 \end{pmatrix}_{s_1}, \quad (4.8)$$

where D' is the derivative of D with respect to s, and m_{13} and m_{23} are matrix components from the particular solution. The dispersion function is calculated by Eq. (4.8) from the linear optics particle tracking.

In the particle tracking simulation, the dispersion function can be approximated by comparing a reference particle orbit with an off-momentum particle orbit. Both particle orbits are obtained by running the particle tracking code. The distance between the reference orbit and off-momentum orbit is defined as x_{eq}. Multi-turn data without acceleration is used to correct the small residual oscillation.

The dispersion functions of the RAFFIA at the injection and extraction energy are shown in Fig. 4.4. The dispersion functions from the linear optics and particle tracking simulations show almost consistent results. The discrepancy may come from the kick approach in the linear optics when calculating the H-V coupling, as discussed in the previous section. Fig. 4.3 shows that the dispersion function at the injection energy is much smaller than at the extraction energy. We previously obtained the maximum $\Delta p/p$ of 0.41% from injecting carbon ions into the fast-cycling induction synchrotron (KEK digital accelerator) [39]. Assuming the maximum $\Delta p/p$ at the injection energy

34

is 0.41%, the maximum x_{eq} is 5.3 mm, which is still sufficient small. Even though the maximum dispersion function at the extraction energy is almost three times bigger than at the injection energy, $\Delta p/p$ at the extraction energy may decrease due to the acceleration. The calculation result also shows that the location of the acceleration device in the straight section has a small dispersion function. Therefore, the emittance blows up caused by synchro-beta coupling can be avoided [40].
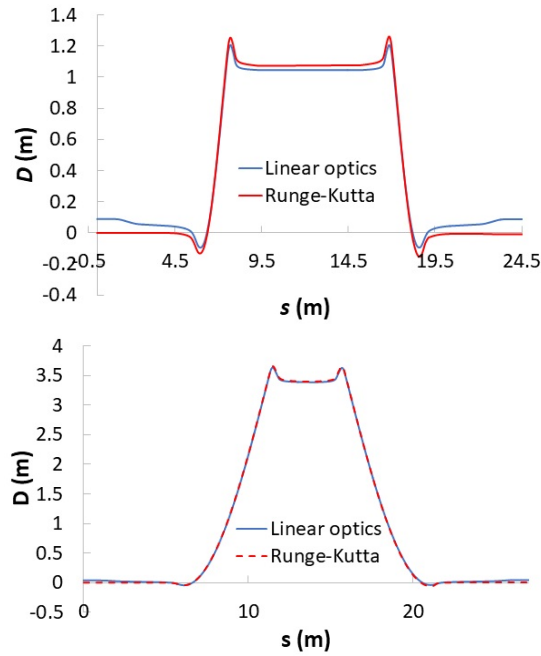
Figure 4.4: Dispersion function of RAFFIA at injection (upper) and extraction (lower) energy.

4.1.4. Closed orbit distortion

The magnetic fields of the actual bending magnet may be different from the magnetic field that is used in the design. This difference is the magnetic field error (ΔB_y), which generate closed orbit distortion (COD). In a usual synchrotron, the COD arose from any unpredicted magnetic field imperfections in the accelerator ring and can be minimized by the steering magnet (ST) system in the well-established manner.

In the RAFFIA, an ideal magnetic field that is uniform along the longitudinal

direction of the magnet is used in the orbit design. As a matter of fact, a non-uniform magnetic field originated from the finite size of the bending magnet in Z direction is induced, as shown in the designed magnetic field in Fig. 4.5. Even though the bending magnet design has been optimized, the non-uniformity is still remained more or less. This non-uniform magnetic field is considered as the specific magnetic field error (ΔB_y), which induces an intrinsic COD. As shown in Fig. 4.5, a particle experiences a different ΔB_y for each turn because the particle orbit in the bending magnet varies with acceleration. Therefore, the COD can be considered as the predictable time-varying COD.
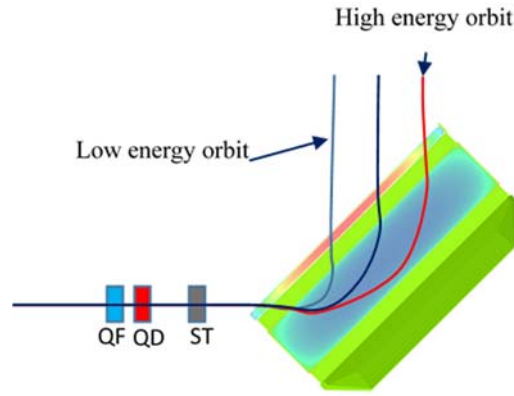
Figure 4.5: Magnetic field contour and particle orbits in the bending magnet of the RAFFIA.

In the linear optics approach, the COD can be calculated by the following equation

$$X_{COD}(s) = \frac{\sqrt{\beta(s)}}{2\sin(\mu/2)} * \int_s^{s+C} \left\{-\frac{\Delta B_y(s')}{B\rho}\right\} \sqrt{\beta(s')} \cos\left[\mu/2 - |\Psi(s) - \Psi(s')|\right] ds'.$$

$$(4.9)$$

On the other hand, the COD is obtained by subtracting that in the case of the ideal magnetic field from a closed orbit in the case of the non-uniform magnetic field. Both closed orbits are obtained by running the particle tracking code with zero emittance. The closed orbit is obtained by scanning the initial position in the phase-space. The resultant CODs of the RAFFIA at the injection energy are shown in Fig. 4.6. The results from the

linear optics approach and simulation are in good agreement with each other.

To compensate for the COD, an additional magnetic field is applied by using four steering magnets. For the injection energy, the optimum correction is performed by setting the steering magnet field to 0.0277 T m.
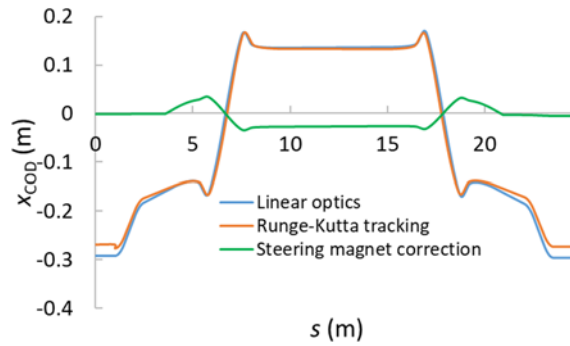
Figure 4.6: Bare COD at the injection energy and its corrected one.

4.2. Analysis of tracking results

In order to confirm the stable acceleration of cluster ion beams in the transverse direction, the macroparticle tracking of a gaussian beam over the entire acceleration cycle is carried out, assuming the discrete and constant step acceleration voltage. Here, we will show two tracking results using ideal bending magnet field data (Fig. 4.1 (b)) and using two-dimension bending magnet field data (Fig. 4.1 (a)).

4.2.1. Tracking results using ideal bending magnet field data

Figure 4.7 (a) and (b) show the temporal evolution of the beam sizes from injection to extraction, where the horizontal beam size changes with a typical adiabatic dumping associated with acceleration and the vertical beam size goes through blow-up in the several regions of turns. However, it is noted that any beam loss is not observed in the macroparticle tracking.
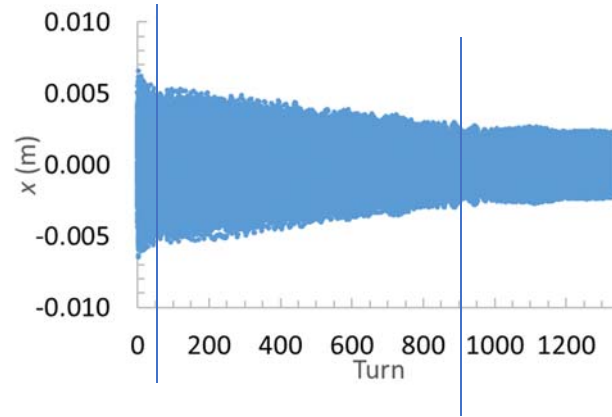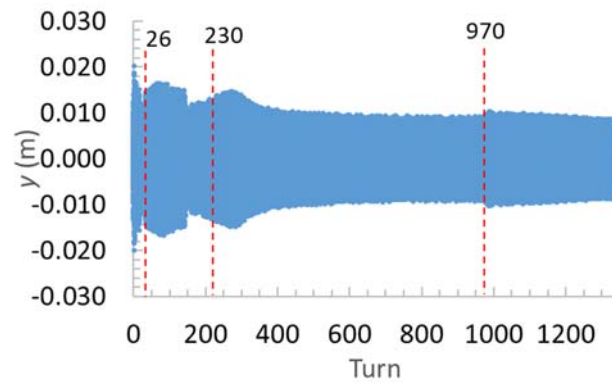
Figure 4.7: The beam size during acceleration in (a) Horizontal monitored at the QF
and (b) vertical monitored at QD.

To manifest what causes this beam size growth, the temporal evolution of betatron tunes and their foot-prints are evaluated from the tracking results and shown in Fig. 4.8. The vertical beam size growth observed around 26, 230, and 970 turns seems to be driven by the 4th-order nonlinear resonance, which is usually originated from the octupole magnetic component. This nonlinear component is likely in the bending magnet with gradient.

One can conclude that the beam size blow-up is not fatal and still acceptable without introducing any countermeasure, although it is desired to further reduce the octupole component in the bending magnet design.
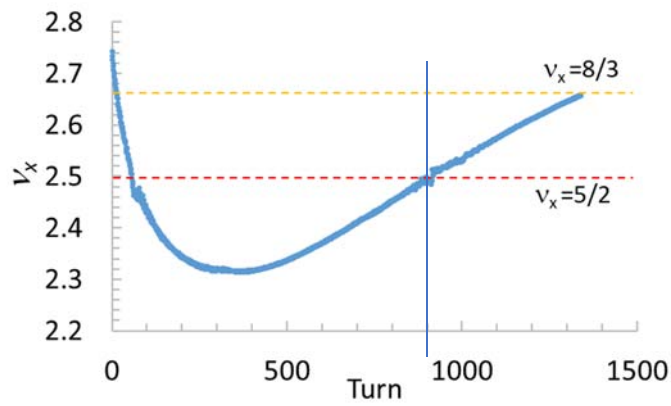
(a)
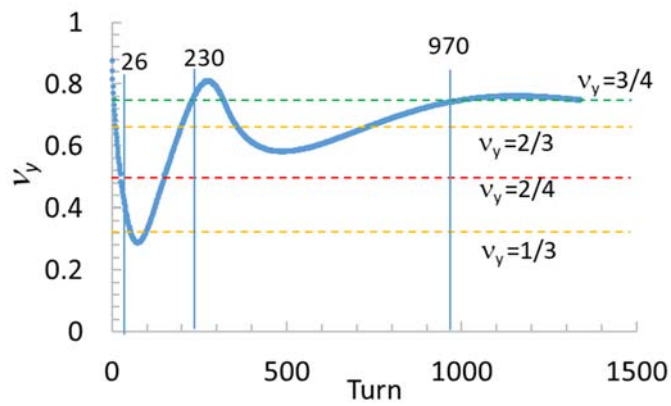
(b)
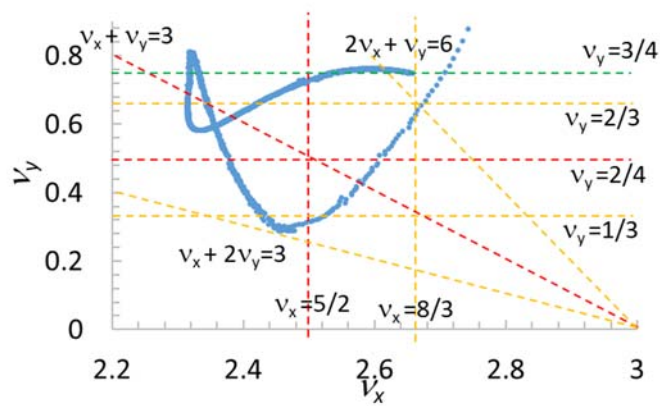
(c)

Figure 4.8: (a) Horizontal tune vs. turn number, (b) vertical tune vs. turn number, and

(c) tune foot-print

4.2.2. Tracking results using two-dimension bending magnet field data

In this macroparticle tracking, the orbit stability is obtained by ramping the gradient field of the quadrupole doublets and the magnetic field of the steering magnets as shown in Fig. 4.9. Unlike the case of ideal bending magnet field data, the ramping steering magnets are required because the large COD is generated due to the field non-uniformity along the *Z*-direction of the bending magnet.
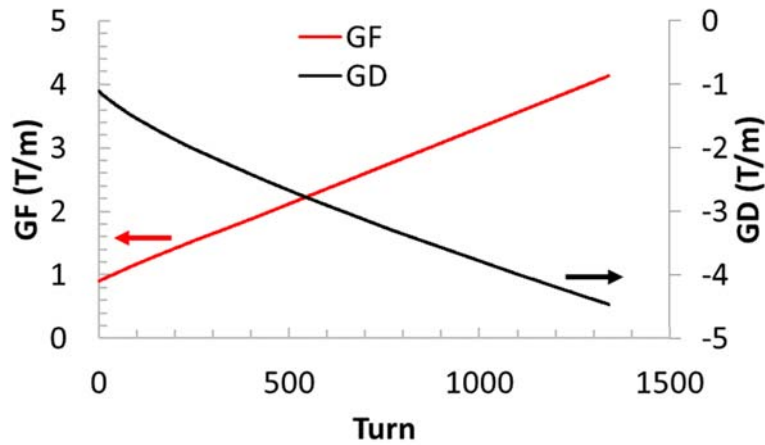
(a)
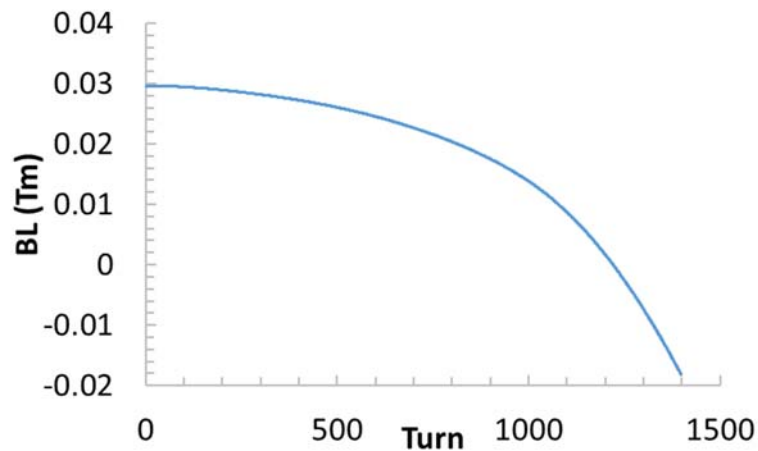
(b)

Figure 4.9: Ramping pattern of quadrupole doublet (a) and steering magnet (b).

The temporal evolution of the beam sizes from injection to extraction are shown in Fig. 4.10 (a) and (b) where both the beam sizes blow-up in the horizontal and vertical direction are observed at the several regions of turns. The beam loss is not observed in the macroparticle tracking.
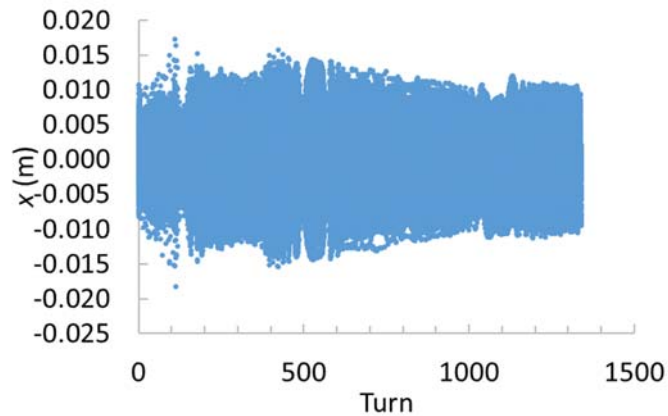
(a)
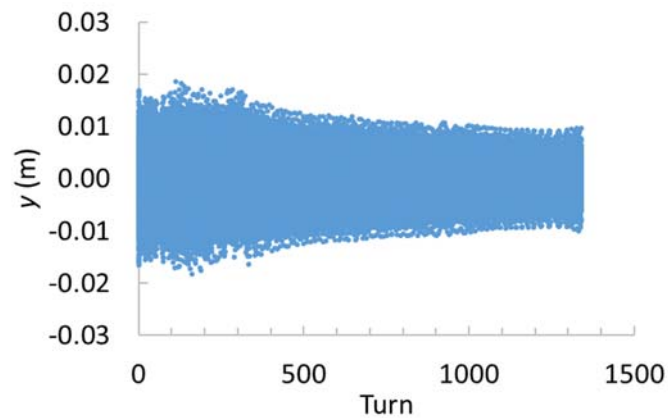
(b)

Figure 4.10: The beam size during acceleration in (a) Horizontal direction monitored at the QF and (b) vertical direction monitored at QD.

The beam size growths are analyzed from the temporal evolution of betatron tunes and their foot-prints which are evaluated from the tracking results and shown in Fig. 4.11. The horizontal beam growth at 110 and 400 turns caused by crossing half integer resonance $v_x = 5/2$, and at 1100 turns caused by crossing third integer resonance $v_x =$

41

8/3. In the vertical direction, the beam growth at 120 and 300 turns may caused by crossing third integer resonance $v_x = 1/3$. Although the tunes pass the coupling resonance line at early stage of acceleration, the effects are not significant. The beam size growths may be attributed to the sextupole field components in the bending magnet.

(a)

(b)
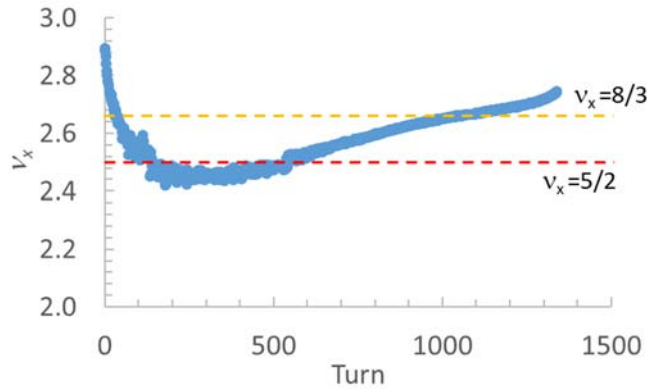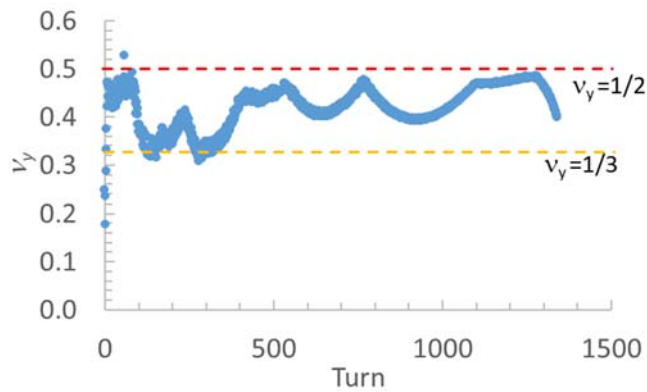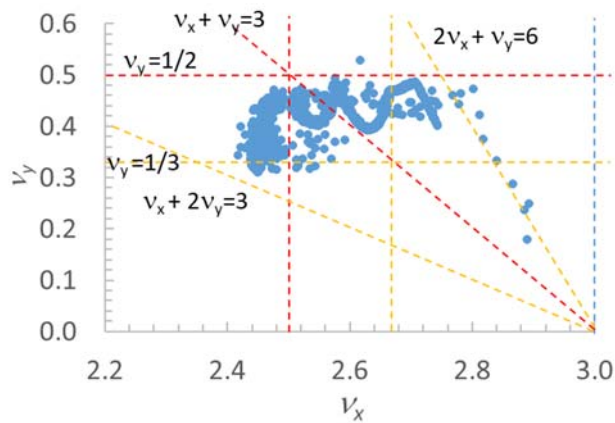
Figure 4.11: (a) Horizontal tune vs. turn number, (b) vertical tune vs. turn number, and

(c) tune foot-print.

4.3. Longitudinal motion

4.3.1. Injected cluster bunch

The motion of the particle in the longitudinal direction is mainly determined by the acceleration device. The particles continue to be accelerated and confined by the acceleration voltage (V_{ac}) and barrier voltage (V_{bb}). The injected particles are usually distributed in the longitudinal direction with slightly different energy (ΔE) and phase (ϕ) to the synchronous particle. In this calculation, the energy of the injected particle is assumed to follow a normal distribution with some variance, whereas the initial phase of the particle follows a uniform distribution with a width of 50°.

4.3.2. Trapping and acceleration

The longitudinal motion of the particles that are injected to the RAFFIA are defined by the acceleration equation for the induction accelerator

$$\begin{cases} (\Delta E)_{n+1} = (\Delta E)_n + q[V_{bb}(\phi_n) - V_{ac}] \\ \phi_{n+1} = \phi_n + \frac{2\pi\eta_{n+1}}{(\beta_{n+1}^s)^2 E_{n+1}^s}(\Delta E)_{n+1} \end{cases}, \qquad (4.10)$$

where E is the particle energy, n is the turn number, q is the particle charge, β is the relativistic beta, $\eta = \alpha - \frac{1}{(\gamma^s)^2}$ is the slippage factor, γ is the Lorentz factor, $\alpha = \frac{1}{C}\oint\frac{D(s)}{\rho}ds$ is the momentum compaction factor, and C is the circumference of the closed orbit. Superscript s denotes the synchronous particle. The calculation result shows that the momentum compaction factor of the RAFFIA increases with particle energy (Fig. 4.12). This feature of the RAFFIA is different from a synchrotron, which has a constant

momentum compaction factor.
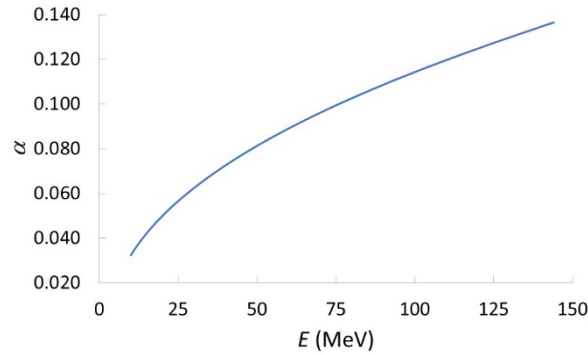
Figure 4.12: Momentum compaction factor of the RAFFIA varying with acceleration.

In this calculation, we set V_{bb} to be 1 kV, the phase of the beam center, ϕ_{pulse}, to 12°, and the phase distance between two barrier voltages, $\Delta\phi$, to 24°. An induction cell generates a 10 kV acceleration voltage between the two barrier voltage pulses. $\Delta p/p$ and ϕ of the injected particles are generated by following a normal distribution and a uniform distribution, respectively. The longitudinal motion is calculated from the injection energy to the extraction energy, and the phase space distributions at the beginning and extraction energy are shown in Fig. 4.13. The calculation result shows that the momentum deviation decreases at the extraction energy as expected and two barrier voltages confine the beam to a size of $\Delta\phi$. The final longitudinal beam size can be varied by controlling $\Delta\phi$.
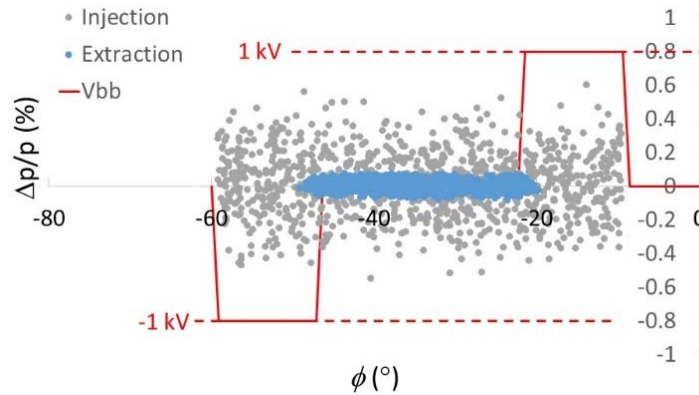
Figure 4.13: Longitudinal phase plot at injection and extraction.

4.3.3. Beam loss

During acceleration, some particles with high $\Delta p/p$ may not be confined. The unconfined particles are lost due to a finite momentum aperture of the RAFFIA ring. The maximum $\Delta p/p$ of the particles that are confined depends on the barrier voltage according to

$$\left(\frac{\Delta p}{p}\right)_{max} = \frac{1}{\beta^s}\sqrt{\frac{1}{|\eta|}\left(\frac{qV_{bb}}{E^s}\right)\frac{2\tau_{pulse}}{T_0}}, \tag{4.11}$$

where τ_{pulse} is the barrier pulse width and T_0 is the time period for a single turn. For a barrier voltage of 1 kV, $\left(\frac{\Delta p}{p}\right)_{max}$ is obtained as 0.58 % at the injection energy. Fig. 4.14 shows the survival rate of the particles when the standard deviation (σ) of $\Delta p/p$ is varied. Because $\Delta p/p$ decreases at each turn, particle loss occurs only at the early stage of acceleration. At $V_{bb} = 1$ kV, a 100% survival rate can be achieved at a maximum of $\sigma = 0.193$ %.
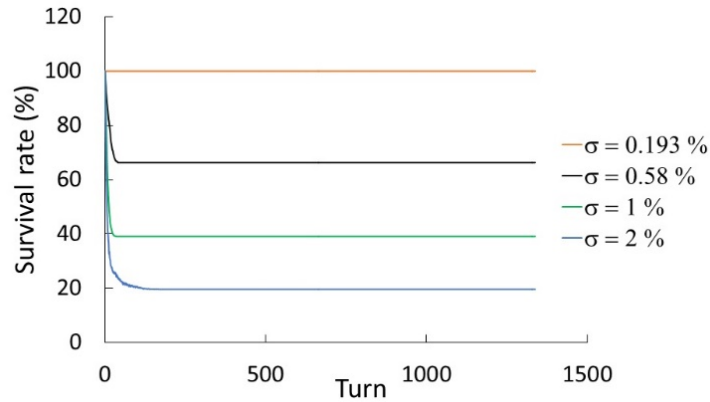
Figure 4.14: Survival rate of the ions as function of σ at V_{bb}=1kV

Chapter 5 Space charge effects in the RAFFIA [41]

5.1. Introduction

Space-charge effects in circular accelerators have long been a major problem in synchrotron beam dynamics. In particular, space-charge effects are crucial in high-intensity beam accelerators such as IFMIF drivers [42], heavy ion inertial fusion drivers [43], and neutron source drivers for nuclear waste transmutation [44]. The space-charge effects primarily determine the acceptable beam current in circular induction accelerators, where extremely low-velocity injection is allowed due to the intrinsic nature of induction acceleration [45], with no limitation on the revolution frequency.

Space-charge effects on beam motion in various accelerators have been extensively studied by theoretical and numerical approaches assisted by computer simulations. A typical example of a numerical approach is the multi-particle simulation based on the particle-in-cell (PIC) scheme [46]. This method mimics realistic beam motion; however, it usually requires an extremely long CPU time, proportional to the total number of macroparticles, beam guiding elements, and turn numbers. Other studies have used the beam-core envelope equation model (BCEEM). The BCEEM, which is derived from the betatron equation perturbed with the linearized space-charge forces, has been used to analyze the characteristics of halo formation in a uniform linear focusing channel [47,48]. When the global behavior of the beam is more important than the motion of individual particles, the BCEEM is suitable, for example, to discuss coherent motion, such as the beam-core breathing enhanced by the space-charge forces. The BCEEM produces results consistent with the multi-particle simulation results based on the PIC method [49]. The BCEEM has also been used to analyze the nonlinear resonance and chaotic behavior of intense charged-particle beams in the periodic solenoidal focusing channel [50]. However, most studies have discussed the evolution of beam

envelope through a uniform linear focusing channel where the beam shape is assumed to be cylindrical and a one-dimensional envelope equation is used.

Recently, a three-dimensional envelope model has been developed to study beam halo formation [51] and the envelope instability of a bunched beam in the periodic focusing channel with RF focusing in the longitudinal direction [52]. The subject and approach discussed in Ref. 52 are close to those in the present study, although the discussion in the present study is limited to the transverse direction. The discussion in Ref. 52 is not generic due to the specific assumption that the focusing channel consists of 1-m-long cells with 0.2-m-long focusing and defocusing quadrupoles. From the results in Ref. 39, it is unclear how the beam-core evolves as it passes through the periodic cells, how this depends on the beam current, and whether the beam current threshold leading to the catastrophic beam-core instability can be predicted clearly.

In this chapter, we focus on the evaluation of the space-charge effects in the transverse direction by using beam-core evolution equation. Coupled nonlinear beam-core evolution equations are derived by linearizing the perturbed betatron equation, assuming the Gaussian beam distribution from injection to a certain time period. Justification of the coupled nonlinear beam-core evolution equation is performed by using proton acceleration in KEK DA lattice. Beam-core evolution predicted from the evaluated nonlinear beam-core evolution equations is justified by macroparticle tracking simulations through a long-term revolution for various beam currents. The results are presented visually by Poincaré mapping on the (σ, dσ/ds) space. Rapid change in the beam-core evolution is observed above a beam current threshold. The feature is confirmed by the rigorous stability analysis of the coupled and linearized beam-core evolution equations. We arrive at an important definition of the space-charge limit for the beam-core instability. It is theoretically shown that onset of this instability corresponds to period-doubling bifurcation of the elliptical point in the beam-core phase space.

5.2. Analytically evaluated beam-core evolution equation with space-charge effects

A beam model with an elliptic cross-section of the Gaussian distribution is assumed. The particle distribution is uniform in the longitudinal direction with a bunch length of L. The charge distribution is written as

$$\rho(\boldsymbol{r}) = \frac{NQe}{2\pi\sigma_x\sigma_y L} \exp\left[-\frac{x^2}{2\sigma_x^2} - \frac{y^2}{2\sigma_y^2}\right], \tag{5.1}$$

where $\boldsymbol{r}$ is the vector position (x, y, z), x and y are the transverse coordinates, z is the longitudinal direction, N is the number of particles included in a bunch, Q is the charge state, e is the unit charge, and σ_x and σ_y are the standard deviations of the beam size in the x- and y-directions, respectively. The space-charge potential, φ, is analytically given in the mathematically closed form [53] by

$$\varphi(x, y; s) = \frac{NQe}{4\pi\varepsilon_0 L} \int_0^\infty \frac{\exp\left[-\frac{x^2}{2\sigma_x^2+t} - \frac{y^2}{2\sigma_y^2+t}\right]}{\sqrt{(2\sigma_x^2+t)(2\sigma_y^2+t)}} dt. \tag{5.2}$$

where ε_0 is the permittivity in a vacuum and t is the integration variable. Space-charge force F generated by the beam is given by

$$\boldsymbol{F} = Qe(\boldsymbol{E} + \boldsymbol{v} \times \boldsymbol{B}) = \frac{Qe\boldsymbol{E}}{\gamma^2} = -\frac{Qe}{\gamma^2}\nabla\varphi, \tag{5.3}$$

where $\boldsymbol{E}$ is the space-charge electric field, $\boldsymbol{v}$ is the beam velocity, $\boldsymbol{B}$ is the beam current-induced magnetic flux density, and γ is the Lorentz factor. Thus, the particle motion affected by the space-charge forces is described by

$$\begin{cases} \frac{d^2x}{ds^2} + K_x(s)x = \frac{F_x}{Amc^2\beta^2\gamma} \\ \frac{d^2y}{ds^2} + K_y(s)y = \frac{F_y}{Amc^2\beta^2\gamma} \end{cases}, \tag{5.4}$$

where c is the speed of light, β is the relativistic factor, $K_x(s)$ and $K_y(s)$ are the restoring coefficients in the betatron motion in both directions, A is the mass number, and m is the

proton rest mass. Substituting Eq. (2) into (4) gives

$$\begin{cases} \dfrac{d^2x}{ds^2} + K_x(s)x - \dfrac{2}{\beta^3\gamma^3} \cdot \left(\dfrac{I_B}{I_0}\right) \cdot x \cdot \displaystyle\int_0^\infty \dfrac{\exp\left[-\dfrac{x^2}{(2\sigma_x^2(s)+t)} - \dfrac{y^2}{(2\sigma_y^2(s)+t)}\right]}{(2\sigma_x^2(s)+t)^{3/2}(2\sigma_y^2(s)+t)^{1/2}} \cdot dt = 0 \\[3em] \dfrac{d^2y}{ds^2} + K_y(s)y - \dfrac{2}{\beta^3\gamma^3} \cdot \left(\dfrac{I_B}{I_0}\right) \cdot y \cdot \displaystyle\int_0^\infty \dfrac{\exp\left[-\dfrac{x^2}{(2\sigma_x^2(s)+t)} - \dfrac{y^2}{(2\sigma_y^2(s)+t)}\right]}{(2\sigma_x^2(s)+t)^{1/2}(2\sigma_y^2(s)+t)^{3/2}} \cdot dt = 0 \end{cases} \tag{5.5}$$

where I_B is the beam current and $I_0 = \left(\dfrac{A}{Q}\right) \cdot \dfrac{4\pi\varepsilon_0 mc^3}{e}$ is the Alfven current for an ion

with mass number A and charge-state Q. Assuming that particles in the beam-core region performing small amplitude oscillation are exerted by the linearized space-charge forces, the equations of motion for those particles   are

$$\begin{cases} \dfrac{d^2x}{ds^2} + \left[K_x(s) - \dfrac{2}{\beta^3\gamma^3} \cdot \dfrac{(I_B/I_0)}{\sigma_x(\sigma_x+\sigma_y)}\right]x = 0 \\[1.5em] \dfrac{d^2y}{ds^2} + \left[K_y(s) - \dfrac{2}{\beta^3\gamma^3} \cdot \dfrac{(I_B/I_0)}{\sigma_y(\sigma_x+\sigma_y)}\right]y = 0 \end{cases} \tag{5.6}$$

The envelope equation that corresponds to Eq. (6) is written straightforwardly as

$$\begin{cases} \rho''_x + \left[K_x(s) - \dfrac{k}{\sqrt{\varepsilon_x}\cdot\rho_x(s)\cdot\{\sqrt{\varepsilon_x}\rho_x(s)+\sqrt{\varepsilon_y}\rho_y(s)\}}\right] \cdot \rho_x = \dfrac{1}{\rho_x^3} \\[1.5em] \rho''_y + \left[K_y(s) - \dfrac{k}{\sqrt{\varepsilon_y}\cdot\rho_y(s)\cdot\{\sqrt{\varepsilon_x}\rho_x(s)+\sqrt{\varepsilon_y}\rho_y(s)\}}\right] \cdot \rho_y = \dfrac{1}{\rho_y^3} \end{cases} \tag{5.7}$$

where $k = \dfrac{2}{\beta^3\gamma^3} \cdot \left(\dfrac{I_B}{I_0}\right)$, $\sigma_{x,y} = \sqrt{\varepsilon_{x,y}} \cdot \rho_{x,y}(s)$, $\rho_{x,y} = \sqrt{\beta_{x,y}}$, $\beta_{x,y}$ is the beta

function in the transverse direction, and $\varepsilon_{x,y}$ is the emittance in the transverse direction, corresponding to the 1σ beam. Assuming that the beam-core size equals the standard deviation of the beam size, the coupled nonlinear beam-core evolution equations are derived straightforwardly from Eq. (5.7) as

$$\begin{cases} \dfrac{d^2\sigma_x}{ds^2} + K_x(s)\sigma_x(s) - \dfrac{k}{\sigma_x(s)+\sigma_y(s)} = \dfrac{\varepsilon_x^2}{\sigma_x(s)^3} \\[1.5em] \dfrac{d^2\sigma_y}{ds^2} + K_y(s)\sigma_y(s) - \dfrac{k}{\sigma_x(s)+\sigma_y(s)} = \dfrac{\varepsilon_y^2}{\sigma_y(s)^3} \end{cases} \tag{5.8}$$

The perturbing terms originating from the space charge effects are proportional to k, which is a function of I_B and β^3. In the KEK-DA, β is very small at injection; therefore, the space charge effects are most significant at injection. The coupled nonlinear beam-core evolution Eq. (5.8) can be easily solved by a numerical method, such as the Runge-Kutta method. However, there is no proof whether Eq. (5.8) stands over a long period. First, we must confirm that the beam-core evolution can be followed by Eq. (5.8) over many turns.

5.3. Justification of the nonlinear beam-core evolution equation by the macro particle tracking approach

The KEK-DA synchrotron lattice with simple 8-fold symmetry that consists of eight combined function-type magnets is chosen in order to justify Eq. (5.8). Its parameters are given in Appendix A. First, the beam-core evolutions are obtained by solving Eq. (5.8) using the Runge-Kutta method, and then they are evaluated by statistically manipulating the result of the macroparticle tracking simulation, where $\sigma_x = \sqrt{\frac{\Sigma(x_i - \bar{x})^2}{N}}$ and $\sigma_y = \sqrt{\frac{\Sigma(y_i - \bar{y})^2}{N}}$. In the macroparticle tracking simulation based on Eq. (5.6), the reference orbit, that is, the s-axis, is divided into segments 2 mm in size. The 4×4 transfer matrix is calculated for every segment, refreshing the standard deviations of σ_x and σ_y in the restoring coefficient in Eq. (5.6) at the beginning of each segment, and the motions of individual particles are followed by the linear transformation method,

$$X^i_{j+1} = M^* \cdot X^i_j \tag{5.9}$$

where X is the transverse vector, j is the segment ID along orbit s, and i is the particle ID. We call this approach the renormalized space-charge matrix approach (RSMA). A Gaussian distribution is used to generate $N = 10^4$ macroparticles at the beginning, and vector X^i of each macroparticle is tracked by Eq. (5.9). The beam-core information of σ_x, σ'_x, σ_y, and σ'_y at the fixed observation point on the orbit axis is exported every turn

for Poincaré mapping.

Two Poincaré maps over 300 turns that are obtained by the coupled nonlinear beam-core evolution approach (CNBCEA) and the RSMA results are shown on the same phase space for the same initial conditions and different beam currents in Fig. 5.1. The initial beam-core vectors, (σ_x, σ'_x) and (σ_y, σ'_y), seem to deviate slightly from the matched beam-core vectors, which are defined as the center point of the ellipse. Even so, the two Poincaré maps are similar to each other for the assumed beam currents. Even at 300 μA, the Poincaré maps suggest similar phase space structures. This fact indicates that the CNBCEA is justified by the macroparticle tracking. CNBCEA has a major advantage that the evaluation time is several seconds, whereas the evaluation time for RSMA is 129 min on a normal PC.

(a)

(b)

51

(c)

(d)
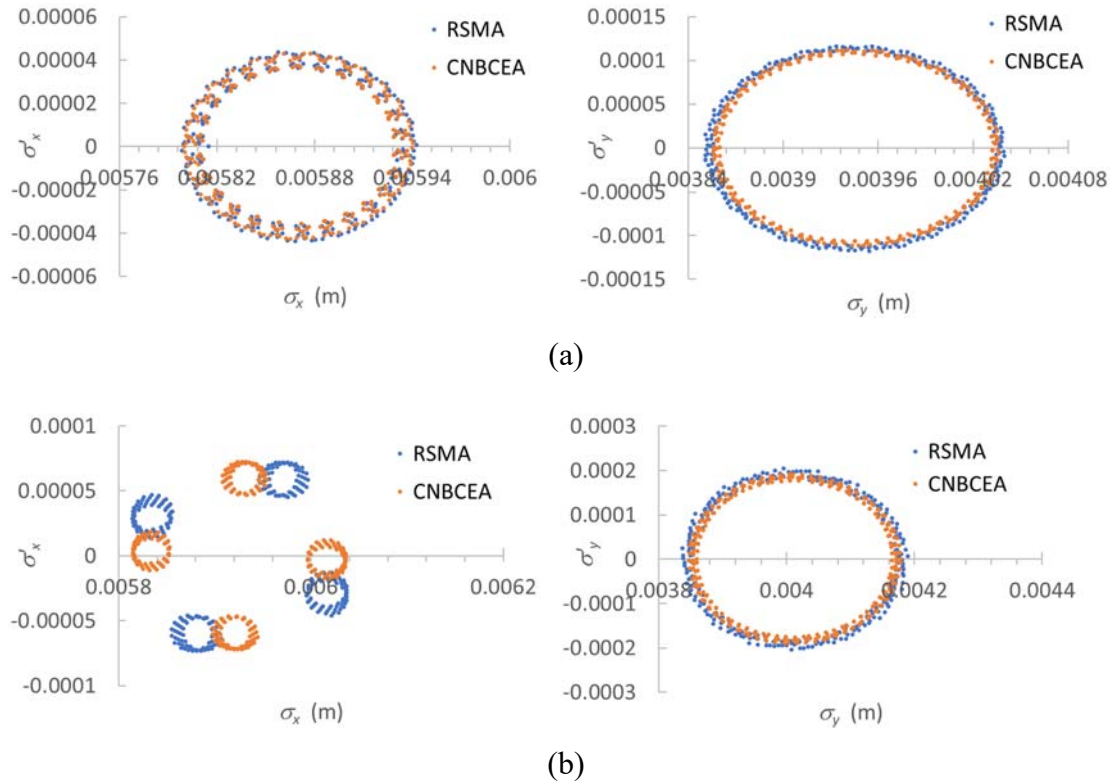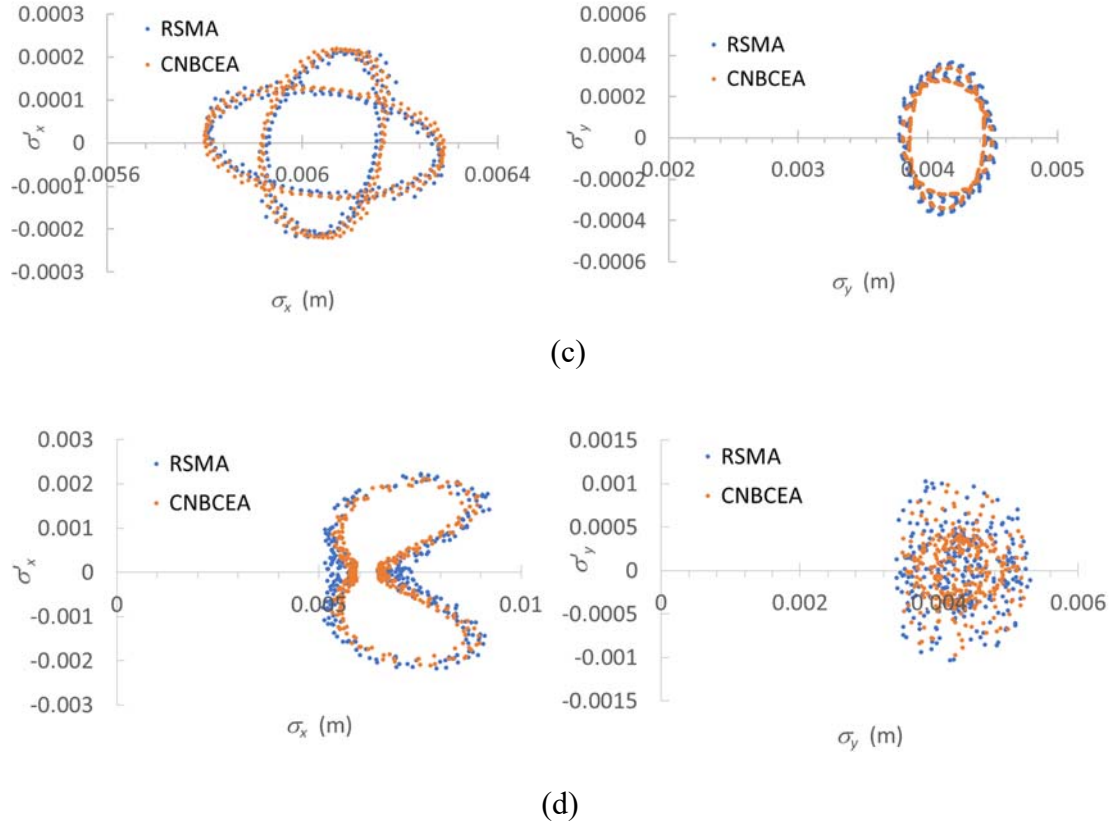
Figure 5.1: Poincaré map of the beam-core evolution evaluated by RSMA and CNBCEA for (a) I_B = 50 µA, (b) I_B = 100 µA, (c) I_B = 200 µA, and (d) I_B = 300 µA.

5.4. Instability observed in the beam-core phase-space ($\sigma, d\sigma/ds$).

As shown in Fig. 5.1, the beam-core size gradually increases with beam current, and the shape of the Poincaré map varies with beam current. The Poincaré maps at beam currents up to 200 µA still appear elliptical, whereas a phase transition appears to occur above 200 µA, resulting in a large change in beam-core size. It is interesting to focus our attention on the beam-core evolution and its behavior apparently depends on beam current. More Poincaré maps for different initial conditions are shown for beam currents over 240 µA in Fig. 5.2. The mapping colors in Fig. 5.2 correspond to the different initial conditions. Resonant structures in the phase space appear above a beam current of 250 µA, indicating the lowest-order nonlinear resonance. The resonant structures become deformed as the beam current increases and the chaotic area increases.

52

From the perspective of nonlinear dynamics [54], this phenomenon can be explained by period-doubling bifurcation. In Fig. 5.2 (b), the elliptic fixed points denoted in red shown in Fig. 5.2 (a) lose stability when $I_b \sim 250$ μA and produce two stable periods, resulting in new phase space structures in both directions. This period-doubling bifurcation is justified by the tangent map in Section 5. The structures persist above $I_b = 250$ μA and up to at least 400 μA (Figs. 5.2 (b), (c), and (d)). The present nonlinear system Eq. (5.8) is coupled to two freedoms of beam-core motion. Diffusion of the phase point in the beam-core phase space due to Arnold diffusion may be predicted; however, we have no reliable way to verify this.
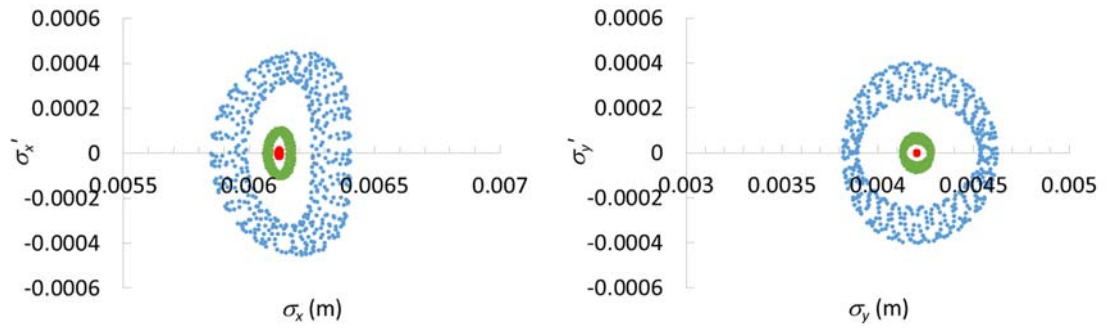
(a)
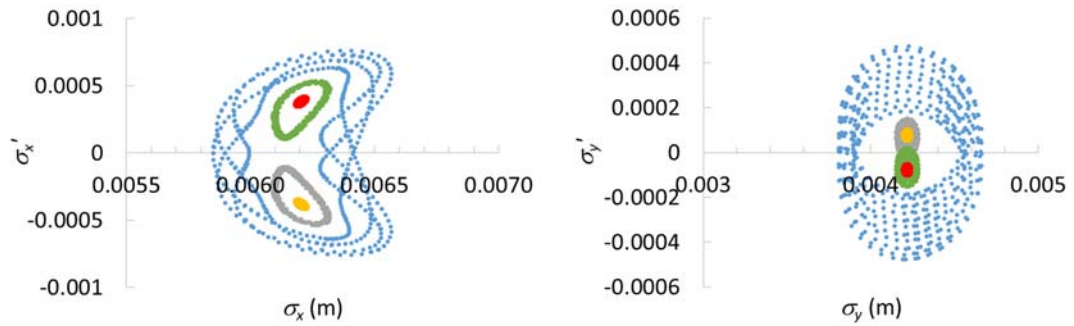
(b)
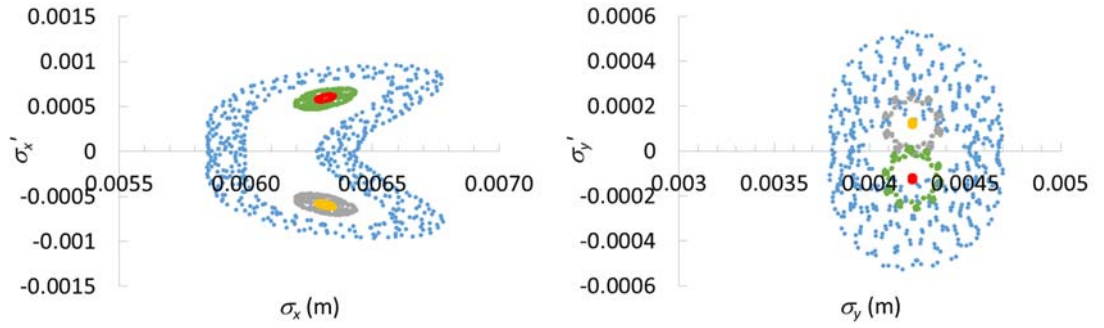
(c)
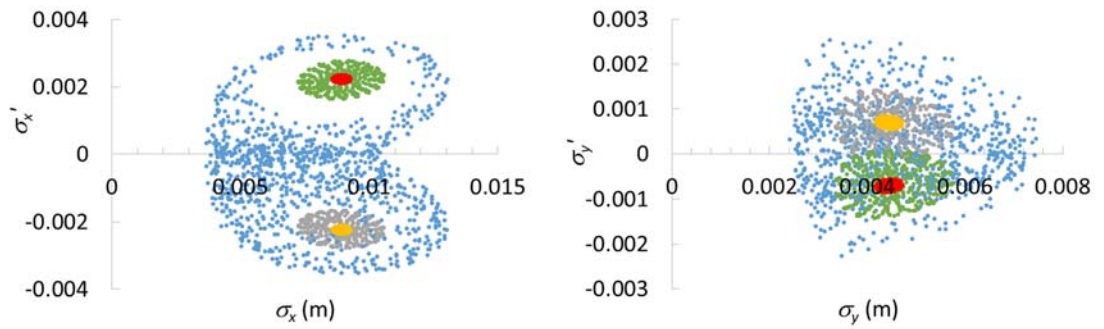
(d)

Figure 5.2: Poincaré map of the beam-core evolution (colors represents different initial condition) evaluated by the CNBCEA for (a) I_B = 240 μA, (b) I_B = 250 μA, (c) I_B = 255 μA, and (d) I_B = 400 μA. Plotting is done every 8 cells corresponding to 1 turn along the accelerator ring; in the other ward, this is even cell plotting. It is noted that Perio-doubling bifurcation becomes clear when including odd cell plotting.

To understand how the beam-core size evolves quantitatively, the maximum beam-core sizes of σ_x and σ_y under the initial conditions, which equals the nonperturbed matched beam-core (blue profile), are plotted as a function of beam current I_B. They change from several millimeters to several centimeters (Fig. 5.3). There is a critical point around 250 μA, suggesting that the nonlinear resonance is excited and the initial condition happens to be located in a chaotic region necklaced around the unstable fixed point.
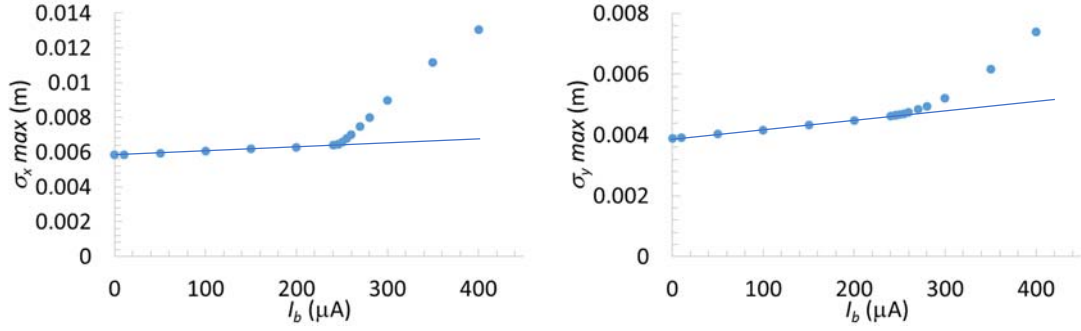
(a)
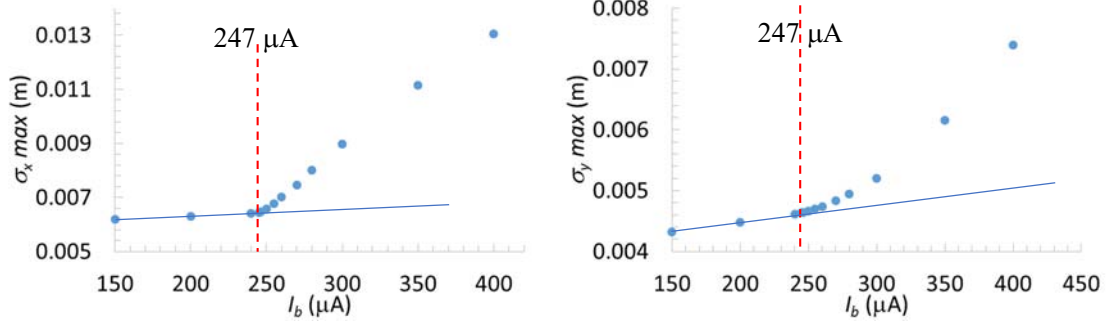
(b)

Figure 5.3: Maximum beam-core sizes during 300 turns versus the beam current. (a) Beam current range of 0 to 400 µA and (b) magnification of (a).

5.5. Stability analysis of the coupled linearized beam-core evolution equations

5.5.1. Coupled linearized beam-core evolution equation

Here, we solve the coupled nonlinear beam-core evolution equation analytically. First, let us look for periodic solutions $\sigma_x(s)$ and $\sigma_y(s)$ with a periodicity of the orbit circumference C that satisfy $\sigma_x^0(0) = \sigma_x^0(C)$, $\sigma'^0_x(0) = \sigma'^0_x(C) = 0$, and $\sigma_y^0(0) = \sigma_y^0(C)$, $\sigma'^0_y(0) = \sigma'^0_y(C) = 0$ using an approximation technique. Here,

we call σ_x^0 and σ_y^0 the matched beam-cores with the space-charge perturbation. Introducing small deviations u_x and u_y from the matched beam-core

$$\begin{cases} u_x = \sigma_x(s) - \sigma_x^0(s) \\ u_y = \sigma_y(s) - \sigma_y^0(s) \end{cases}, \tag{5.10}$$

substituting $\sigma_x(s)$ and $\sigma_y(s)$ into Eq. (5.8), and leaving the first-order terms with respect to u_x and u_y, we obtain coupled linearized beam-core evolution equations

$$\begin{cases} u_x'' + \left[K_x(s) + \dfrac{k}{(\sigma_x^0 + \sigma_y^0)^2} + \dfrac{3\varepsilon_x^2}{(\sigma_x^0)^4} \right] \cdot u_x + \dfrac{k}{(\sigma_x^0 + \sigma_y^0)^2} \cdot u_y = 0 \\ u_y'' + \dfrac{k}{(\sigma_x^0 + \sigma_y^0)^2} \cdot u_x + \left[K_y(s) + \dfrac{k}{(\sigma_x^0 + \sigma_y^0)^2} + \dfrac{3\varepsilon_y^2}{(\sigma_y^0)^4} \right] \cdot u_y = 0 \end{cases}. \tag{5.11}$$

Eq. (5.11) is the coupled linear equation with the restoring coefficients that are complicated periodic functions of s. We find that this periodicity has an important role when Eq. (5.11) is solved.

5.5.2. Matched beam core

The matched beam-core is solved with a linear approximation, assuming that the third term (space-charge term) on the left-hand side of Eq. (5.8) is smaller than the second and the right-hand term. We introduce small deviations $\delta_{x,y} (\equiv \sigma_{x,y}^0 - \sigma_{x,y}^M)$ from the nonperturbed $\sigma_{x,y}^M$, which is the matched solution of

$$\left(\sigma_{x,y}^M \right)'' + K_{x,y}(s) \sigma_{x,y}^M = \dfrac{\varepsilon_{x,y}^2}{\left(\sigma_{x,y}^M \right)^3}. \tag{5.12}$$

Substituting $\sigma_{x,y}^0$ into Eq. (5.8) and leaving the first-order terms, we obtain

$$\delta_{x,y}'' + \left[K_{x,y}(s) + \dfrac{3}{(\beta_{x,y})^2} \right] \cdot \delta_{x,y} = \dfrac{k}{\sigma_x^M + \sigma_y^M} \tag{5.13}$$

where $\beta_{x,y} = \dfrac{\left(\sigma_{x,y}^M \right)^2}{\varepsilon_{x,y}}$ is the beta function. Fortunately, second-order inhomogeneous

linear Eq. (5.13) has particular periodic solutions,

$$\delta_{x,y}(s) = \frac{k\sqrt{\beta_{x,y}(s)}}{4\sin\mu_{x,y}} \cdot \int_s^{s+C} \frac{\sqrt{\beta_{x,y}(s')}}{\sigma_x^M(s')+\sigma_y^M(s')} \cdot \cos[\mu_{x,y} - 2|\psi_{x,y}(s) - \psi_{x,y}(s')|]\, ds' \quad (5.14)$$

where $\psi_{x,y}(s) = \int_0^s \frac{ds'}{\beta_{x,y}(s')}$ are the betatron phases and $\mu_{x,y} = \int_0^C \frac{ds'}{\beta_{x,y}(s')}$ are the betatron phase advances. Details of the derivation are given in Appendix B. δ_x and δ_y along orbit s at a beam current of 200 μA are shown in Fig. 5.4. The matched beam-cores with the space charge perturbation $\delta_{x,y}(0)$ are compared with the numerically obtained matched beam-core in Fig. 5.5. The agreement is sufficient for the beam current of current concern.
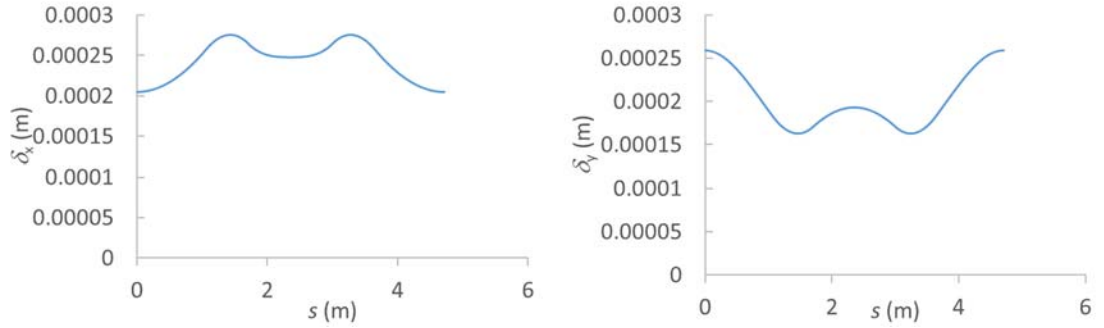
Figure 5.4: $\delta_{x,y}$ at a beam current of 200 μA in one sector of the KEK-DA lattice.
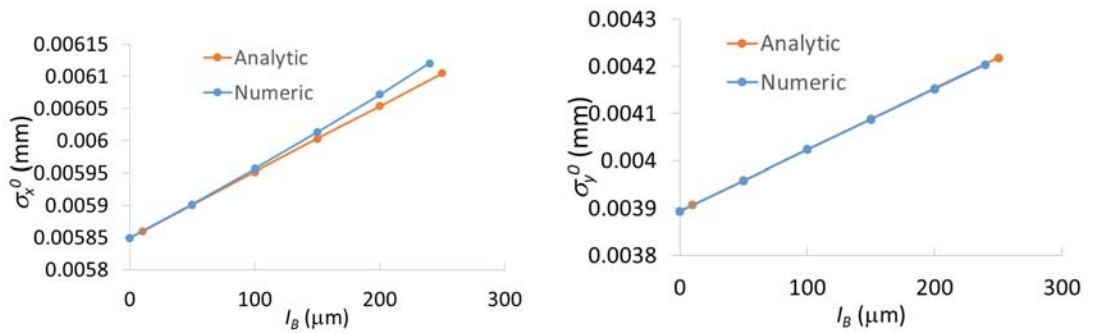
Figure 5.5: Matched beam-cores obtained from the linearized beam-core evolution equations and numerically obtained matched beam-cores vs. beam current.

5.5.3. Transfer matrix per turn and eigenvalue equation

It is important that all of the restoring coefficients in Eq. (5.11) are analytically determined in the previous subsection. If $\boldsymbol{U} = \left(u_x, u'_x, u_y, u'_y\right)^T$ is defined, the solution of Eq. (5.11) can be written as

$$\boldsymbol{U_{n+1}} = \mathbf{M} \cdot \boldsymbol{U_n} \tag{5.15}$$

where $\mathbf{M}$ is the 4×4 transfer matrix per turn. Thus, the stability problem of Eq. (5.11) is uniquely attributed to characteristics of transfer matrix $\mathbf{M}$. Matrix elements of transfer matrix $\mathbf{M}$ are easily obtained by solving Eq. (5.11) up to one turn for four initial conditions by the numerical method. The four initial conditions are unit vectors, which are defined as $\boldsymbol{U^{(1)}} = \left(u_x^{(1)}, u_x^{(1)}, u_y^{(1)}, u_y^{(1)}\right)^T = (1,0,0,0)^T$, $\boldsymbol{U^{(2)}} = \left(u_x^{(2)}, u_x^{(2)}, u_y^{(2)}, u_y^{(2)}\right)^T = (0,1,0,0)^T$, $\boldsymbol{U^{(3)}} = \left(u_x^{(3)}, u_x^{(3)}, u_y^{(3)}, u_y^{(3)}\right)^T = (0,0,1,0)^T$, and $\boldsymbol{U^{(4)}} = \left(u_x^{(4)}, u_x^{(4)}, u_y^{(4)}, u_y^{(4)}\right)^T = (0,0,0,1)^T$. From the output vector after one turn for each set of initial conditions, transfer matrix $\mathbf{M}$ is written as

$$\mathbf{M} = \begin{pmatrix} u_x^{(1)}(C) & u_x^{(2)}(C) & u_x^{(3)}(C) & u_x^{(4)}(C) \\ u_x'^{(1)}(C) & u_x'^{(2)}(C) & u_x'^{(3)}(C) & u_x'^{(4)}(C) \\ u_y^{(1)}(C) & u_y^{(2)}(C) & u_y^{(3)}(C) & u_y^{(4)}(C) \\ u_y'^{(1)}(C) & u_y'^{(2)}(C) & u_y'^{(3)}(C) & u_y'^{(3)}(C) \end{pmatrix} \tag{5.16}$$

The stability problem is attributed to the eigenvalue problem in Eq. (5.16). Eigenvalues λ_i are solutions of the eigenvalue equation,

$$|\mathbf{M} - \lambda\mathbf{I}| = (\lambda - \lambda_1) \cdot (\lambda - \lambda_2) \cdot (\lambda - \lambda_3) \cdot (\lambda - \lambda_4) = 0 \tag{5.17}$$

where $\mathbf{I}$ is the unit matrix. Because eigenvector ξ_i corresponds to eigenvalue λ_i with the characteristics $\mathbf{M}\xi_i = \lambda_i\xi_i$, turn by turn evolution of the arbitrary beam-core vector, $\boldsymbol{u} = \sum_{i=1}^{4} c_i \cdot \xi_i$, is written as $\boldsymbol{M} \cdot \boldsymbol{u} = \sum_{i=1}^{4} c_i \cdot \boldsymbol{M} \cdot \xi_i = \sum_{i=1}^{4} c_i \cdot \lambda_i \cdot \xi_i$. Its evolution after the N-th turn is

$$\boldsymbol{M}^N \cdot \boldsymbol{u} = \sum_{i=1}^{4} c_i \cdot (\lambda_i)^N \cdot \xi_i \qquad (5.18)$$

Eq. (5.18) implies that the stability condition is $|\lambda_i| = 1$.

This transfer matrix $\mathbf{M}$ is in fact the tangent map around the stable periodic solutions $(\sigma_x^0, 0)$ and $(\sigma_y^0, 0)$ for the periodic nonlinear coupling system Eq. (5.8).

5.5.4. Stability diagram

Eq. (5.17) can be expressed as

$$\lambda^4 - C_3 \cdot \lambda^3 + C_2 \cdot \lambda^2 - C_1 \cdot \lambda + C_0 = 0 \qquad (5.19)$$

where

$$det\, \mathbf{M} \equiv C_0 = \lambda_1 \cdot \lambda_2 \cdot \lambda_3 \cdot \lambda_4 = 1 \qquad (5.20)$$

$$C_1 = \lambda_1 \cdot \lambda_2 \cdot (\lambda_3 + \lambda_4) + (\lambda_1 + \lambda_2) \cdot \lambda_3 \cdot \lambda_4 \qquad (5.21)$$

$$C_2 = \lambda_1 \cdot \lambda_2 + (\lambda_1 + \lambda_2) \cdot (\lambda_3 + \lambda_4) + \lambda_3 \cdot \lambda_4 \qquad (5.22)$$

$$\mathrm{Tr}\mathbf{M} \equiv C_3 = \lambda_1 + \lambda_2 + \lambda_3 + \lambda_4 \qquad (5.23)$$

C_i (i = 1–4) are functions of the matrix elements of $\mathbf{M}$. If the eigenvalues are two set complex conjugates $r_a \exp(\pm i\phi_a)$ and $r_b \cdot \exp(\pm i\phi_b)$, $r_a = r_b = 1$ must be satisfied for stability from Eq. (5.20). In this case, Eqs. (5.22) and (5.23) are written as

$$x + y = C_3 \qquad (5.24)$$

$$x \cdot y = C_2 - 2 \qquad (5.25)$$

where $x = 2\cos\phi_a$ and $y = 2\cos\phi_b$. Let us consider the quadratic equation and quadratic function with respect to z,

$$z^2 - C_3 \cdot z + C_2 - 2 = 0 \qquad (5.26)$$

$$f(z) = z^2 - C_3 \cdot z + C_2 - 2 = \left(z - \frac{C_3}{2}\right)^2 + C_2 - 2 - \left(\frac{C_3}{2}\right)^2 \qquad (5.27)$$

Here, x and y are solutions of Eq. (5.26). For $|x| \leq 2$ and $|y| \leq 2$, function $f(z)$ has to

satisfy relations

$$f(-2) = 2 + 2 \cdot C_3 + C_2 \geq 0 \tag{5.28}$$

$$f(+2) = 2 - 2 \cdot C_3 + C_2 \geq 0 \tag{5.29}$$

$$f\left(\frac{C_3}{2}\right) = C_2 - 2 - \left(\frac{C_3}{2}\right)^2 \leq 0. \tag{5.30}$$

When $C_3 \geq 0$, relations (5.28), (5.29), and (5.30) are consolidated into

$$2 \cdot C_3 - 2 \leq C_2 \leq \left(\frac{C_3}{2}\right)^2 + 2. \tag{5.31}$$

In contrast, when $C_3 < 0$,

$$-2 \cdot C_3 - 2 \leq C_2 \leq \left(\frac{C_3}{2}\right)^2 + 2. \tag{5.32}$$

Fig. 5.6 shows a schematic stability diagram for coefficients C_2 and C_3 as a function of I_B.
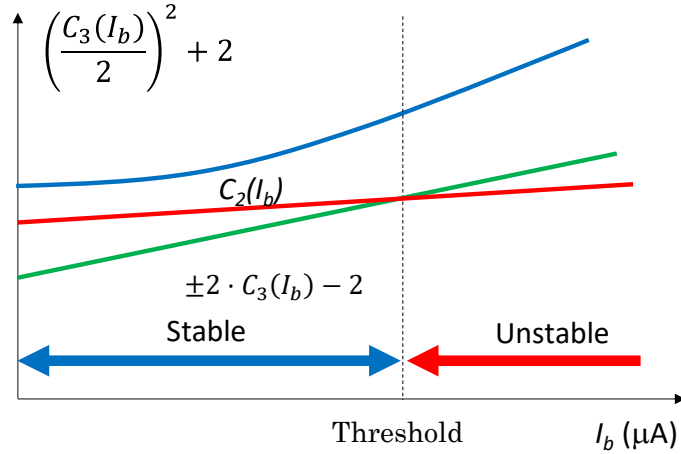
Figure 5.6: Stability diagram for C_2 and C_3.

When the eigenvalues are two real values and one set complex conjugate $(r\, exp(\pm i\phi))$, the stable condition implies that Eqs. (5.27) and (5.28) can be written as $\pm 2 \cdot C_3 - C_2$

$$C_3 = \pm 2 + 2\cos\phi \tag{5.33}$$

60

$$C_2 = 2 \pm 4\cos\phi. \tag{5.34}$$

When $\lambda_1 = \lambda_2 = -1$, coefficients C_2 and C_3 must satisfy $C_2 = -2(C_3 + 1)$, whereas when $\lambda_1 = \lambda_2 = 1$, $C_2 = 2(C_3 - 1)$.

5.5.5. Stability threshold for the example

Matrix elements of transfer matrix $\mathbf{M}$ for the current example are easily obtained as functions of the beam current. Eq. (5.32) is the stability condition because C_3 is negative. In the other form, the stability condition becomes

$$\begin{cases} C_2 + 2 \cdot C_3 + 2 \geq 0 \\ \left(\frac{C_3}{2}\right)^2 + 2 - C_2 \geq 0 \end{cases}. \tag{5.35}$$

The stability diagram for the proton beam in the KEK-DA lattice is shown in Fig. 5.7. The coefficient of $C_2 + 2 \cdot C_3 + 2$ is less than zero at 253 µA. In the range of 390–570 µA, stability condition (5.35) is also not satisfied. The eigenvalue of the matrix in Appendix C shows that the instability occurs above a beam current of 252 µA. Thus, we conclude that the stability threshold is at 252 µA. This value is close to the numerically obtained threshold of 247 µA. The stability threshold is confirmed by analyzing the stability condition of the eigenvalue.
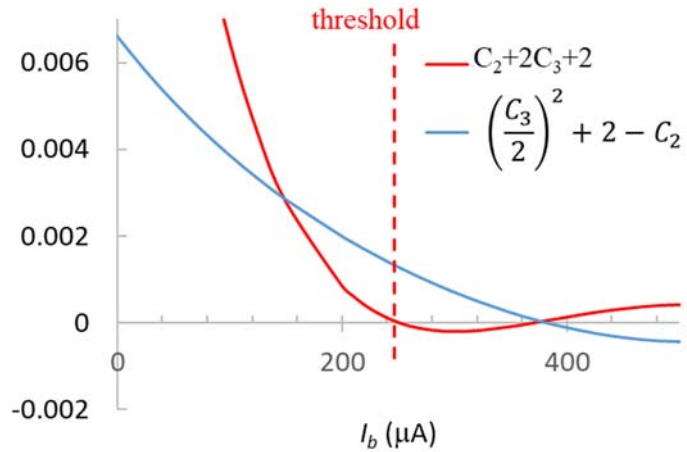
Figure 5.7: Stability diagram and the beam current threshold of the proton beam in the

As predicted, the stability threshold for the linearized system of the tangent map corresponds to the disappearance of stability in the matched solution, $(\sigma_x^0, 0)$ and $(\sigma_y^0, 0)$, suggesting the *onset* of the lowest-order nonlinear resonance of the original coupled nonlinear beam-core evolution system.

5.6. Scaling law

As mentioned earlier, the KEK-DA is capable of accelerating any species of ion with its possible charge state, including giant cluster ions, such as C-60 or Si-100, where mass number A and charge-state Q vary over a wide range. The acceptable beam current determined by space charge effects should depend on A and Q. Fortunately, the beam current can be predicted from the proton threshold current that has been discussed here. As shown in Eq. (5.8), the space-charge effect contribution appears in the third term of the equation, which is proportional to parameter k. From the definition of k and I_0, the beam current is written as

$$I_B = \frac{4\pi\varepsilon_0 mc^3 \beta^3 \gamma^3 k}{2e} \cdot \frac{A}{Q}. \tag{5.36}$$

When the term $\frac{4\pi\varepsilon_0 mc^3 k}{2e}$ is constant, then I_B is proportional to $\beta^3\gamma^3 \frac{A}{Q}$. Assuming the same injection energy and same actual emittance in the ring, the beam current threshold can be obtained from the threshold of the reference ion beam from scaling equation

$$I_{B2}^{thres} = \frac{A_2}{Q_2} \cdot \frac{Q_1}{A_1} \cdot \frac{\beta_2^3 \gamma_2^3}{\beta_1^3 \gamma_1^3} I_{B1}^{thres} \tag{5.37}$$

When the reference is a proton beam, its threshold current is 247 μA in the KEK-DA with an injection voltage of 0.2 MV. From Eq. (37), the threshold beam current for C_{60}^{+10} (A = 720) is estimated to be 29.5 μA.

Scaling for the emittance is quite clear from Eq. (5.6) in a case where there is no

excessive emittance unbalance between the horizontal and vertical directions; it should read $I_{B2}^{thres} = \frac{\varepsilon_2}{\varepsilon_1} \cdot I_{B1}^{thres}$.

5.7.   Space charge effects in the RAFFIA

Space charge effects of C_{60}^{+10} acceleration in the RAFFIA are evaluated in order to know the beam current threshold. The CNBCEA which has been justified above is used for space charge evaluation by assuming the beam emittance 1×10^{-5} m·rad. The Poincare maps for the beam core evolution over 300 turns are shown in Fig. 5.8. Up to a certain limit of the beam current, the beam core size slightly changes with the stable pattern. Beyond some beam current, the beam core evolution becomes chaotic. The maximum beam core sizes as a function of beam current are shown in Fig. 5.9, where the beam sizes drastically change beyond 225 μA. This is the space charge limit.

(a)

(b)

(c)
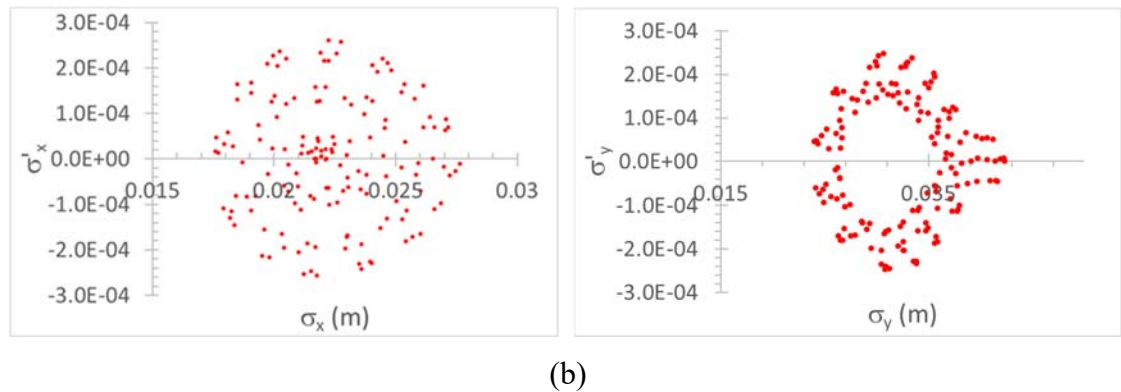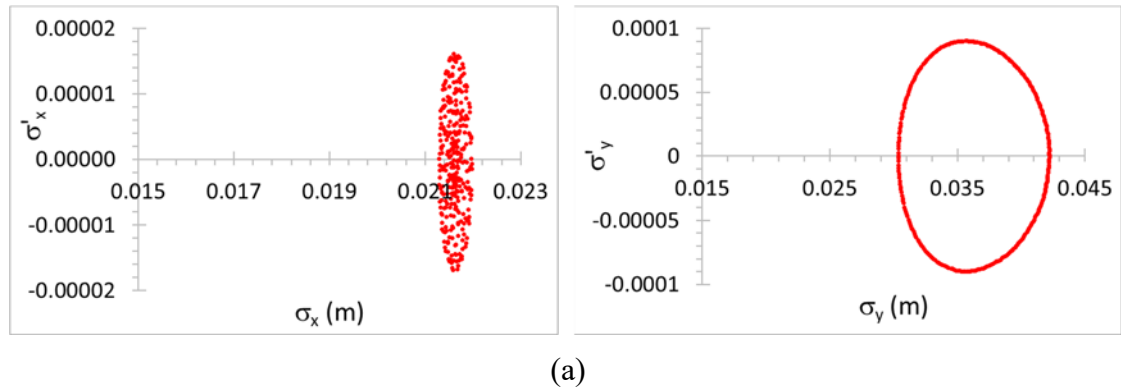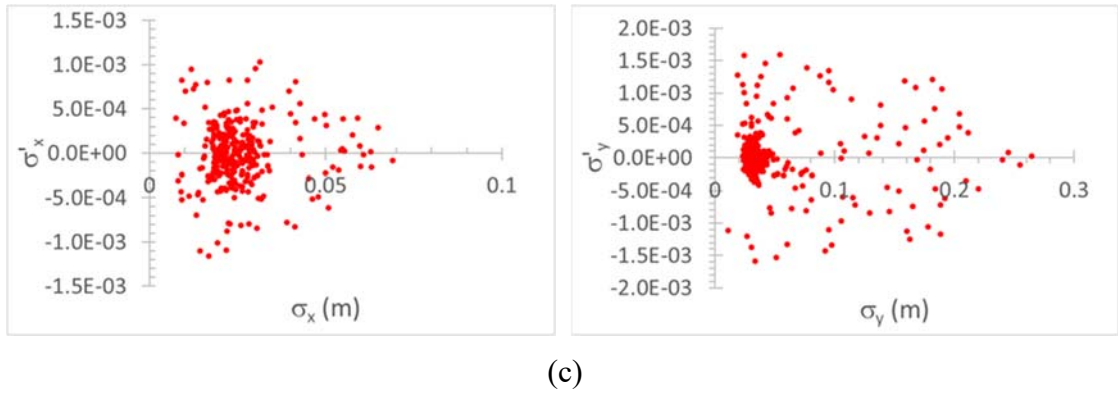
Figure 5.8: The Poincare map of the beam core evolution observed at the injection

point for (a) I_B = 50 µA, (b) I_B = 200 µA, and (c) I_B = 250 µA.
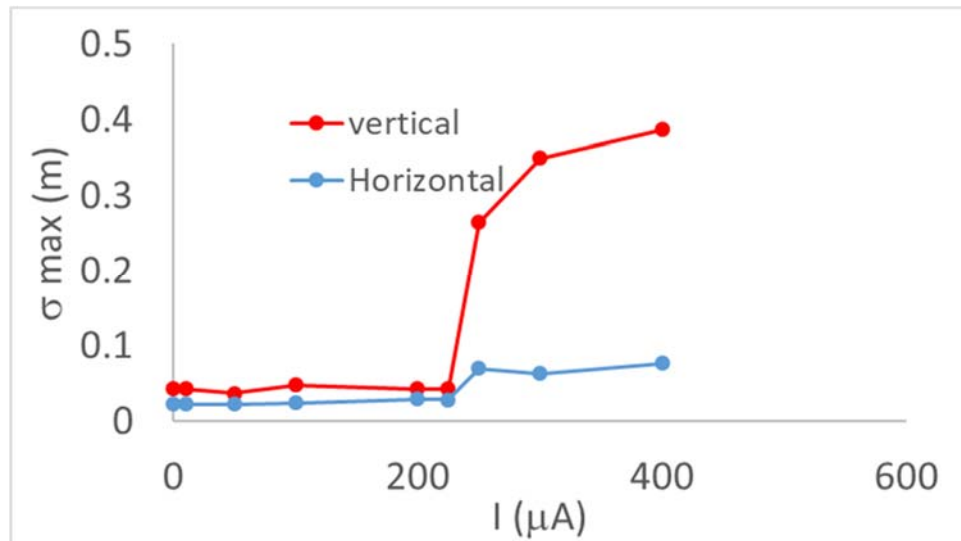
Figure 5.9: Maximum beam sizes vs. beam current.

Chapter 6 Beam guiding magnets for the RAFFIA

6.1. Bending magnet

The designed bending magnet and magnetic field distribution on the median plane are shown in Fig. 6.1. The important features of this bending magnet is two different magnetic field polarity that is generated in the front gap and the main bending regions by using single set of coils. The magnet field calculations indicate a peak flux density of 0.98 T in the front gap and -1.5 T in the main bending region. The magnet is 5.8 m long, 0.7 m high, and 2.8 m wide so as to cover the particle orbit up to the extraction energy. The weight of the magnet reaches 62.258 ton.
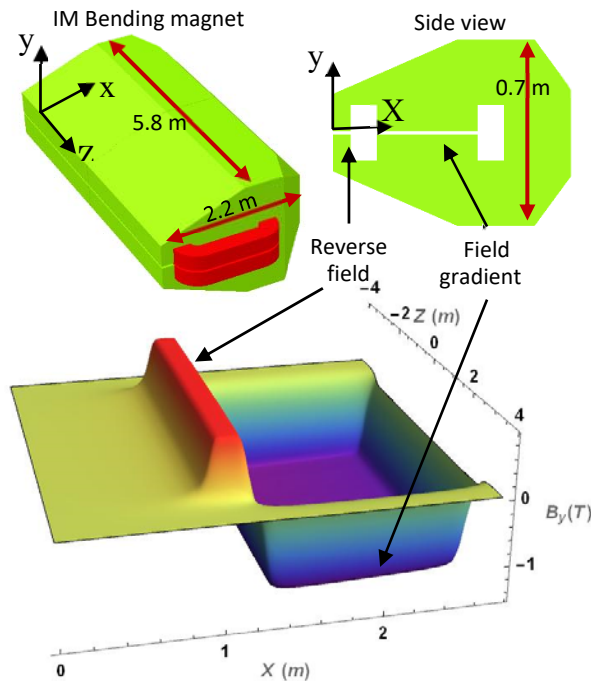
Figure 6.1: Bending magnet and its magnetic field component B_y on the median plane.

For beam stability, beam focusing in the bending magnet is provided by edge focusing at the edge of two poles and gradient field in the main magnet region. The gradient field in the main magnet can be seen in the Fig. 6.2 (a). As described in the

previous chapter, the beam stability of the RAFFIA is also related to the inherent COD. The source of COD in the bending magnet is reduced by minimizing the non-uniformity of the magnetic field in Z direction. The minimizing is performed by varying pole gap as a function of Z coordinate. As shown in Fig. 6.2 (b), the non-uniformity at the reverse field and gradient field are obtained with 175 and 250 gauss peak to peak, respectively.
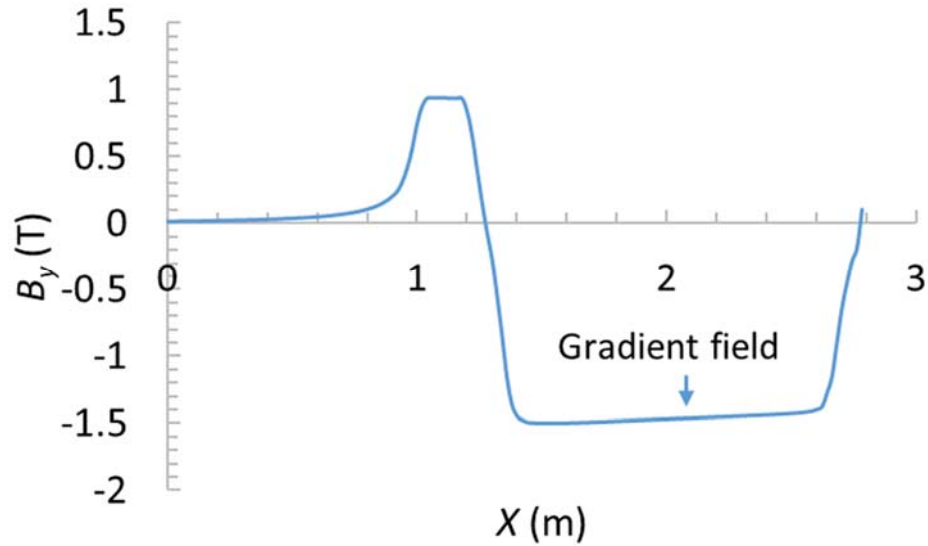
(a)
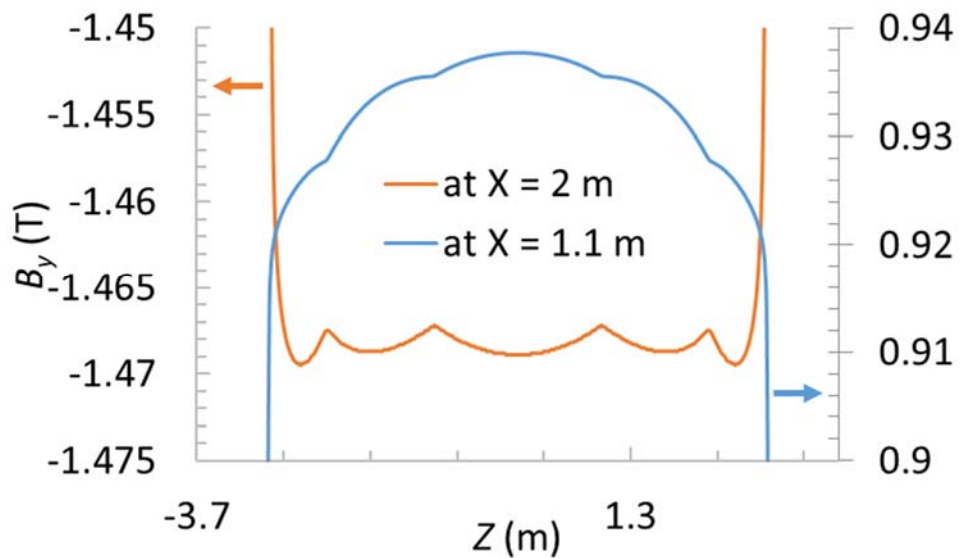
(b)

Figure 6.2: Line distribution of the magnetic field at center of longitudinal magnet (*Z*

= 0 m) (a), and near the center of the reverse field region ($X = 1.1$ m) and near the center of the main field region ($X = 2$ m) (b).

6.2. Quadrupole magnet

The quadrupole doublets of the RAFFIA have been known to be operated in the ramping pattern. The maximum of the gradient field of the quadrupole focusing and defocusing are obtained at 4.132 T/m and 4.461 T/m, respectively. These parameters are required in the designing of the quadrupole magnet. Since the quadrupole generates hyperbolic-shape flux in the *x-y* axis as shown in Fig. 6.3, the pole shape of the quadrupole is designed to follow the hyperbolic shape. Rogowski shape at the edge of the pole is applied to reduce local saturation which will generate eddy loss when operated in the ramping pattern.
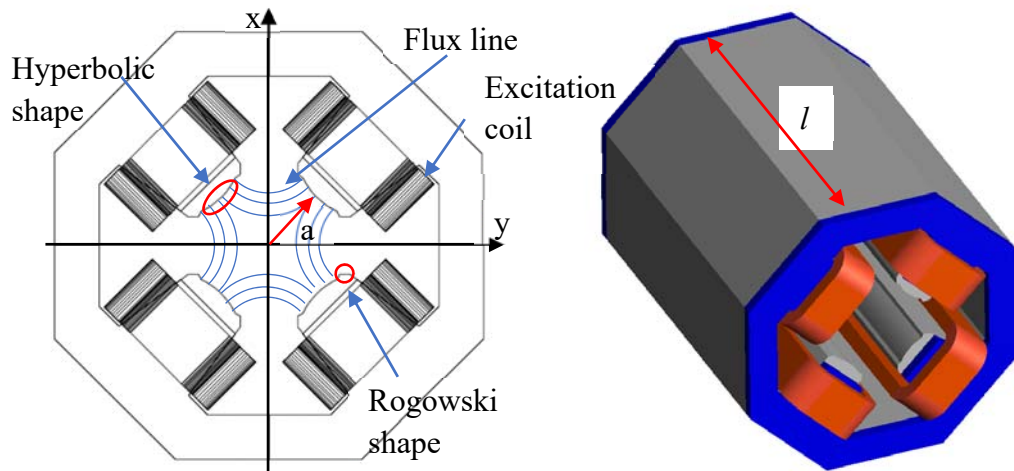
Figure 6.3: Quadrupole schematic and its cross section.

The excitation current (*I*) of the quadrupole magnet is define by the following equation

$$NI = \frac{ga^2}{2\mu_0},$$ (6.1)

where N is the turn number per coil, g is the field gradient (T/m), a is the bore radius

(m), and μ_0 is the permeability of free space. The inductance of the coils (L_Q) is calculated by using the following equation [55]

$$L_Q = 8\mu_0 N^2 y_{max}(y_{max} + 2w_c/3)\frac{l}{a^2}, \tag{6.2}$$

where y_{max} is the distance from the magnet center to the coil face (m), w_c is the coil width (m), and l is the magnetic length (m). The design parameters of the quadrupole doublet are summarized in the following Table.

Table 6.1: Quadrupole doublet parameters.

Parameter	QF	QD
Maximum field	4.132 T/m	4.461 T/m
Magnetic length (l)	0.5 m	0.5 m
Maximum aperture	r < 0.07 m	r < 0.07 m
Gap height (r_{bore})	0.088 m	0.088 m
Max Current	354 A	382 A
Hollow conductor	7x7 mm^2 (hole 4x4 mm^2)	7x7 mm^2 (hole 4x4 mm^2)
Coil Turn	36 turns/pole	36 turns/pole
Inductance (L_Q)	14.0 mH	14.0 mH
Resistance	108 mΩ	108 mΩ

6.3. Steering magnet

Steering magnet is a dipole magnet which may be generated in a window frame or H-frame type. The excitation coil parameters are simply defined by

$$NI = \frac{Bh}{\mu_0}, \tag{6.3}$$

where B is the magnetic field (T) and h is the half gap size (m). The steering magnet of the RAFFIA ramps to a maximum field of 0.01141 Tm. By this parameter, the excitation coil parameters can be determined by Eq. (6.3), and the inductance of the coil is determined by [55],

$$L_B = \mu_0 \frac{2N^2(w_a + 2w_c/3)l}{h},$$

(6.4)

where w_a is aperture between coil. The design parameters of the steering magnet are summarized in the following Table.

Table 6.2: Steering magnet parameters.

Parameter	Steering magnet
Maximum field	0.01141 Tm
Magnetic length (l)	0.3 m
Maximum aperture	$\|x\| < 0.03$ m, $\|y\| < 0.06$ m
Gap height ($2h$)	0.12 m
Max Current	429 A (bipolar)
Hollow conductor	7x7 mm^2 (hole 4x4 mm^2)
Coil Turn	11 turns/pole
Inductance (L_B)	0.20 mH
Resistance	11.6 mΩ

Chapter 7 Prototype bending magnet for the RAFFIA (1/8th size model)

7.1. Design of the prototype bending magnet

A small-scale prototype of the RAFFIA bending magnet with the reverse field strip is designed by using Tosca Opera 3D. This is a 1/8th size model of the designed 144 MeV induction synchrotron 90° bending magnet. The main bending field is excited across the inner pole gap and the reverse field is excited across the outer pole gap. The shape and the size of the prototype magnet is shown in Fig. 7.1.
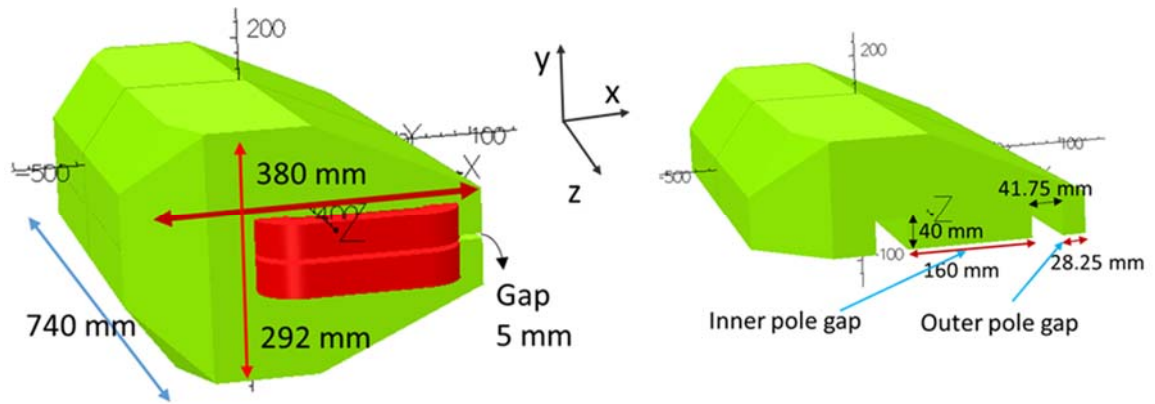
Figure 7.1: Schematics of the prototype magnet shape and size.

The uniformity of the magnetic field along the Z direction is important in the RAFFIA bending magnet, as discussed in Chapter 4. The magnet pole surface along the Z direction is optimized within a limited physical size, using the four-point spline technique to achieve uniformity. The curvature of the line is determined by the distance of each point (Fig. 7.2). From the Tosca calculation, the optimized curve is obtained by setting the distance of each spline point at the fixed coil current of 116 A (Table 7.1).

Table 7.1. Optimized spline curve.

Spline parameters	Main field	Reverse field
a (mm)	370	370

b (mm)	0.067	0.154
c (mm)	0.062	0.092
d (mm)	337	335
e (mm)	0.066	0.154
f (mm)	175	175
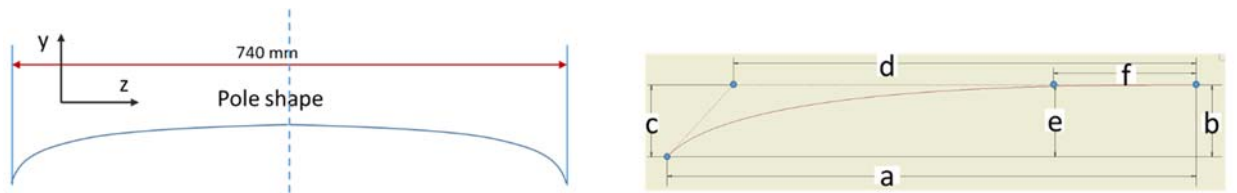
Figure 7.2: Curved pole shape determined by using the four points spline technique.

It is difficult to reduce the non-uniformity, ΔB_y, further using the four-point spline technique. Although it may be possible to use a multi-point spline containing many more points, the size of the reduction will be limited. In addition, highly accurate pole shaping, which is required for the multi-point spline technique, exceeds the capability of the available numerical control (NC) machine. ΔB_y is sufficiently small compared with ΔB_y (>100 G) used in the orbit calculation, as discussed in Section 6.1.

The magnetic flux density profile, in which the peak-to-peak magnetic flux density in the y direction (ΔB_y) is 6 G in the main field region and 8 G in the reverse field region, is achieved (Fig. 7.3). ΔB_y for the optimized pole shape is much lower than that for the flat pole shape.
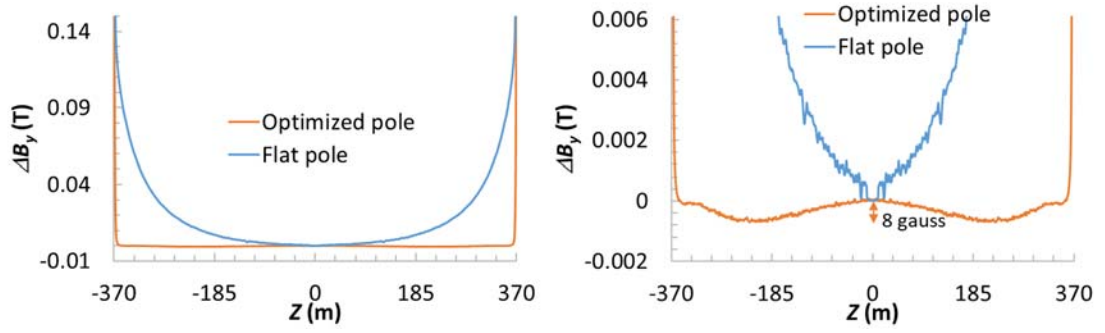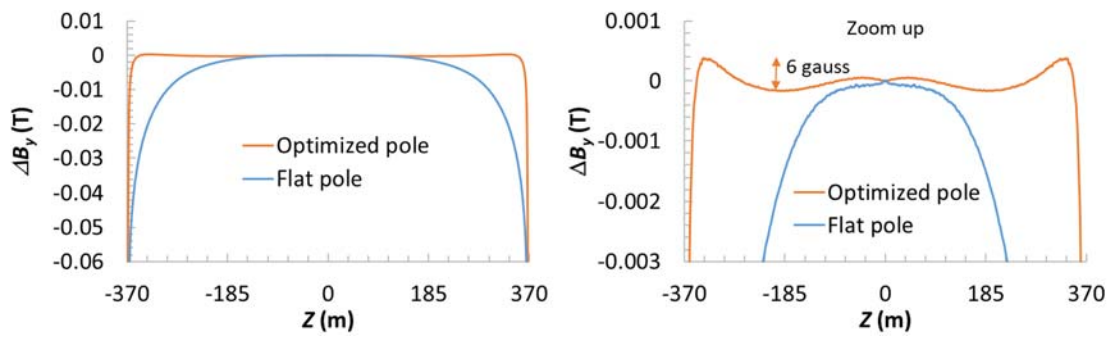
Figure 7.3: Relative profiles of magnetic fields along the *Z* direction in (a) the outer pole and (b) the inner pole.

7.2. Manufacturing the magnet poles and excitation coil

This prototype magnet was manufactured at KEK. The upper/lower iron cores were machined from low-carbon steel and the pole shape was finely processed by the KEK machine shop NC machine. The cores have seven bolt holes for bolt tightening (Fig. 7.4), and the two poles were carefully fitted together with seven screw bolts installed using a torque tool.

Figure 7.4: Lower part of the iron core (left) and assembled iron core (right).

Two racetrack-shape coils (Fig 7.5 (b)) were manufactured by a private company following our design. Each coil consists of 56 turns, comprising a solid square coil with four columns and 14 layers, and the plate with cooling pipes is placed in the middle of the coils (Fig. 7.5 (a). The specifications of the excitation coils are listed in Table 7.2. Two coils were mounted on the individual poles before they were combined.

Table 7.2: Specifications of the coils.

Parameters	Unit
Designed operation current	116 A
Ampere turns	6494 A·Turns/coil
Coil resistant	0.197 Ω
Operating voltage	27 V
Water cooling flow rate	3.6 L/min
Weight	25 kg/coil
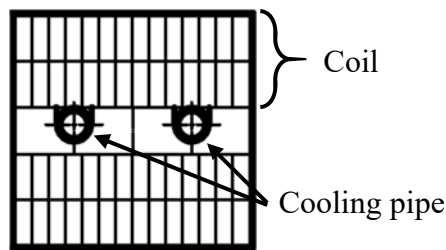
(a)

(b)

Figure 5: (a) Cross-sectional configuration and (b) photograph of the coils.

7.3. Gap size measurement.

The KEK machine shop, where the pole surfaces were processed with the NC machine, measured the distance from the center of the gap, namely the median plane, to the pole surface separately for the upper and lower poles before the magnet was assembled. The gap size was determined by summing both measured values. Other gap measurements were obtained with a micrometer and a 3D gage (Gage-PLUS, FARO) tool after magnet assembly. The measurements were performed only for the outer pole gap; it was impossible to measure the inner pole gap size because the gap was too narrow. In the micrometer and FARO gage measurements, the measurement position along the *Z* direction was determined manually; thus, the accuracy was lower than that of the KEK machine workshop measurement. The gap size measurement results are shown in Fig. 7.6.
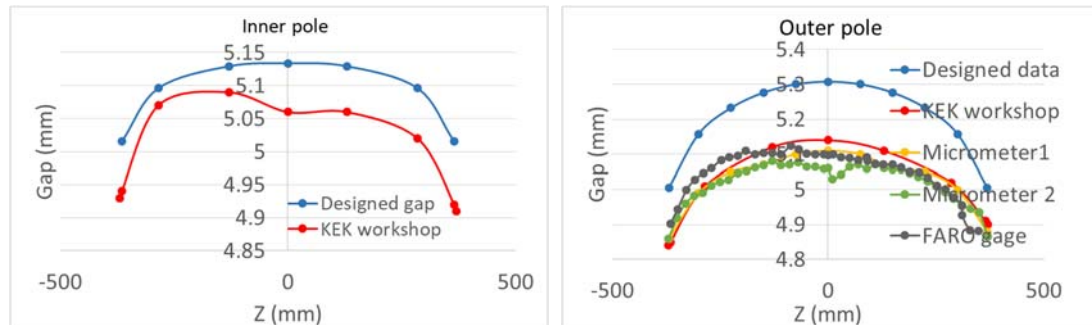
Figure 7.6: Gap size measurement results.

The measured inner pole gap was apparently asymmetric along the *Z* direction and the gap size was smaller than the designed gap size. Although the gap size obtained by the KEK machine shop was slightly different from the micrometer and 3D gage measurements, the three gap size measurements were still consistent, suggesting that the inner gap size measured at the KEK machine shop was reliable.

7.4. Gap size reduction associated with excitation

Deformation of the outer pole gap was observed when the excitation current was turned on. The gap deformation was caused by the magnetic attraction force between the two magnet poles. Fig. 7.7 shows the gap size reduction as a function of the excitation current. The gap size reduction depends on the clamping force between the upper and bottom cores. However, the clamping force was not the main source of the gap size reduction.
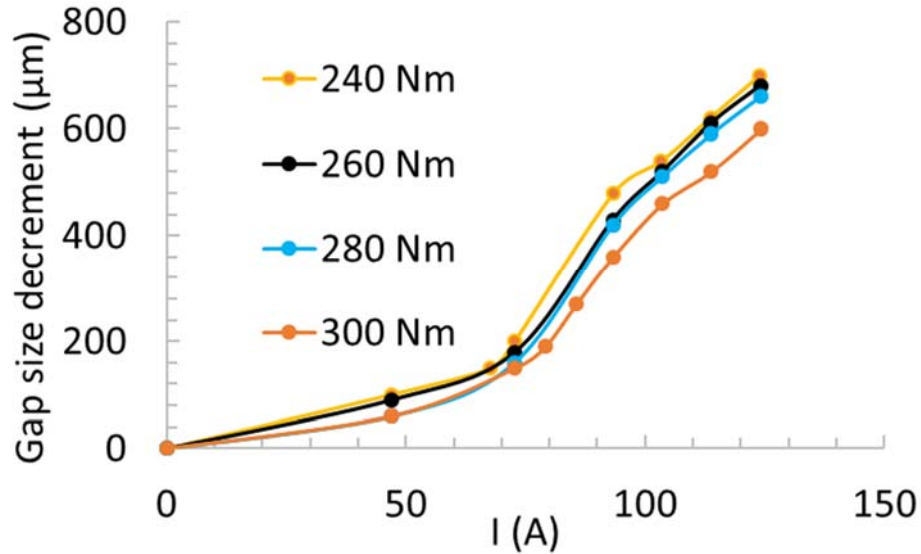
Figure 7.7: Gap size reduction as a function of excitation current for different clamping forces.

The magnetic field attraction force (F) is written as

$$F = \frac{AB^2}{2\mu_0} \tag{7.1}$$

where A is the pole surface area, B is the magnetic flux density, and μ_o is the permeability in a vacuum. By substituting the measured magnetic flux density into Eq. (7.1), F is obtained. The observed gap deformation with a clamping torque of 240 N·m is shown as a function of F in Fig. 7.8, and we can conclude that the gap deformation is simply caused by the magnetic attraction force.
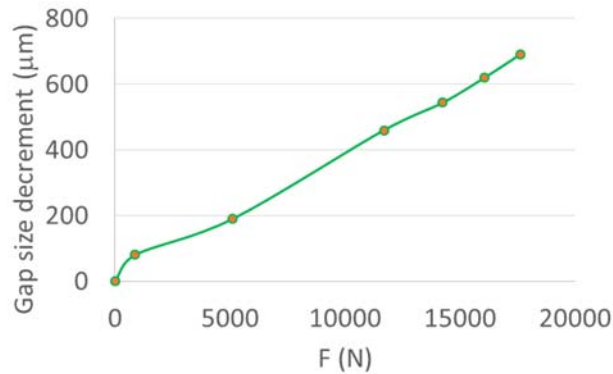
Figure 7.8: Experimental gap deformation as a function of the magnetic attraction force.

To minimize gap deformation during magnetization, non-magnetic spacers were inserted into the outer pole gap in the magnet edge. This simple counter measure reduced the gap deformation greatly; the outer pole gap size at the coil current of 123 A was reduced from 600 to 11 μm.

7.5. Magnet field measurement

The magnetic field measurement was conducted on the median plane of the gap under a controlled environment temperature of 24 °C. The set-up of the magnetic field measurement using a two-dimensional mapping tool is shown in Fig. 7.9. The mapping tool was carefully aligned to the prototype magnet before measurement. The gaussmeter was calibrated with the 1000 G standard magnetic field. The magnetic field data was collected from the output voltage of the gaussmeter because the galvanometer of the gaussmeter has a large minimum scale. The output voltage was calibrated with the galvanometer. The relationship between the output voltage and the galvanometer was linear (Fig. 7.10).
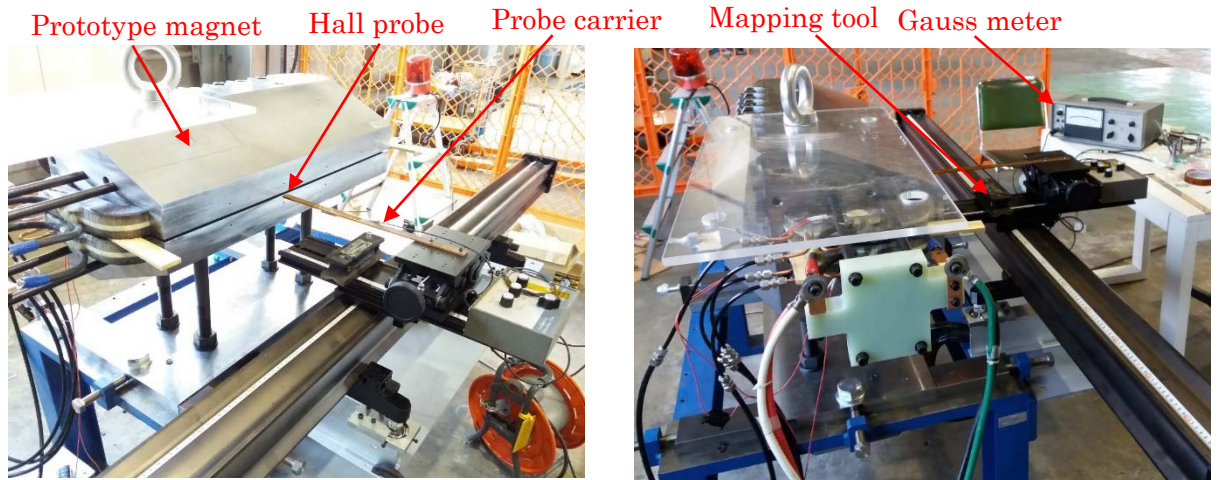
Figure 7.9: Layout of the field measurement stands.
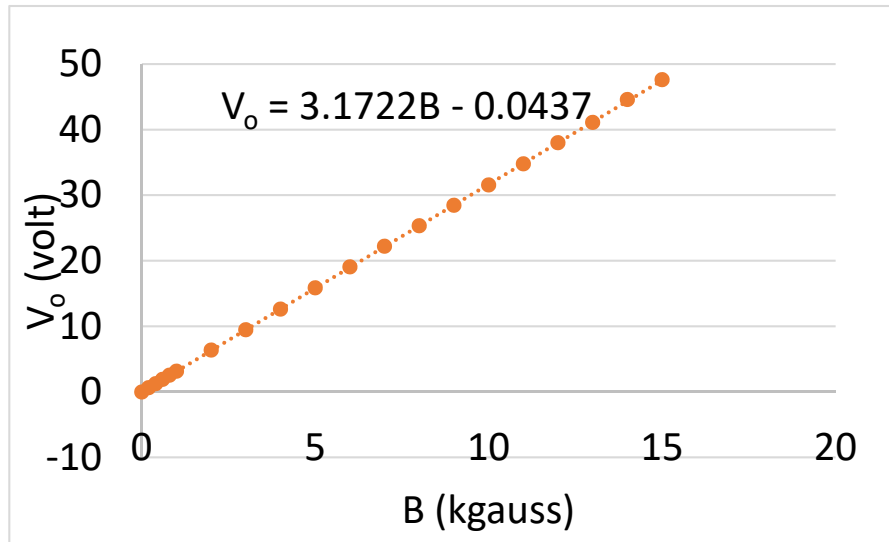
Figure 7.10: Hall probe calibration data.

7.6. Excitation curve of the magnetic field

Excitation of the prototype magnet was observed at the central point on the median plane of the inner and outer pole gaps. The magnetic field excitation curve is shown together with the calculation result in Fig. 7.11. The excitation curve of the main magnetic field was different from that of a usual bending magnet; the magnetic field increased almost uniformly with the excitation current below 50 A and the gradient

changed beyond that, but did not achieve saturation. In addition, a unique excitation curve in the outer pole gap was observed, where the magnetic field was almost zero up to a current of several amperes, and then uniformly increased to saturation with increasing excitation current. The magnetic flux results in Fig. 7.12 can be explained as follows.

(1) Most of the magnetic flux in the inner pole gap passes through the closed-return yoke at the low current.

(2) When the excitation current is high enough to create similar magnetic resistance in the loop containing the inner pole gap and closed-return yoke and in the loop including the inner pole gap and outer pole gap, the magnetic flux passing through the outer gap begins to appear.

(3) Above 100 A, the outer pole achieves saturation because of its small volume.

The excitation curves obtained from the measurements and calculation are similar (Fig. 7.11). This characteristic was predicted in the original design of RAFFIA, where the magnet is used with fixed maximum fields.
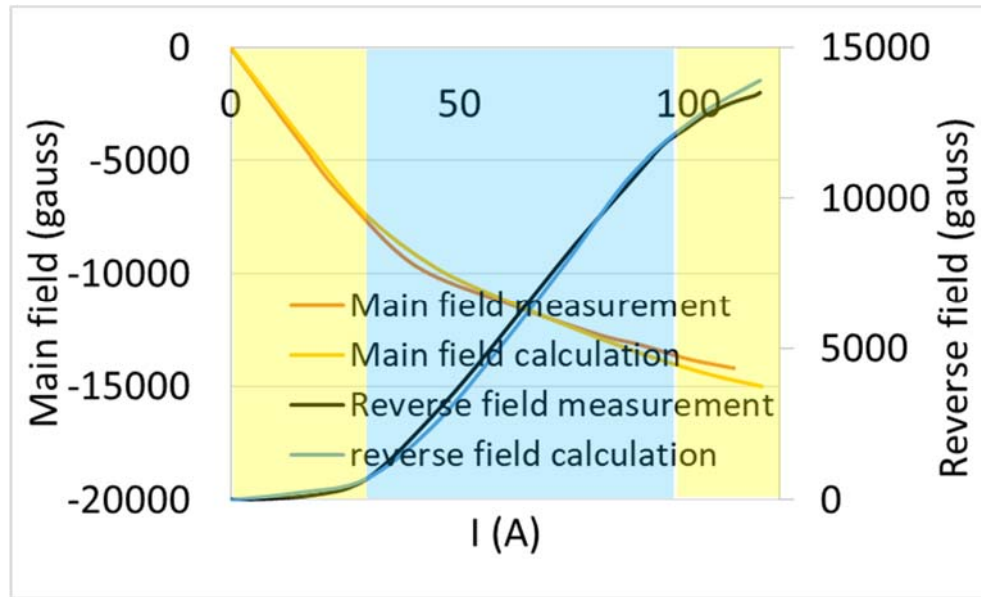
Figure 7.11: Excitation curves of the reverse and main field.
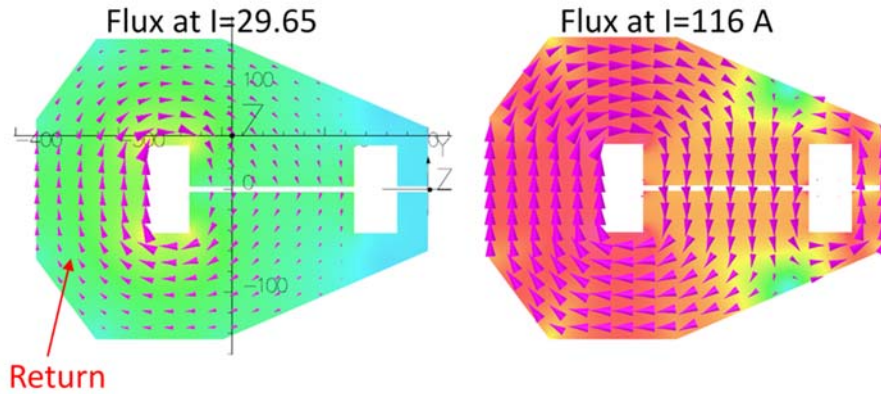
Figure 7.12: Magnetic flux lines at different current in the prototype magnet.

7.7. Magnetic field distribution

7.7.1. Effects of pole gap deformation

To determine the field characteristics of the prototype magnet, line mapping was performed in the X and Z direction near the peak fields. Mapping data in the X direction was taken at the middle of the longitudinal direction of the magnet ($Z = 0$). The mapping position and field data at the excitation current (I) of 123.2 A are shown in Fig. 7.13, where the mapping results with and without gap spacers are shown. The effects of gap modification, such as the gradient in the main fields and higher flux density in the outer pole gap, are clear.
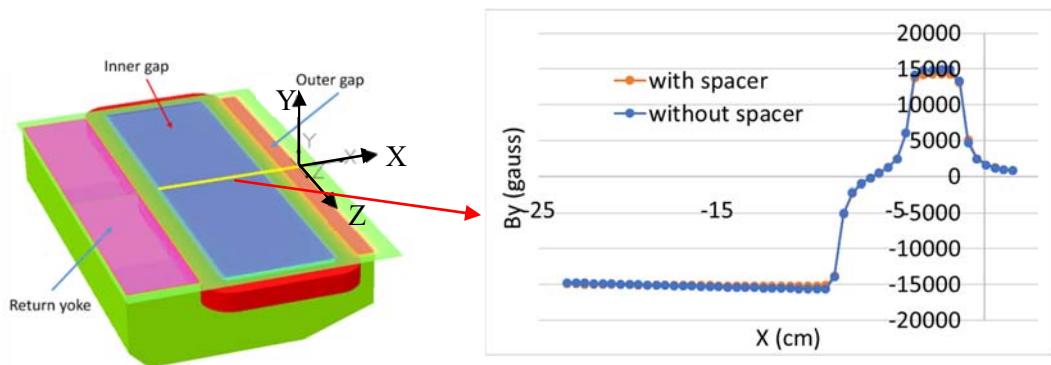
Figure 7.13: Magnetic field profile in the X direction 123.2 A.

Line mapping in the *Z* direction was performed to clarify how the field uniformity along the *Z* is determined by the pole surface profile. The line mapping data measured at the center of the outer and inner poles at the fixed excitation current of 122.4 A are shown in Fig. 7.14. The uniformity along the *Z* direction is much poorer than that of the prototype design. Some of the discrepancies between the actual field and the design can be attributed to the difference in the pole gap size.
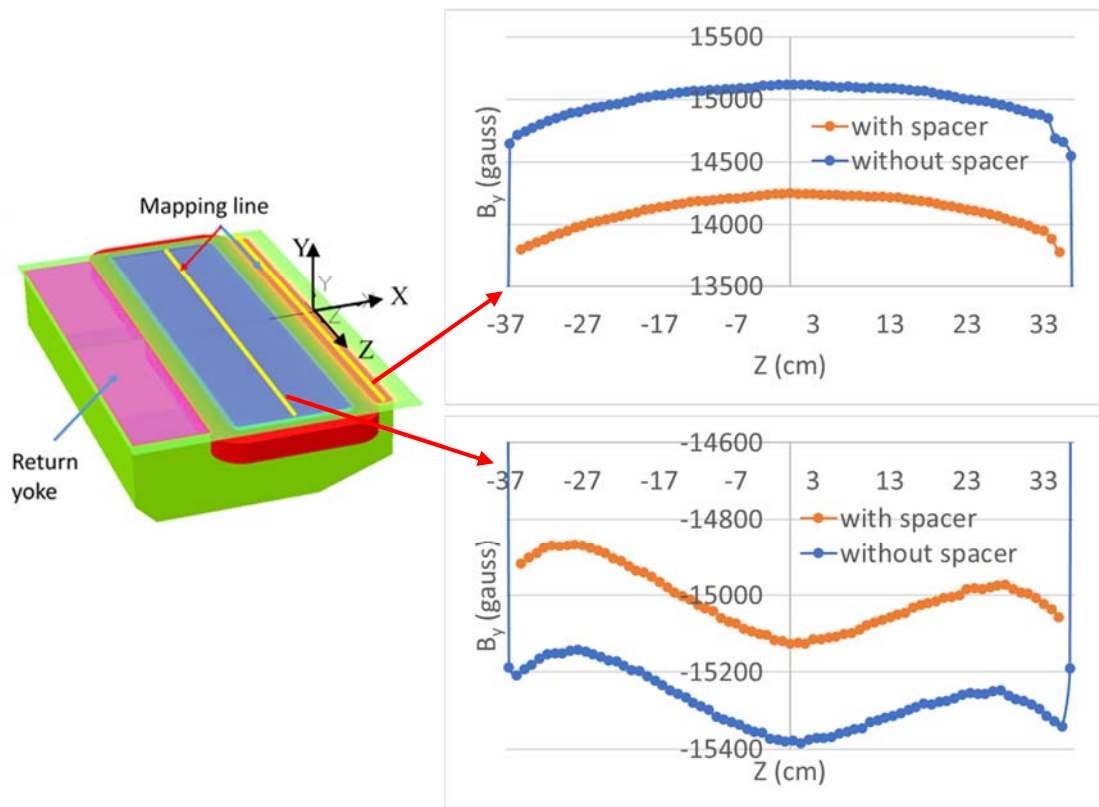
Figure 7.14: Magnetic field profile along the *Z* direction at 122.4 A.

7.7.2. Remaining non-uniformity along the Z direction

To compare the Tosca calculation and the measurement results, the measured gap profile was imported into the Tosca calculation. Gap 1 is the gap size measurement obtained at the KEK machine shop and gap 2 is the micrometer measurement. Normalization field profiles are given for the inner and outer pole gaps in Fig. 7.15 to

show the non-uniformity in the *Z* direction. There were discrepancies between the actual field profile and the calculations. Fig. 7.15 shows that the magnetic field non-uniformity from the Tosca calculation is different from the measurements. The difference may be caused by a discrepancy between the prototype and simulation model gap size profile. This simulation model gap size profile was obtained by interpolating the prototype gap size measurement. The sample points for the gap size measurement from the KEK machine shop were small (Fig. 7.6), and there was a measurement error from several gap size measurements, which may contribute to the discrepancies in the gap size profiles.

(a)   (b)
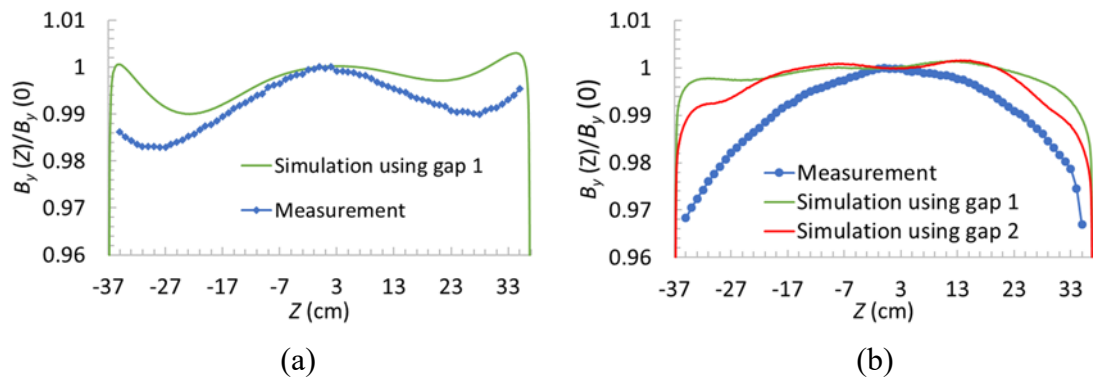
Figure 7.15: Comparison of the non-uniformity of Tosca calculations and the measurements at (a) the inner pole and (b) the outer pole at 122.6 A.

7.7.3. Explanation of the non-uniformity

The inner gap size measurement data was not available after magnet assembly and at excitation and there was some ambiguity in the gap size profiles of the simulation model. Therefore, gap size profile fitting was introduced, where the gap size profiles in the simulation model were adjusted to reproduce the measured non-uniformity at a low current. The field data measured at 25 A was used for this purpose, where the effects induced by any difference in the assumed B-H curve should be negligible. Once the pole gap profile was determined at the low excitation current, it was used for the peak current excitation of 122.6 A. Calculated and measured fields profiles are compared in Fig. 7.16.

The field profile at the peak excitation current was reproduced well for the inner and outer poles. The fitted gap size profiles are compared with the measurements in Fig. 7.17. There was no clear explanation for the discrepancy in the region from –370 to – 190 mm for the outer pole, which seems to be out of the range of measurement errors.
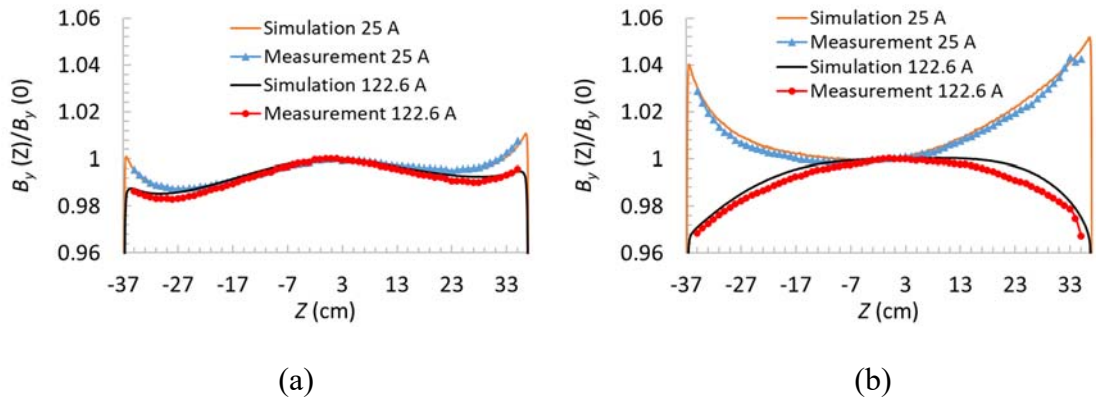
Figure 7.16: Non-uniformity of Tosca calculations and measurements after gap size fitting at (a) the inner pole and (b) the outer pole.
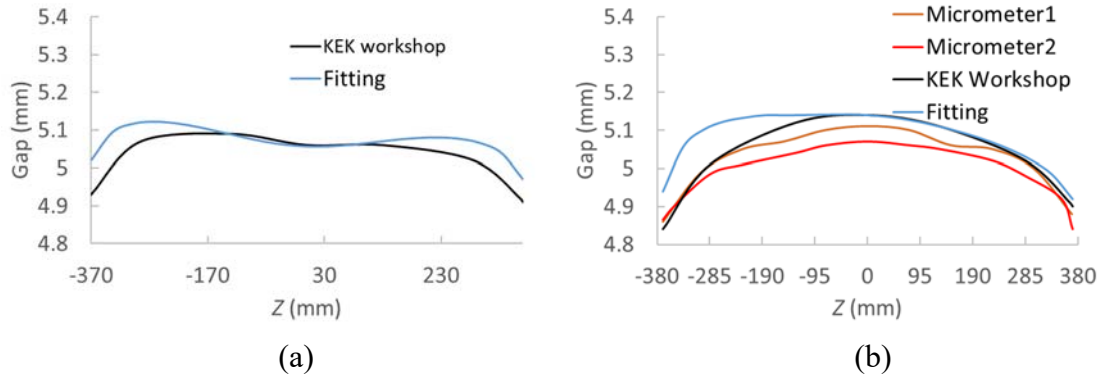
Figure 7.17: Fitted gap size profiles at (a) the inner pole and (b) the outer pole.

Chapter 8 Conclusion

A standard orbit theory and particle tracking code based on the Runge-Kutta approach were established for calculating the generic properties of the RAFFIA. As a typical example, the RAFFIA that can accelerate C_{60}^{10+} ions from 10 to 144 MeV was discussed in detail. The RAFFIA is a unique accelerator designed to produce high-energy giant cluster ions and is a synchrotron-cyclotron hybrid accelerator. The linear orbit theory was justified without loss of generality by the particle tracking code. The orbit stability was guaranteed by the properly optimized ramping of the quadrupole magnets. The intrinsic closed-orbit distortion caused by the physical limitation of the magnet size can be corrected by programmed ramping of a set of the steering magnets. The RAFFIA could be operated at 15 Hz. By using the maximum beam envelope, assuming a beam emittance of 1×10^{-5} m·rad and a maximum deviation from the dispersion function of 5.3 mm, the beam size was calculated as around 6.5 cm and the maximum vacuum vessel size was determined as 10 cm. The macroparticle tracking result shows that the cluster ion beam remained within the vacuum vessel without significant loss and emittance degradation.

The longitudinal motion in the RAFFIA, which is characterized by the inherent feature of variable transition energy, was evaluated by solving the induction acceleration equation. The longitudinal beam parameters of the cluster ion bunch were controlled by varying the phase distance between two barrier voltage pulses, as well as in an induction synchrotron. The acceptable momentum deviation of the injected particles depended on the barrier voltage pulse height, as expected.

The space charge effects on beam-core evolution and the beam current threshold were discussed. The beam-core evolution equation approach, which has the advantage of an extremely quick evaluation time, was justified by the macroparticle tracking simulation. The beam-core evolution equation is a powerful tool for clarifying what happens during high-intensity beam operation and for estimating the space-charge limited current for any accelerator ring. Poincaré mapping in the beam core phase space (σ, $d\sigma/ds$) clearly demonstrated how the beam core evolves, depending on the beam current parameters. Below the beam current threshold, the Poincaré map was stable around the matched beam-core phase point, which is called an elliptic point in nonlinear dynamics terminology. Beyond the threshold, the elliptic point disappeared and period-doubling bifurcation occurred; the beam-core size became large. This beam-core instability was rigorously analyzed by using the linearized beam-core evolution equation and matrix theory (tangent map). A scaling law was evaluated to determine the stability threshold for a cluster ion with various A/Q or injection energy or emittance. A C_{60}^{10+} beam with 10 MeV injection energy and 1×10^{-5} m·rad beam emittance in the RAFFIA had a beam current threshold around 225 μA.

A unique feature of the RAFFIA bending magnet is an inverse field strip in the front side. This feature was justified by using a prototype bending magnet where the main bending field and the reverse field can be excited by a single pair of two coils. The magnetic attraction force caused a significant reduction of the gap size because of a long nose property in the pole face. The gap reduction must be considered in the design stage. Inserting pole gap supports into the gap may be another countermeasure. The non-uniformity of the magnetic field in the longitudinal direction was minimized by designing the pole gap profile using the four-point spline approach. However, in manufacturing, the actual gap profile was slightly different from the design. Thus, the pole gap must be shaped carefully with a high-precision machine because the mechanical profile of the pole gap along the longitudinal direction significantly affects

the magnetic field profile. The remaining field non-uniformity due to the limitations of the precision machine can be corrected by adding correction coils.

From this study, it can be concluded that this new accelerator, RAFFIA, can be constructed, although further design work on the 90° bending magnet is required.

Appendix

A. Runge-Kutta Solution for Equation of Motion

$$r(t + \Delta t) = r(t) + \frac{\Delta t}{6}(k_1 + 2k_2 + 2k_3 + k_4) \Bigg\}$$
$$p(t + \Delta t) = p(t) + \frac{\Delta t}{6}(k_5 + 2k_6 + 2k_7 + k_8) \Bigg\}$$

where p, r, and k are vectors in the global cartesian coordinate.

Here,

$$k_1 = p_1/m\gamma, \qquad k_5 = q\left(E(r_1) + \frac{p_1 \times B(r_1)}{m\gamma}\right),$$

$$k_2 = p_2/m\gamma, \qquad k_6 = q\left(E(r_2) + \frac{p_2 \times B(r_2)}{m\gamma}\right),$$

$$k_3 = p_3/m\gamma, \qquad k_7 = q\left(E(r_3) + \frac{p_2 \times B(r_3)}{m\gamma}\right),$$

$$k_4 = p_4/m\gamma, \qquad k_8 = q\left(E(r_4) + \frac{p_4 \times B(r_4)}{m\gamma}\right),$$

$$p_1 = p(t), \qquad r_1 = r(t),$$

$$p_2 = (p(t) + k_5\,\Delta t/2), \qquad r_2 = (r(t) + k_1\,\Delta t/2),$$

$$p_3 = (p(t) + k_6\,\Delta t/2), \qquad r_3 = (r(t) + k_2\,\Delta t/2),$$

$$p_4 = (p(t) + k_7\Delta t), \quad r_4 = (r(t) + k_3\Delta t).$$

B. KEK digital accelerator ring parameters

The KEK-DA ring is shown in Fig. B1. The ring parameters are given in Table B1 and the beta function in one sector is shown in Fig. B2.

Table B1. KEK-DA ring parameters

Parameter	
Circumference (C)	37.71 m
Curvature of the bending magnet (ρ)	3.3 m
Field gradient (B'/B)	3.664 m^{-1}
Bending angle per magnet (θ)	$\frac{360°}{8}\left(\frac{\pi}{180°}\right) = \frac{\pi}{4}$
Lattice per sector	O-F-D-F-O
Magnet length	2.5918 m
Length of the drift space	2.1206 m/sector
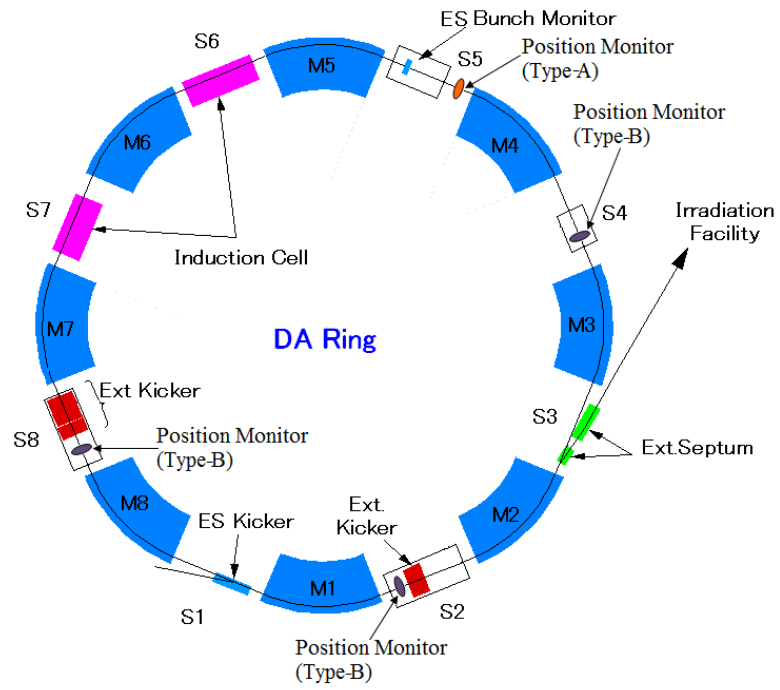
Figure B1: Layout of the KEK-DA ring.
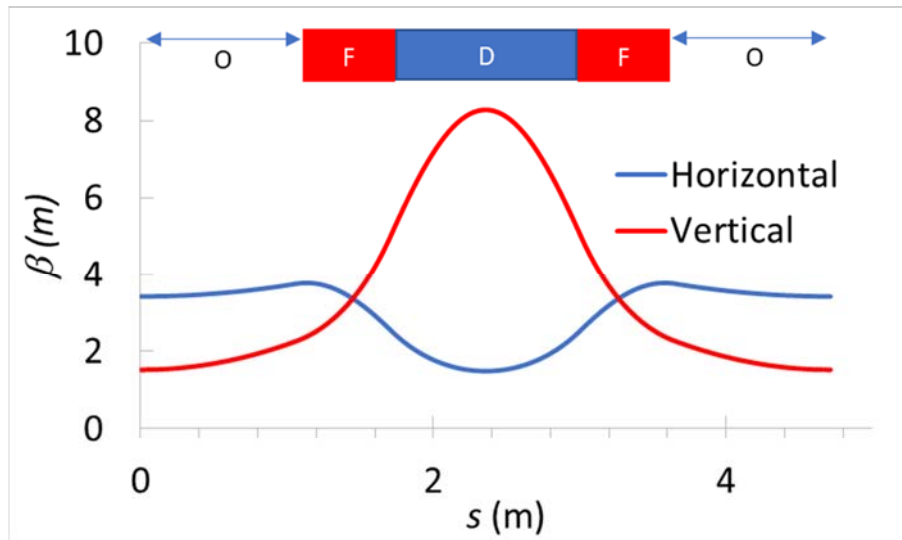
Figure B2: Beta functions in one cell of the KEK-DA lattice.

C. Derivation of the deviation δ from the nonperturbed matched beam-core

The deviation δ satisfies

$$\delta'' + \left[K(s) + \frac{3}{(\beta)^2}\right] \cdot \delta = \frac{k}{\sigma_x^M + \sigma_y^M}. \tag{C.1}$$

Two independent solutions for $\delta'' + \left[K(s) + \frac{3}{\rho_0{}^4}\right] \cdot \delta = 0$ are known to be $\delta_1(s) = \rho_0 \cos 2\psi(s)$ and $\delta_2(s) = \rho_0 \sin 2\psi(s)$ [56], where $\psi(s) = \int_0^s \frac{ds'}{\beta(s')}$ and $\rho_0 = \sqrt{\beta}$. The general solution of Eq. (C.1) is written by

$$\delta(s) = c_1 \delta_1(s) + c_2 \delta_2(s) + \int_0^s f(s') G(s, s') ds' \tag{C.2}$$

where $G(s, s') = \frac{1}{W}[-\delta_1(s)\delta_2(s') + \delta_1(s')\delta_2(s)]$, Wronskian $W = \begin{vmatrix} \delta_1 & \delta_2 \\ \delta'_1 & \delta'_2 \end{vmatrix} = \delta_1 \delta'_2 - \delta_2 \delta'_1$, and $f(s') = \frac{k}{\sigma_x^M + \sigma_y^M}$. We obtain $W = 2$ and $G(s, s') = \frac{1}{2}\rho_0(s)\rho_0(s') \sin 2[\psi(s) - \psi(s')]$.

Eq. (C.2) can be written in

$$\begin{aligned}
\delta(s) = c_1 &\left(\rho_0'^{(s)} \cos 2\psi(s) - 2\psi'^{(s)}\rho_0(s) \sin 2\psi(s)\right) \\
&+ c_2 \left(\rho_0'^{(s)} \sin 2\psi(s) + 2\psi'(s)\rho_0(s) \cos 2\psi(s)\right) \\
&+ \frac{1}{2}\rho_0'(s) \int_0^s f(s')\rho_0(s') \sin 2[\psi(s) - \psi(s')]\, ds' \\
&+ \psi'(s)\rho_0(s) \int_0^s f(s')\rho_0(s') \cos 2[\psi(s) - \psi(s')]\, ds'
\end{aligned} \tag{C.3}$$

For periodic solution, then $\delta(0) = \delta(C)$, $\delta'(0) = \delta'(C)$ and $\rho_0(0) = \rho_0(C)$. From that condition and assuming $\rho_0'(0) = 0$, we found

$$c_1(\rho_0(0) - \rho_0(C) \cos 2\psi(C))$$
$$= c_2\rho_0(C) \sin 2\psi(C)$$
$$+ \frac{1}{2}\rho_0(C) \int_0^C f(s')\rho_0(s') \sin 2[\psi(C) - \psi(s')]\, ds'$$

(C.4)

$$\frac{c_1}{\rho_0(C)} \sin 2\psi(C)$$
$$= c_2 \left(\frac{1}{\rho_0(C)} \cos 2\psi(C) - \frac{1}{\rho_0(0)}\right)$$
$$+ \frac{1}{2}\frac{1}{\rho_0(C)} \int_0^C f(s')\rho_0(s') \cos 2[\psi(s) - \psi(s')]\, ds'$$

(C.5)

By elimination Eq. (C.4) with respect to Eq. (C.5), we obtain

$$c_1 = \frac{1}{4 \sin \mu} \left(\int_0^C f(s')\rho_0(s') \cos[-\mu + 2\psi(s')]\, ds'\right)$$

(C.6)

$$c_2 = \frac{1}{4 \sin \mu} \left(\int_0^C f(s')\rho_0(s') \sin[-\mu + 2\psi(s')]\, ds'\right)$$

(C.7)

where $\psi(C) = \mu$. By substituting Eq. (C.6) and (C.7) into Eq. (C.3), we obtain the solution

$$\delta(s) = \frac{\rho_0(s)}{4 \sin \mu} \left(\int_0^{s+C} \frac{k}{\sigma_x^M + \sigma_y^M} \sqrt{\beta(s')}\rho_0(s') \cos[\mu - 2|\psi(s) - \psi(s')|]\, ds'\right)$$

.

D. The eigenvalue stability of the linearized core evolution equation solution

The beam current threshold can be obtained from the eigenvalues of the transfer matrix of the linearized core evolution equation. The eigenvalues of the transfer matrix correspond to the beam current is shown in the following table,

Table D1: Eigenvalues of the matrix corresponding to the beam current

I_b (μA)	Eigenvalue			
	λ_1	λ_2	λ_3	λ_4
0	- 0.9545 + 0.2980i	- 0.9545 - 0.2980i	- 0.8732 + 0.4874i	- 0.8732 - 0.4874i
50	- 0.9687 + 0.2480i	- 0.9687 - 0.2480i	- 0.8973 + 0.4415i	- 0.8973 - 0.4415i
100	- 0.9802 + 0.1980i	- 0.9802 - 0.1980i	- 0.9179 + 0.3967i	- 0.9179 - 0.3967i
200	- 0.9956 + 0.0937i	- 0.9956 - 0.0937i	- 0.9508 + 0.3098i	- 0.9508 - 0.3098i
210	- 0.9966 + 0.0821i	- 0.9966 - 0.0821i	- 0.9536 + 0.3011i	- 0.9536 - 0.3011i
220	- 0.9976 + 0.0697i	- 0.9976 - 0.0697i	- 0.9562 + 0.2925i	- 0.9562 - 0.2925i
230	- 0.9984 + 0.0562i	- 0.9984 - 0.0562i	- 0.9588 + 0.2839i	- 0.9588 - 0.2839i
240	- 0.9992 + 0.0403i	- 0.9992 - 0.0403i	- 0.9614 + 0.2752i	- 0.9613 - 0.2752i
250	- 0.9998 + 0.0165i	- 0.9999 - 0.0165i	- 0.9638 + 0.2665i	- 0.9638 - 0.2665i
251	- 0.9999 + 0.0122i	- 0.9999 - 0.012i	- 0.9641 + 0.2656i	- 0.9641 - 0.2656i
252	- 0.9999 + 0.0049i	- 0.9999 - 0.0049i	- 0.9643 + 0.2648i	- 0.9643 - 0.2648i
253	-1.0099547	-0.9901435	- 0.9645 + 0.2639i	- 0.9645 - 0.2639i
254	-1.0148944	-0.9853241	- 0.9648 + 0.2630i	- 0.9648 - 0.2630i
255	-1.0185351	-0.9818023	- 0.9650 + 0.2621i	- 0.9650 - 0.2621i
260	-1.0305284	-0.9703759	- 0.9662 + 0.2577i	- 0.9662 - 0.2577i
270	-1.0446169	-0.9572888	- 0.9685 + 0.2489i	- 0.9685 - 0.2489i
280	- 0.9708 + 0.2399i	- 0.9708 - 0.2399i	-1.0536112	-0.9491168
290	- 0.9730 + 0.2307i	- 0.9730 - 0.2307i	-1.0597411	-0.9436267
300	- 0.9751 + 0.2214i	- 0.9752 - 0.2214i	-1.0637455	-0.9400739

From Table D1, all the eigenvalues of the transfer matrix up to the beam current of 252 μA are complex conjugate and satisfy the stability condition. Meanwhile, beyond that current, one of the eigenvalue is a real and larger than one. Thus, we can conclude that the stability threshold is 252 μA.

Bibliography

[1] H. Pauly, *Atom, Molecule, and Cluster Beams II: Cluster Beams, Fast and Slow Beams, Accessory Equipment and Applications* (2000).

[2] V. R. Bhardwaj, P. B. Corkum, and D. M. Rayner, Phys. Rev. Lett. **91**, 203004 (2003).

[3] H. Bräuning, R. Trassl, A. Diehl, A. Theiß, E. Salzborn, A. A. Narits, and L. P. Presnyakov, Phys. Rev. Lett. **91**, 168301 (2003).

[4] S. Díaz-Tendero, M. Alcamí, and F. Martín, Phys. Rev. Lett. **95**, 013401 (2005).

[5] 293 (1993). Attal, P.[1] P. Attal, S. Della-Negra, D. Gardès, J. D. Larson, Y. Le Beyec, R. Vienet-Legué, and B. Waast, Nucl. Instruments Methods Phys. Res. Sect. A Accel. Spectrometers, Detect. Assoc. Equip. 328, S. Della-Negra, D. Gardès, J. D. Larson, Y. Le Beyec, R. Vienet-Legué, and B. Waast, Nucl. Instruments Methods Phys. Res. Sect. A Accel. Spectrometers, Detect. Assoc. Equip. **328**, 293 (1993).

[6] S. Matt, P. Schbier, A. Stamatovic, H. Deutsch, K. Becker, and T. D. Märk, Philos. Trans. R. Soc. A Math. Phys. Eng. Sci. **357**, 1201 (1999).

[7] P. Scheier and T. D. Märk, Phys. Rev. Lett. **73**, 54 (1994).

[8] A. Brenac, F. Chandezon, H. Lebius, A. Pesnelle, S. Tomita, and B. A. Huber, Phys. Scr. **T80**, 195 (1999).

[9] T. Seki and J. Matsuo, Nucl. Instruments Methods Phys. Res. Sect. B Beam Interact. with Mater. Atoms **237**, 455 (2005).

[10] B. Waast, S. Della-Negra, and A. Lafoux, Nucl. Instruments Methods Phys. Res. Sect. A Accel. Spectrometers, Detect. Assoc. Equip. **382**, 348 (1996).

[11] Y. Saitoh, K. Mizuhashi, and S. Tajima, Nucl. Instruments Methods Phys. Res. Sect. A Accel. Spectrometers, Detect. Assoc. Equip. **452**, 61 (2000).

[12] K. Takayama, Y. Arakida, T. Dixit, T. Iwashita, T. Kono, E. Nakamura, K. Otsuka, Y. Shimosaki, K. Torikai, and M. Wake, Phys. Rev. Lett. **98**, 54801 (2007).

[13] K. Takayama, T. Yoshimoto, M. Barata, L. K. Wah, L. Xingguang, T. Iwashita, S. Harada, T. Adachi, T. Arai, D. Arakawa, H. Asao, E. Kadokura, T. Kawakubo, H. Nakanishi, Y. Okada, K. Okamura, K. Okazaki, A. Takagi, S. Takano, and M. Wake, Phys. Rev. ST Accel. Beams **17**, 10101 (2014).

[14] K. Takayama, T. Adachi, M. Wake, and K. Okamura, Phys. Rev. ST Accel. Beams **18**, 50101 (2015).

[15] D. W. Kerst, Phys. Rev. **58**, 841 (1940).

[16] N. C. Christofilos, R. E. Hester, W. A. S. Lamb, D. D. Reagan, W. A. Sherwood, and R. E. Wright, Rev. Sci. Instrum. **35**, 886 (1964).

[17] K. Takayama and R. J. Briggs, *Induction Accelerators* (Springer, New York, 2011).

[18] I. D. Smith, Phys. Rev. Spec. Top. - Accel. Beams **7**, 1 (2004).

[19] M. A. D. Wilson, IEEE Trans. Nucl. Sci. **28**, 3375 (1981).

[20] S. D. Putnam, in *Proc. 1987 Part. Accel. Conf.* (Washington, DC, 1987), pp. 887–891.

[21] K. Takayama and J. Kishiro, Nucl. Instruments Methods Phys. Res. Sect. A Accel. Spectrometers, Detect. Assoc. Equip. **451**, 304 (2000).

[22] I. Yamada and J. Khoury, Mater. Res. Soc. Symp. Proc. **1354**, 21 (2012).

[23] H. Dammak, A. Dunlop, D. Lesueur, A. Brunelle, S. Della-Negra, and Y. Le Beyec, Phys. Rev. Lett. **74**, 1135 (1995).

[24] A. S. El-Said, Nucl. Instruments Methods Phys. Res. Sect. B Beam Interact. with Mater. Atoms **267**, 953 (2009).

[25] T. Kitayama, Y. Morita, K. Nakajima, K. Narumi, Y. Saitoh, M. Matsuda, M. Sataka, M. Tsujimoto, S. Isoda, M. Toulemonde, and K. Kimura, Nucl. Instruments Methods Phys. Res. Sect. B Beam Interact. with Mater. Atoms **356**–**357**, 22 (2015).

[26] R. Soma, Y. Saitoh, M. Sakamaki, K. Amemiya, A. Iwase, and T. Matsui, AIP Adv. **8**, 056433 (2018).

[27] K. Nakajima, K. Nagano, M. Suzuki, K. Narumi, Y. Saitoh, K. Hirata, and K. Kimura, Appl. Phys. Lett. **104**, 3 (2014).

[28] K. Takayama, in *Asian Forum Accel. Detect. 2019* (2019).

[29] K. Takayama and K. Horioka, in *21st Int. Symp. Heavy Ion Fusion* (Astana, Kazakhstan, 2016).

[30] Taufik, T. Adachi, M. Wake, and K. Takayama, in *Proc. 14th Annu. Meet. Part. Accel. Soc. Japan August 1-3* (Sapporo, Japan, 2017), pp. 359–363.

[31] T. Adachi, *Private Discussion* (2018).

[32] J. Hasegawa, Y. Ishikawa, and W. Feng, in (2019).

[33] R. D. Scarpetti, S. Nath, J. Barraza, C. A. Ekdahl, E. Jacquez, B. T. Mccuistian, K. Nielsen, M. Schulze, J. Seitz, G. J. Caporaso, Y. Chen, G. Logan, and F. Bieniosek, in *Proc. PAC07, Albuquerque* (New Mexico, USA, 2007), pp. 831–835.

[34] T. Adachi and T. Kawakubo, Phys. Rev. Spec. Top. - Accel. Beams **16**, 053501 (2013).

[35] K. Okamura and K. Takayama, in *Proc. IPAC2017* (Copenhagen, Denmark, 2017), pp. 3388–3390.

[36] R. H. Landau, M. J. Páez, and C. C. Bordeianu, *A Survey of Computational Physics* (PRINCETON UNIVERSITY PRESS, Princeton, New Jersey, 2008).

[37] J. C. Butcher, *Numerical Methods for Ordinary Differential Equations*, 3rd Editio (John Wiley & Sons Ltd, Chichester, England, 2008).

[38] Taufik, T. Adachi, M. Wake, and K. Takayama, Phys. Rev. Accel. Beams **22**, 044001 (2019).

[39] N. Munemoto, S. Takano, E. Kadokura, Taufik, T. Yoshimoto, X. Liu, T. Adachi, M. Ikeda, T. Kawakubo, K. Okamura, K. Takayama, and M. Wake, Phys. Rev.

Accel. Beams **20**, (2017).

[40] T. Monma, K. Takayama, T. Yoshimoto, and L. Xigguang, in *Proc. HIAT2015, Yokohama, Japan* (2015), p. MOPA16.

[41] Taufik and K. Takayama, Phys. Lett. A 125855 (2019).

[42] J. Knaster, P. Garin, H. Matsumoto, Y. Okumura, M. Sugimoto, F. Arbeiter, P. Cara, S. Chel, A. Facco, P. Favuzza, T. Furukawa, R. Heidinger, A. Ibarra, T. Kanemura, A. Kasugai, H. Kondo, V. Massaut, J. Molla, G. Micciche, S. O'hira, K. Sakamoto, T. Yokomine, and E. Wakai, Nucl. Fusion **57**, 102016 (2017).

[43] S. Kawata, T. Karino, and A. I. Ogoyski, Matter Radiat. Extrem. **1**, 89 (2016).

[44] H. A t Abderrahim, J. Galambos, Y. Gohar, S. Henderson, G. Lawrence, T. McManamy, A. C. Mueller, S. Nagaitsev, H. Nolen, E. Pitcher, R. Rimmer, R. Sheffield, and M. Zodosow, *Accelerator and Target Technology for Accelerator Driven Transmutation and Energy Production* (2010).

[45] T. S. Dixit, T. Iwashita, and K. Takayama, Nucl. Instruments Methods Phys. Res. Sect. A Accel. Spectrometers, Detect. Assoc. Equip. **602**, 326 (2009).

[46] I. Bozsik and I. Hofmann, Nucl. Instruments Methods Phys. Res. **187**, 305 (1981).

[47] J. O'Connell, T. P. Wangler, R. S. Mills, and K. R. Crandall, in *Proc. PAC* (1993), pp. 3657–3659.

[48] J.-M. Lagniel, Nucl. Instruments Methods Phys. Res. Sect. A Accel. Spectrometers, Detect. Assoc. Equip. **345**, 46 (1994).

[49] T. P. Wangler, K. R. Crandall, R. Ryne, and T. S. Wang, Phys. Rev. Spec. Top. - Accel. Beams **1**, 084201 (1998).

[50] C. Chen and R. C. Davidson, Phys. Rev. E **49**, 5679 (1994).

[51] J. Qiang and R. D. Ryne, Phys. Rev. Spec. Top. - Accel. Beams **3**, 064201 (2000).

[52] J. Qiang, Phys. Rev. Accel. Beams **21**, 034201 (2018).

[53] K. Takayama, Lett. Al Nuovo Cim. **34**, 190 (1982).

[54] L. E. Reichl, in *Transit. to Chaos Conserv. Class. Syst. Quantum Manifestations* (Springer New York, New York, NY, 2004), pp. 58–133.

[55] C. Bovet, R. Gouiran, I. Gumowski, and K. H. Reich, *A Selection of Formulae and Data Useful for the Design of A.G. Synchrotrons; Rev. Version* (CERN, Geneva, 1970).

[56] K. Takayama, Part. Accel. **21**, 259 (1987).